Passive Chemiresistor Sensor Based on Iron (II) Phthalocyanine Thin Films for Monitoring of Nitrogen Dioxide

by

John Hungjen Shu

A dissertation submitted to the Graduate Faculty of
Auburn University
in partial fulfillment of the
requirements for the Degree of
Doctor of Philosophy

Auburn, Alabama
Dec 13, 2010

Keywords: Iron phthalocyanine, Nitrogen dioxide, Gas sensor, Chemiresistor sensor, Thin film sensor

Approved by:

Bryan A. Chin, Chair, Professor of Materials Engineering
Arnold Vainrub, Associate Professor of Department of Anatomy, Physiology and Pharmacology
Dong-Joo (Daniel) Kim, Associate Professor of Materials Engineering
Jong Wook Hong, Associate Professor of Materials Engineering
ZhongYang Cheng, Associate Professor of Materials Engineering

Abstract

Nitrogen dioxide gas is a common atmospheric pollutant that is hazardous to human health at concentrations as low as one part per million (ppm). Iron (II) phthalocyanine (FePc) thin films have been identified to be sensitive materials for the detection of nitrogen dioxide and other oxidizing gases. The charge carrier complex formed from the interaction between FePc and nitrogen dioxide molecules acts to liberate hole charge carriers, thereby increasing film conductivity. Traditional metal-Pc based sensors rely on substrate heating and active temperature control to achieve nitrogen dioxide detection in a reversible manner. However, the heating process causes film deterioration and limits the life of metal-Pc sensors.

In this dissertation, an alternate, new approach was investigated to produce a non-reversible, passive, FePc thin film sensor that does not require continuous power for operation. The sensor was manufactured using standard microelectronics fabrication procedures, with emphasis on low cost and sensor consistency. The sensor substrate consists of a gold interdigitated electrode pattern deposited on an oxidized silicon or quartz wafer. The FePc thin film is then vacuum sublimed over the interdigitated electrodes to form the finalized sensor. Different thicknesses and morphologies of FePc thin films were fabricated.

Once sensor fabrication was accomplished, the general response, temperature dependence, concentration dependence, specificity, and longevity of FePc thin film sensors were investigated. To evaluate general sensor reponse, sensors were exposed to 100 ppm nitrogen dioxide in nitrogen, with a flow rate of 0.25 liters per minute (L/min), at the temperatures of -46, 20, and 71 °C. For each case, the resistance of the sensor decreased exponentially as a function of exposure duration and reached saturation within 25 minutes. The resistance decrease was measured to be four, three, and two orders of magnitude for the exposure temperatures of -46, 20, and 71 °C respectively. In these experiments, sub-zero temperature

detection of nitrogen dioxide with FePc thin films was reported for the first time. It was found that the response at -46 °C was greater than at 20 or 71 °C. To evaluate temperature dependence, sensors were thermal cycled in the range of -50 to 80 °C, first under ultra-high purity nitrogen gas at 0.25 L/min, and then under 100 ppm nitrogen dioxide gas at 0.25 L/min. Intrinsic FePc film conductivity was measured by thermal cycling sensors under nitrogen gas. Extrinsic FePc film conductivity was measured by thermal cycling sensors under nitrogen dioxide gas. Results from these tests indicated that the temperature dependence of FePc thin film conductivity is described by the Arrhenius equation. Activation energies of 0.70 and 0.36 eV were measured for intrinsic and extrinsic conductivity respectively. These activation energies compared favorably with energies reported by other investigators. To investigate concentration dependence, experiments were performed at room temperature over the range of 0.5 to 2 ppm nitrogen dioxide. Sensor response showed that the change in relative resistance over time can be used to reliably differentiate different concentrations in this range. The normalized resistance change over time was found to be a linear function of concentration. Specificity studies were conducted by exposing sensors to humidity, oxygen, and ammonia, common interferant gases encounted in the atmosphere. Humidity and oxygen did not alter the response, indicating good specificity of the FePc sensor. Ammonia gas de-doped the FePc thin film, causing resistance levels to increase. Exposure to ammonia gas can cleanse FePc thin film sensors and restore high initial resistance levels. Sensor longevity was investigated by monitoring sensor response under several storage conditions. Operational longevity tests under flowing nitrogen gas at 0.1 L/min in a continuous -50 to 80 °C temperature cycle indicated excellent sensor stability. De-doping of atmospheric interefferants occurred steadily for several cycles until the resistance levels became strictly a function of temperature. At room temperature, a dark or UV shielded enclosed air environment can be used to preserve resistance levels indefinitely.

To investigate the effects of sensor fabrication parameters, the film thickness, substrate type, and heat treatment effects were analyzed. FePc film thickness effects were investigated by fabricating sensors ranging from 50 to 450 nm in thickness. Observation of surface morphology under a scanning electron microscope (SEM) showed an evolution of increasing grain size and film roughness as film thickness increased. The 450 nm films have the largest grain size and surface roughness. They also form the best film-electrode contact. For substrate type analysis, FePc thin films simultaneously deposited on sensor substrates consisting of n-type oxidized silicon, p-type oxidized silicon, and quartz wafers were observed under SEM. Visual results show similar film morphologies. Electrical resistance levels under a continuous -50 to 80 °C thermal cycle under 0.1 L/min flowing nitrogen gas also indicated similar film conductivity values. To investigate the effects of post-deposition heat treatment, sensors were subjected to temperatures ranging from 20 to 340 °C under air for a constant duration of two hours. Sensor response to 100 ppm nitrogen dioxide gas showed that sensors saturated faster as treatment temperature was increased up to 190 °C. In summary, results from sensor fabrication parameter analysis suggested that a polycrystalline α-FePc thin film active layer, 450 nm in thickness, on either an oxidized silicon or quartz substrate, with no post-deposition heat treatment produced the best results for a passive sensor.

In attempt to understand the sensor conductivity mechanism and to model sensor response, two theoretical models were developed. To determine the sensor conductivity mechanism, theoretical surface and bulk conductivity equations were derived for the sensor geometry. Comparison of measured resistance values with published metal-Pc conductivity values suggests that the bulk conductivity assumption yields comparable intrinsic values of 2.2 x 10^{-5} and 2.49 x 10^{-8} $\Omega^{-1}m^{-1}$ at 80 and -50 °C respectively. Since a passive, integrating sensor inevitably approaches saturation, a sensor response model was developed for determining analyte concentrations based on the level of saturation. This passive response model was derived with reference to established equations on gas adsorption-desorption kinetics. Experimental sensor saturation data revealed that film conductivity is a power law of surface

coverage. The passive sensing model also predicts a linear, proportional relationship between normalized resistance change and analyte gas concentration. Experimental sensor response to a concentration gradient showed that the model was able to provide excellent predictions for sensor response to various concentrations of nitrogen dioxide. The lower limit of detection was determined to be roughly 0.3 ppm. In summary, results show that as-deposited FePc thin films on silicon dioxide and quartz substrates with no post-deposition heat treatment produced sensors that can reliably differentiate nitrogen dioxide concentrations as low as 0.3 ppm, via passive monitoring of resistance levels.

Acknowledgments

I would like to thank Dr. Howard C. Wikle for his assistance in testing methodology, test cell design, data acquisition setup, and countless other processes and procedures regarding not only this nitrogen dioxide sensor research, but also other projects. With his guidance, I was able to learn and acquire sound engineering practices.

Dr. Hong Yang has shared with me a great deal of knowledge regarding solid state gas sensor design, active layer materials, sensor fabrication, and gas exposure testing. Her help has allowed this research to start on solid fundamentals and pointed in the right direction.

Dr. Xie Fie has cooperated in a significant portion of preliminary work, and I thank him for being there as we struggled to fabricate good working sensors.

Vicki Shu, Ph.D. student in electrical engineering, was tremendous in providing knowledge and expertise regarding microelectronics fabrication techniques and procedures at AMSTC.

Kanchanna Weerakoon, Ph.D. student, has assisted in the batch fabrication of sensors and the setup of laboratory experiments. The discussions with her regarding the sensor platform and research project in general have led to much insight into my research as a whole.

Shin Horikawa, Ph.D. student, has shared with me many discussions regarding sensing principles and testing methodology. We have worked together in our experiments and we constantly try to achieve that greater understanding of our work.

I especially want to thank Dr. Bryan A. Chin, my advisor and head of the Materials Engineering Program at Auburn University, for guidance in research direction, use of equipment, and funding for my education. The opportunity that he has given me is one that shall always be remembered, for it has changed everything.

Table of Contents

List of Illustrations

List of Tables

List of Abbreviations

ACGIH American Conference of Industrial Hygienists

AFM Atomic force microscopy

AMSTC Alabama Microelectronics Science and Technology Center

CAD Computer aided design

E-beam Electron beam

FePc Iron phthalocyanine

HDMS Hexamethyl disilazene

HNO_3 Nitric acid

MON Mixed oxides of nitrogen

MPc Metal substituted phthalocyanine

N_2O_4 Nitrogen tetroxide

NIOSH National Institute for Occupational Safety and Health

NO_2 Nitrogen dioxide

O_3 Ozone

OSHA Occupational Safety and Health Administration

PFA perfluoroalkoxy copolymer resin

ppm part per million

PTFE polytetrafluoroethylene

QCM Quartz Crystal Microbalance

RCA Radio Corporation of America

SEM Scanning electron microscope

UV Ultraviolet

Chapter 1

Introduction

1.1 Background

The danger to human health associated with exposure to nitrogen dioxide (NO_2) gas is well documented, and is known to cause symptoms ranging from permanent deterioration of pulmonary function to fatal pulmonary failure [1]. The risks of nitrogen dioxide exposure are high for older adults and young children, particularly for those with asthma [2, 3]. Due to increased findings and results correlating nitrogen dioxide levels to lung disease, many governments and health agencies around the world have began to adopt stricter guidelines regarding safe levels of nitrogen dioxide exposure. Table 1.1 contains a list of nitrogen dioxide levels observed under various conditions and Table 1.2 contains a list of standard guidelines for nitrogen dioxide exposure.

Table 1.1: Nitrogen dioxide levels

(ppmv)	(mg/m3)	Description	Source
0.015	0.028	Home average levels	UK HPA[1] (2007)
0.016	0.030	Summer avg. for inner city homes	[2]
0.017	0.033	Increased respiratory symptoms among children	[3]
0.030	0.056	Avg for inner city homes	[2]
0.037	0.070	Beijing, China 2008 city levels	IOC[2] (2008)
0.040	0.075	Winter avg. for inner city homes	[2]
0.266	0.500	Acute health effects observed after 1h exposure	[1]
0.600	1.128	Home peak levels, 1 hr avg.	UK HPA[1] (2007)

[1] United Kingdom Health Protection Agency

[2] International Olympic Committee

From the guidelines listed in Table 1.2, it is worth noting that the National Institute for Occupational Safety and Health (NIOSH), the American Conference of Industrial Hygienists

Table 1.2: Nitrogen dioxide exposure guidelines

(ppmv)	(mg/m3)	Description	Organization
0.021	0.040	Air quality guideline (1y)	WHO[1] (2005)
0.053	0.100	Air quality standard	EPA[2]
0.106	0.200	Short term air quality guideline (1h)	WHO[1] (2005)
0.150	0.282	Air quality standard	UK HPA[3] (2007)
1.000	1.880	Recommended exposure limit (REL)	NIOSH[4]
1.000	1.880	Short term exposure limit (STEL)	OSHA[5]/ACGIH[6]
3.000	5.640	Threshold limit value	ACGIH[6]
5.000	9.400	Permissible exposure limit	OSHA[5]
20.000	37.600	Immediately dangerous to life/health (IDLH)	NIOSH[4]

[1] World Health Organization

[2] Environmental Protection Agency

[3] United Kingdom Health Protection Agency

[4] National Institute for Occupational Safety and Health

[5] Occupational Safety and Health Administration

[6] American Conference of Industrial Hygienists

(ACGIH), and the Occupational Safety and Health Administration (OSHA) have each posted recommended exposure levels to exceed no greater than 1 part per million (ppm) in volume.

1.1.1 Sources of nitrogen dioxide

Nitrogen dioxide is present everywhere in the earth's atmosphere in trace quantities. It is estimated that 30% of the nitrogen dioxide present in the atmosphere is produced from naturally occurring phenomena, while 70% is produced from anthropogenic sources [4]. The natural sources of nitrogen dioxide include biomass combustion due to forest fires and volcanic activity, biochemical reactions from microorganisms present in soil, and high temperature and high pressure chemical reactions supported by lightning. The anthropogenic sources of nitrogen dioxide are primarily fossil fuel combustion, agricultural sources, and aircraft exhaust. Of all sources, fossil fuel combustion of coal, oil, and gas is the dominant contributor, accounting for roughly 64% of the total nitrogen dioxide in the atmosphere. Figure 1.1 contains a breakdown of the various sources of nitrogen dioxide by percentage. In cities or urban regions, nitrogen dioxide in the atmosphere is dominated by manmade sources. Studies have shown that up to 99% of nitrogen dioxide in urban air may be traced to anthropogenic origins [5].

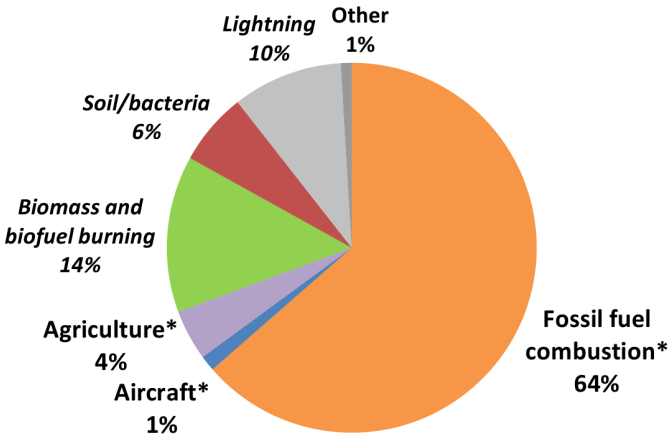

Figure 1.1: Sources of nitrogen dioxide in the atmosphere consist primarily of anthropogenic origin, which account for roughly 70% of all nitrogen dioxide present in the atmosphere. The anthropogenic sources of nitrogen dioxide consist of fossil fuel combustion, agricultural sources, and aircraft exhaust. Fossil fuel combustion of coal, oil, and gas is the single greatest contributor of total nitrogen dioxide in the atmosphere with 64% of the total [4]. (* Denotes anthropogenic source of nitrogen dioxide.)

1.1.2 Nitrogen dioxide in the atmosphere

The presence of nitrogen dioxide in the atmosphere contributes to a dynamic balance between the mixed oxides of nitrogen (MON), commonly referred to as NO_x. The primary species of the MON family are nitric oxide (NO), nitrogen dioxide (NO_2), and nitrogen tetroxide (N_2O_4). The molecular structure of these three species are drawn in Figure 1.2. Nitric oxide is a colorless gas with a sharp, sweet odor. In industry, nitrogen dioxide is produced in mass quantities as an intermediate for nitric acid synthesis from ammonia. In nature, it is an important signaling molecule for various biological systems of mammals and plants [6, 7, 8]. Nitrogen dioxide is the most toxic species of the MON family, and is a brown colored gas with a sharp acrid odor. Nitrogen tetroxide is a red-brown colored liquid that exists in equilibrium with nitrogen dioxide. At temperatures below -11.2°C under atmospheric pressure or when under compression, nitrogen dioxide liquefies into nitrogen tetroxide. Nitrogen dioxide is responsible for the characteristic brownish tint of smog or air pollution.

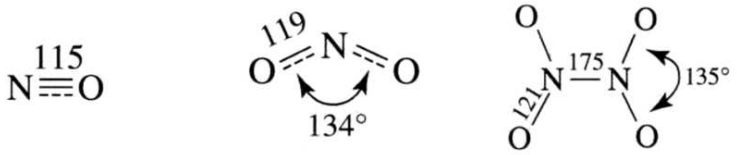

(a) Nitric oxide (b) Nitrogen dioxide (c) Nitrogen tetroxide

Figure 1.2: The molecular diagrams for the family of mixed oxides of nitrogen show angles and bond lengths in picometers. NO is a colorless gas with a sharp sweet odor, nitrogen dioxide is a brown colored gas with an acrid smell, while nitrogen tetroxide is a red-brown colored liquid.

In order for the MON family of gases to form a dynamic balance in earth's atmosphere, a nitrogen cycle exists to maintain an equilibrium as it acts to convert nitrogen between nitric oxide and nitrogen dioxide. As a byproduct of the cycle, ozone (O_3) is formed or consumed. The nitrogen cycle with its relevant chemical reactions is presented in Figure 1.3. With nitric oxide, ozone, and the presence of sunlight, photochemical oxidation can occur to produce nitrogen dioxide. Conversely, with the presence of sunlight, oxygen, and

nitrogen dioxide, photodissociation of nitrogen dioxide can occur to produce nitric oxide and troposcopic ozone. While ozone acts as a UV radiation shield in the upper atmosphere, tropospheric or low level ozone is hazardous to human respiratory function and is destructive towards organic materials including plastics and latex. One natural mechanism that can remove nitrogen dioxide from the air is rain. However, water reacts with nitrogen dioxide to form nitric acid (HNO_3), contributing to acid rain. Thus, in addition to the direct health hazards that nitrogen dioxide presents, its presence in the atmosphere indirectly contributes to compound effects that may be equally undesirable or worse.

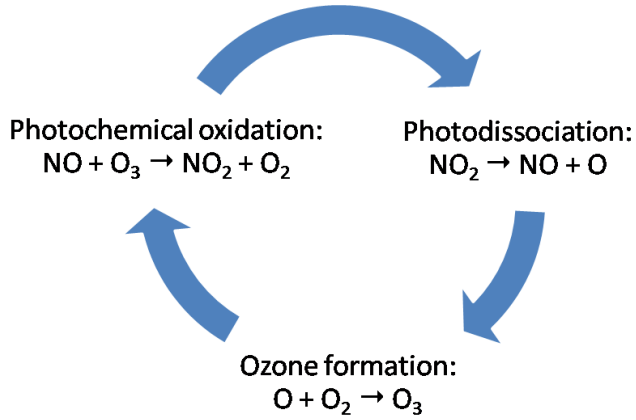

Figure 1.3: Nitrogen dioxide in the atmosphere participates in a nitrogen cycle that contributes to ozone production. While ozone is beneficial in shielding solar UV radiation in the upper atmosphere, it is a harmful pollutant in the lower atmosphere.

1.1.3 Nitrogen dioxide in the workplace

Aside from natural and anthropogenic sources releasing nitrogen dioxide in the atmosphere, perhaps the most significant risk of nitrogen dioxide to human health occurs in industrial settings, particularly in the space and rocket industry, where the storage and handling of large volumes of dinitrogen tetroxide (N_2O_4) is common place. Nitrogen tetroxide exists in equilibrium with and readily dissociates into nitrogen dioxide when leaks occur. For this reason, the U.S. military specifies that 1 ppm nitrogen dioxide should be detected upon nitrogen tetroxide leakage in military specification: MIL-PRF-26539F [9]. Nitrogen tetroxide is commonly used as the hypergolic oxidizer component in high performance hydrazine-based rocket propellants. Its use is expected to extend into future NASA projects, commercial space projects, as well as various military missile projects. This serves as an additional factor for sensors to detect and monitor nitrogen dioxide, particularly in static contained work and storage environments.

1.2 Iron phthalocyanine based sensors

The family of metal-substituted phthalocyanines (MPc) has been found to be highly reactive with strong oxidizing gases such as nitrogen dioxide [10, 11]. Iron phthalocyanine (FePc) belongs to this family of organic molecular solids. Its composition consists of hydrogen, carbon, nitrogen, and substituted iron (II) arranged into a macrocycle. The chemical notation of FePc is $C_{32}H_{16}N_8Fe$. Figure 1.4 shows its molecular structure.

Under vacuum and without the presence of oxidizing gas dopants, FePc thin films have been found to possess band gap energies greater than 3 eV. In this state it can be considered non-conducting. However, the presence of strong electron accepting gases such as nitrogen dioxide effectively dopes FePc thin films, increasing the FePc film's conductivity by many orders of magnitude. The conductivity of FePc can be described via an electron donor-acceptor mechanism, where free electrons in the FePc molecule participate in pi-bonding with nitrogen dioxide gas molecules, forming hole charge carriers that are highly mobile

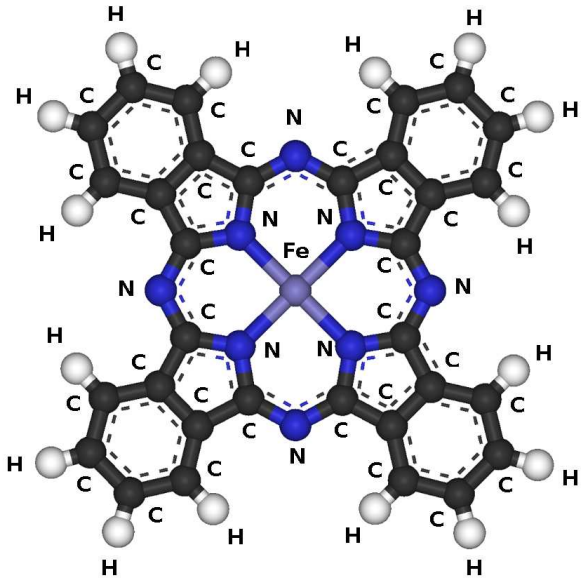

Figure 1.4: FePc is a planar molecule that occupies a square lattice with dimensions of approximately 1.3 by 1.3 nm. The substitution of Fe(II) in the center produces two holes in a $3d_{x^2-y^2}$ orbital [12].

[10, 11, 13, 14]. FePc thin films can thus be utilized in an extrinsic p-type semiconductor sensor, serving as the active sensing element that responds to nitrogen dioxide gas.

1.3 A passive sensor for nitrogen dioxide detection

Though MPcs have been found to be highly sensitive nitrogen dioxide sensors, researchers have generally focused on thermally controlled MPc sensors which operate based on substrate heating and cooling to achieve sensing and cleansing cycles [15, 16]. Heating the MPc film provides the thermodynamic conditions necessary for improved sensor reversibility and recovery, and at sufficiently elevated temperatures, near real time concentration determination may be achieved due to improved gas adsorption-desorption kinetics. Such active systems have been designed for monitoring nitrogen dioxide concentrations in environments where a continuous power source and a monitoring system are available [17, 18, 19, 20]. However, active heating of MPc films tends to cause deterioration of film stability and reduce sensor longevity as film structure is altered during operation [21, 22]. For the purpose of

detecting nitrogen dioxide leaks in industrial or military settings within storage containers or closed environments, such as in satellites, rockets or missile silos, and industrial settings, a new passive sensor approach can be advantageous. Such applications typically employ an external container filled with inert nitrogen gas designed to contain leaks. For cost-effectiveness and long life, passive FePc sensors may be placed within the external container and monitored without a constant power source, to serve as a simple unsafe nitrogen dioxide level indicator. A suitable passive sensor should also remain stable and responsive within a large temperature range, due to the lack of substrate heating. Due to its inherent stability, FePc thin films can provide the temperature stability necessary for operation over large temperature ranges.

1.4 Research Objectives

In this research, a passive, chemical resistance based, thin film FePc sensor was designed and fabricated. The primary objectives of this research are to produce a thin film FePc sensor that can:

1. Provide accurate monitoring of hazardous levels of nitrogen dioxide gas of around 1 ppm in concentration.

2. Remain stable and sensitive at operating temperatures between -46 and 71°C.

3. Be able to perform long term passive sensing in the absence of an external continuous power source for measurement or for heating.

These objectives can be achievable due to the nature of FePc thin films. The concentration of one part per million nitrogen dioxide gas is the target concentration for detection, due to its adoption as the exposure limit by several health agencies for regular work conditions. Since MPc thin films have been shown to possess the sensitivity to reliably detect nitrogen dioxide concentrations in the part per billion range, a FePc thin film sensor should be capable of detecting 1 ppm even in a non-reversing, passive mode of sensing. The operating

temperature range of -46 to 71 °C has been identified as the minimum and maximum temperatures for a diurnal cycle by military specifications, and is regarded as the most stringent operating condition specification that sensor systems should withstand. Vacuum sublimed FePc thin films are stable up to 330 °C, well above the operating temperature range specified. Sub-zero temperature gas detection with MPc thin films have yet to be performed in literature, yet FePc thin films are expected to retain stability at such low temperatures and there is no indication that nitrogen dioxide adsorption mechanics could not work on FePc at these temperatures. Lastly, to attempt long term passive sensing without an external continuous power source represents a new approach towards sensing nitrogen dioxide gas with MPc thin films that has not been documented before. As a whole, the demonstration of a reliable, passively operated nitrogen dioxide sensor based on FePc thin films can introduce new insight into the field of MPc gas sensors.

References

[1] W. H. Organization, *Air Quality Guidelines - Global Update 2005: Particulate matter, ozone, nitrogen dioxide, and sulfur dioxide*. World Health Organization, 2006.

[2] N. N. Hansel, P. N. Breysse, M. C. McCormack, E. C. Matsui, J. Curtin-Brosnan, D. L. Williams, J. L. Moore, J. L. Cuhran, and G. B. Diette, "A longitudinal study of indoor nitrogen dioxide levels and respiratory symptoms in inner-city children with asthma," *Environmental Health Perspectives*, vol. 116, no. 10, 2008.

[3] K. Belanger, J. F. Gent, E. W. Triche, M. B. Bracken, and B. P. Leaderer, "Association of indoor nitrogen dioxide exposure with respiratory symptoms in children with asthma," *American Journal of Respiratory and Critical Care Medecine*, vol. 173, pp. 297–303, 2006.

[4] S. Solomon, D. Qin, M. Manning, Z. Chen, M. Marquis, K. Averyt, M. Tignor, and H. Miller, *Climate Change 2007 - The Physical Science Basis*. Cambridge University Press, Cambridge, United Kingdom and New York, NY, USA, 2007.

[5] N. Gruber and J. N. Galloway, "An earth-system perspective of the global nitrogen cycle," *Nature*, vol. 451, pp. 293–296, 2008.

[6] J. Garthwaite and C. L. Boulton, "Nitric oxide signaling in the central nervous system," *Annual Review of Physiology*, vol. 57, no. 1, pp. 683–706, 1995.

[7] S. J. Neill, R. Desikan, A. Clarke, R. D. Hurst, and J. T. Hancock, "Hydrogen peroxide and nitric oxide as signalling molecules in plants," *J. Exp. Bot.*, vol. 53, no. 372, pp. 1237–1247, 2002.

[8] D. F. Klessig, J. Durner, R. Noad, D. A. Navarre, D. Wendehenne, D. Kumar, J. M. Zhou, J. Shah, S. Zhang, P. Kachroo, Y. Trifa, D. Pontier, E. Lam, and H. Silva, "Nitric oxide and salicylic acid signaling in plant defense," *Proceedings of the National Academy of Sciences of the United States of America*, vol. 97, no. 16, pp. 8849–8855, 2000.

[9] "Mil-prf-26539f performance specification - propellants, dinitrogen textroxide," 2006.

[10] B. Bott and T. Jones, "A highly sensitive nitrogen dioxide sensor based on electrical conductivity changes in phthalocyanine films," *Sensors and Actuators*, vol. 5, pp. 43–53, 1984.

[11] T. Jones and B. Bott, "Gas-induced electrical conductivity changes in metal phthalocyanines," *Sensors and Actuators*, vol. 9, pp. 27–37, 1986.

[12] G. Dufour, C. Poncey, F. Rochet, H. Roulet, S. lacobucci, M. Sacchi, F. Y. N. Motta, M. Piancastelli, A. Sgarlata, and M. D. Crescenzi, "Metal phthalocyanines (mpc, m=ni, cu) on cu(001) and si(001) surfaces studied by xps, xas and stm," *Journal of Electron Spectroscopy and Related Phenomena*, vol. 76, pp. 219–224, 1995.

[13] R. L. V. Ewyk, A. V. Chadwick, and J. D. Wright, "Electron donor-acceptor interactions and surface semiconductivity in molecular crystals as a function of ambient gas," *J. C. S. Faraday Transactions I*, vol. 76, pp. 2194–2205, 1980.

[14] M. F. Craciun, S. Rogge, and A. F. Morpurgo, "Correlation between molecular orbitals and doping dependence of the electrical conductivity in electron-doped metal-phthalocyanine compounds," *Journal of the American Chemical Society*, vol. 127, pp. 12210–12211, 2005.

[15] Y. Sadaoka, T. Jones, and W. Gopel, "Fast nitrogen dioxide detection at room temperature with optimized lead phthalocyanine thin-fllm structures," *Sensors and Actuators B*, vol. 1, pp. 148–153, 1990.

[16] A. Wilson, J. D. Wright, and A. V. Chadwick, "A microprocessor-controlled nitrogen dioxide sensing system," *Sensors and Actuators B*, vol. 4, pp. 499–504, 1991.

[17] A. Heilmann, V. Lantto, M. Muller, and C. Hamann, "Nitrogen dioxide monitoring as an air pollutant using lead phthalocyanine thin film sensors," *Sensors and Actuators B*, vol. 7, pp. 522–525, 1992.

[18] G. Barillaro and L. Strambini, "An integrated cmos sensing chip for nitrogen dioxide detection," *Sensors and Actuators B: Chemical*, vol. 134, pp. 585–590, 2008.

[19] J. Brunet, V. P. Garcia, A. Pauly, C. Varenne, and B. Lauron, "An optimised gas sensor microsystem for accurate and real-time measurement of nitrogen dioxide at ppb level," *Sensors and Actuators B: Chemical*, vol. 134, pp. 632–639, 2008.

[20] N. Padma, A. Joshi, A. Singha, S. Deshpandec, D. Aswala, S. Guptaa, and J. Yakhmia, "NO_2 sensors with room temperature operation and long term stability using cupc thin films," *Sensors and Actuators B*, vol. 143(1), pp. 246–252, 2009.

[21] A. de Haan and A. Decroly, "Electrical resistance of copper phthalocyanine thin films as influenced by substrates, electrodes and physical features of the films," *Sensors and Actuators B*, vol. 30, pp. 143–150, 1996.

[22] Y.-L. Lee and C.-H. Chang, "Nitrogen dioxide sensing characteristics of copper phthalocyanine films: Effects of low temperature annealing and doping time," *Sensors and Actuators B*, vol. 119, pp. 174–179, 2006.

Chapter 2

Fundamentals of Vapor Deposited FePc Thin Films

FePc thin films possess many desirable properties for use in chemical gas sensors. FePc thin films show good thermal stability; vaporization at standard atmospheric conditions only occurs at temperatures above 300°C. FePc thin films can be fabricated to possess morphologies with high specific surface areas useful for increasing gas adsorption capability. The ease of incorporation of FePc thin films into existing microelectronics fabrication techniques is another advantage. FePc thin films can be deposited onto semiconductor substrates via established physical vapor deposition techniques. Perhaps the most important property of FePc thin films is their excellent sensitivity towards highly oxidizing gases and the reliability of its chemical to electrical transduction mechanism. The following sections will provide fundamental background information on vapor deposited FePc thin films.

2.1 Vapor deposition of FePc

Vapor deposition of FePc in a vacuum, also referred to as vacuum sublimation, is an established method for fabricating MPc thin films due to its simplicity and ability to control various film properties, namely thickness, crystal structure, and morphology. It is a well established method for producing thin films on microelectronic substrates. Vacuum sublimation of FePc is accomplished by heating FePc powder under low vacuum pressures and allowing the emitted vapor to solidify onto a substrate. FePc powder is normally held in a resistance heated target holder that is heated by the application of current. For reference, FePc powder sublimes at roughly 250 to 300 °C for pressures around $5x10^{-6}$ Torr. At these low sublimation temperatures and normal vacuum pressures, FePc fabrication can be performed inexpensively with standard physical vapor deposition systems without relying on

state-of-the-art technology. Film thickness can be monitored in real time during deposition, with help from installed thickness monitoring devices such as a quartz crystal microbalance. A fairly standard quartz crystal microbalance has the precision to detect coating rates as low as 0.1 nm/s and monitor overall thicknesses in excess of one micron. By carefully monitoring deposition rates and film thickness while adjusting input current to the target holder, FePc films can be accurately reproduced.

2.2 Crystal structure

FePc is a planar MPc molecule [1]. For planar MPc's, the crystal structure of vacuum sublimed thin films generally assumes an α or a β phase. These two phases are polymorphs, and for MPcs, the α phase has been determined to be metastable while the β phase is stable [2, 3]. α-MPc thin films can be obtained via vapor deposition onto non-interacting substrates, such as amorphous silicon dioxide, at room temperature or lower. To achieve β-MPc thin films however, substrate heating during vapor deposition or post deposition annealing is required [4]. Alternatively, exposure to certain organic solvent vapors may induce α to β phase transition [2]. For gas sensor applications, both polymorphs have its advantages. Research has shown that α-MPc films exhibit higher analyte adsorption induced conductivity change, while β-MPc possesses better stability, response rate, and reversibility characteristics [5, 6]. These characteristics can be attributed to the crystal structure of each film. Figures 2.1(a), 2.1(b), and 2.1(c) show the crystal structure of α-FePc; Figures 2.1(d), 2.1(e), and 2.1(f) show the crystal structure of β-FePc.

From the figures, β-FePc exhibits a larger stacking angle than α-FePc, and since intermolecular spacing is the same, the result is a directionally oriented structure. The α-FePc crystal forms a monoclinic unit cell belonging to the C2/c space group, with four FePc molecules per unit cell. The β-FePc crystal structure forms a monoclinic unit cell belonging to a $P2_1/a$ space group, with two FePc molecules per unit cell. Due to the stacking angle differences, the π orbital overlap between stacked α-FePc molecules is greater than between

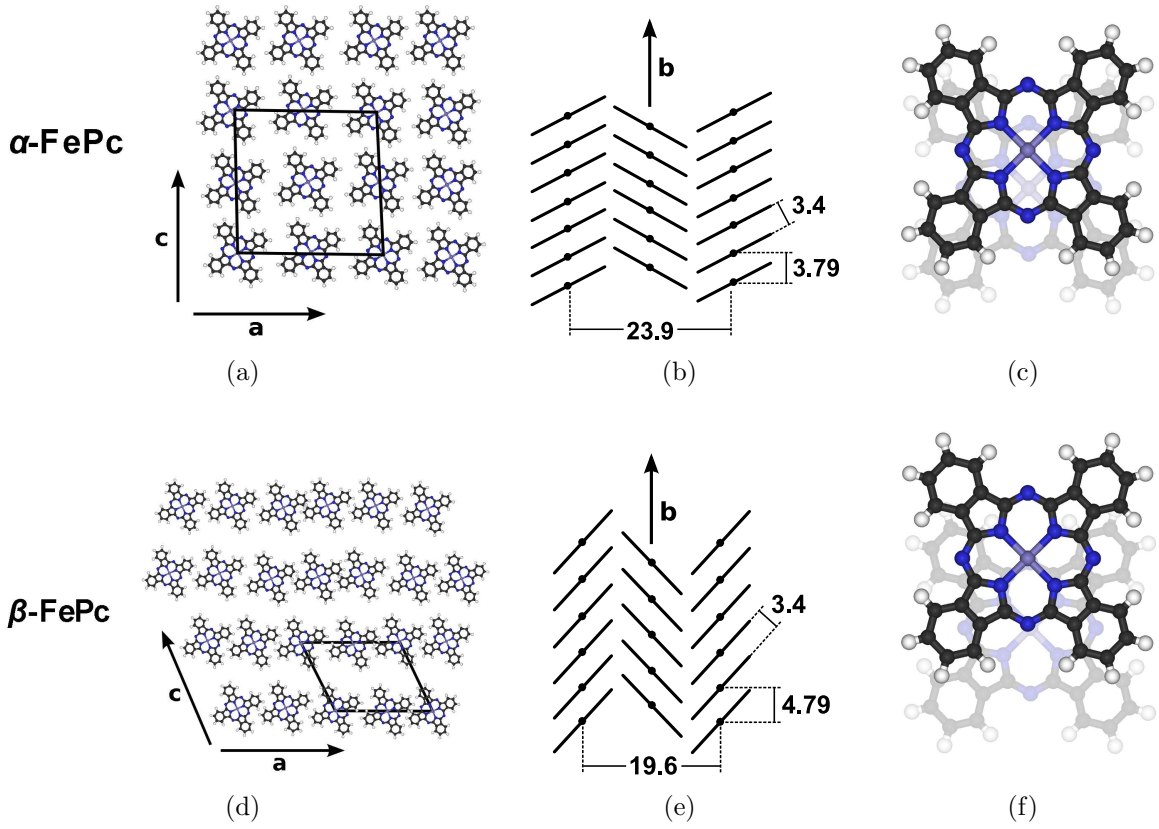

(a) (b) (c)

(d) (e) (f)

Figure 2.1: FePc has the same crystal structure as typical planar MPc's, as shown here elucidated by x-ray diffraction analysis [7]. Two polymorphs exist, with α-FePc shown in (a), (b), and (c) being the metastable phase and β-FePc shown in (d), (e), and (f) being the stable phase. The α-FePc crystal forms a monoclinic unit cell belonging to the C2/c space group, with four FePc molecules per unit cell. The β-FePc crystal structure forms a monoclinic unit cell belonging to a $P2_1/a$ space group, with two FePc molecules per unit cell. The crystal structures are similar with the only difference being that of the stacking angle. The primary difference between the two phases lies in the stacking angle along the stacking axis b. Due to the stacking angle differences, the π orbital overlap between α-FePc molecules is greater than in β-FePc molecules. In theory and in experiment, this results in α-FePc crystals possessing better conductivity characteristics along the stacking axis.

stacked β-FePc molecules. In theory and in experiment, this results in α-FePc crystals possessing better conductivity characteristics along the stacking axis. It is also due to the stacking angle that the α crystals tend to grow as grains while β crystals tend to grow into long whiskers as growth is more confined to similar orientations [4, 8]. The small difference in crystal structure thus leads to significant differences in film morphology, and will be discussed in more detail in the next section.

2.3 Film morphology

Film morphology of vacuum sublimed FePc thin films varies greatly depending on several factors. These factors primarily consist of underlying substrate type, substrate heating during deposition, film thickness, deposition rate, and any subsequent heat treatment. In general, these parameters ultimately affect FePc thin film morphology by affecting how FePc molecules are arranged onto a substrate. Figure 2.2 illustrates three ways by which vacuum sublimed FePc thin films adhere and orient themselves onto a substrate. The first example in Figure 2.2(a) depicts a stacking orientation perpendicular to the substrate, typical for thicker films processed at higher deposition rates onto normal non-interacting substrates. The second example in Figure 2.2(b) shows a stacking orientation parallel to the substrate, typical of thinner films processed at lower deposition rates onto very smooth and non-interacting substrates. The last example illustrates a film stacked at an angle, typical of deposition onto strongly interacting substrates or heated substrates. The b-axis is the stacking direction and the preferred growth direction for each FePc thin film orientation. Therefore, depending on which type of morphology is preferred for a given application, processing parameters such as substrate type, substrate heating, film thickness, deposition rate, or subsequent heat treatment can be optimized.

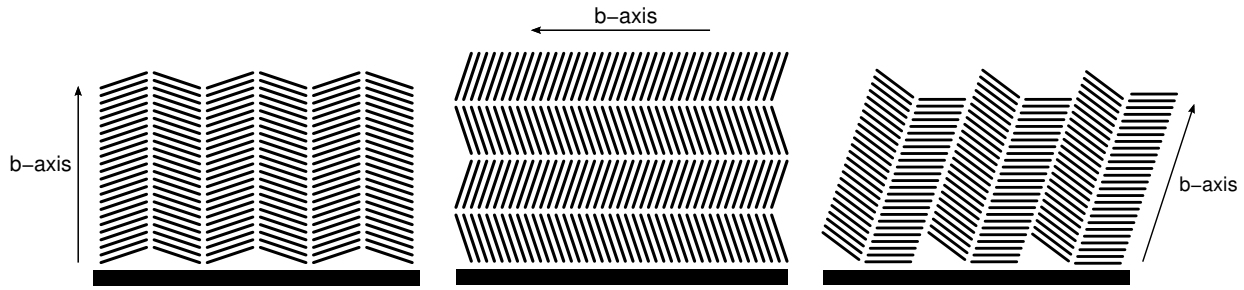

Figure 2.2: FePc stacking orientation on substrates can vary depending greatly on the strength of interaction with the substrate. This in turn leads to morphological differences. (a) Stacking orientations perpendicular to the substrate is typical for thicker films processed at higher deposition rates onto general non-interacting substates. (b) Stacking orientations parallel to the substrate is typical of thinner films processed at lower deposition rates onto very smooth and non-interacting substrates. (c) Films with stacking orientation at an angle with respect to the substrate is typical of deposition onto strongly interacting substrates or heated substrates. In each case, the stacking axis and the preferred growth direction is denoted by the b-axis vector.

2.3.1 Substrate type effects

For sensor applications, MPc thin films and metal electrodes are normally vacuum sublimed onto stable insulating ceramic substrates such as glass [9, 10, 11], quartz [8], oxidized silicon [12, 13, 14], or alumina [15, 16, 17]. With the exception of rough alumina substrates, these insulating substrates are considered non-interacting and rather smooth, resulting in microcrystalline α-FePc thin films when deposited at room temperature at low deposition rates. These thin films possess fairly consistent grain size typically in the range of 20-150 nm, depending on film thickness. As thickness is increased, grain growth proceeds in the direction perpendicular to the thin film plane. One thing worth noting is that the type of doping on the silicon substrate can affect the grain size of vacuum sublimed MPc thin films. Less than a one nanometer of oxidized silicon on p-type and n-type silicon substrates has been found to affect grain sizes on 16 nm MPc films, with larger grains on n-type substrates of roughly 75-150 nm and smaller grains on p-type substrates in the range of 50-100 nm [18]. However, with thicker oxidized silicon layers and thicker vacuum sublimed FePc films, silicon doping plays more of a role in silicon oxidation rates [19], while the effect of silicon doping

on FePc film morphology drastically diminishes, due to the amorphous nature of oxidized silicon.

2.3.2 Film thickness effects

Vacuum sublimed MPc films at room temperature form small α phase grains that gradually increase in size and form vertical rod structures as film thickness increases [6]. This trend was observed during preliminary experiments of FePc vacuum sublimation onto silicon dioxide substrates. For a visual comparison showing grain growth evolution as film thickness increases, SEM images at 80,000x magnification are shown in Figure 2.3. The evolution of morphology due to increasing thickness has a significant effect on the electrical conductivity of FePc thin films. In preliminary experiments, thicker films have exhibited lower conductivity values when saturated with nitrogen dioxide, suggesting that thicker films have a morphology that provides more conducting pathways. Furthermore, thicker MPc films of 200 nm and higher also show much less reversibility compared to thinner films, indicating that thicker films either possess more defects and thus more preferential adsorption sites or that target gas molecules have penetrated into the bulk and have difficulty diffusing out.

2.3.3 Substrate heating effects

Substrate temperature during deposition has great affect on the morphology of vacuum sublimed MPc films. As discussed in the previous section, at room temperatures, vacuum sublimed MPc films on glass substrates form small α phase grains that gradually increase in size and form vertical rod structures as thickness increases [6], while at substrate temperatures above 100 °C, β phase whiskers become increasingly prevalent as substrate temperature is increased [8]. Figure 2.4 shows how heated substrates alter the morphology of a vacuum sublimed CuPc thin films.

For gas sensor applications, MPcs are typically vacuum sublimed at room temperature to produce an α phase film with many small grains. When considering conductivity change

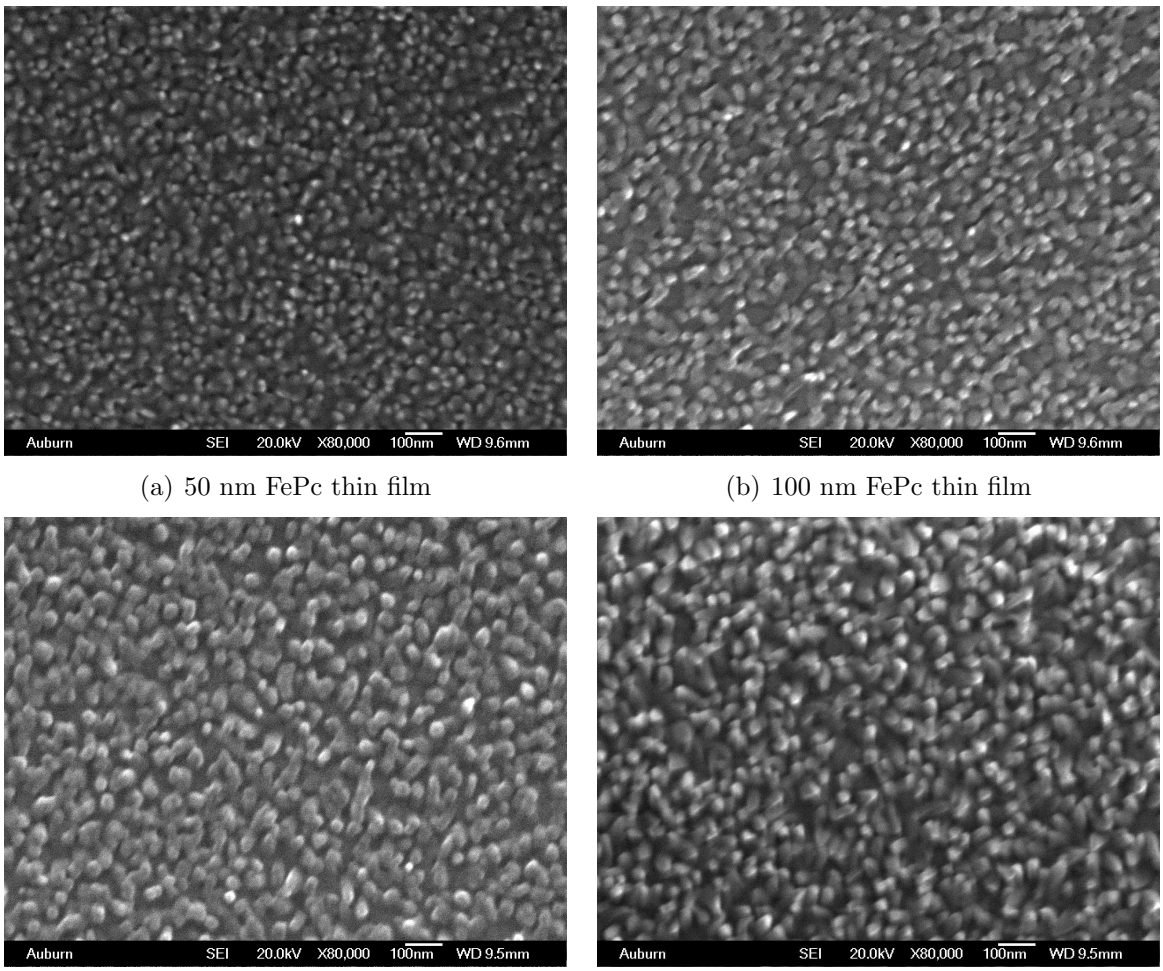

(a) 50 nm FePc thin film

(b) 100 nm FePc thin film

(c) 200 nm FePc thin film

(d) 250 nm FePc thin film

Figure 2.3: Preliminary results from scanning electron microscopy show thicker FePc thin films having larger grains and greater surface roughness, as rod-like structures grow both vertically away from the thin film plane and horizontally in size. These FePc thin films have been vacuum sublimed onto silicon dioxide substrates at room temperature, and are in the α phase.

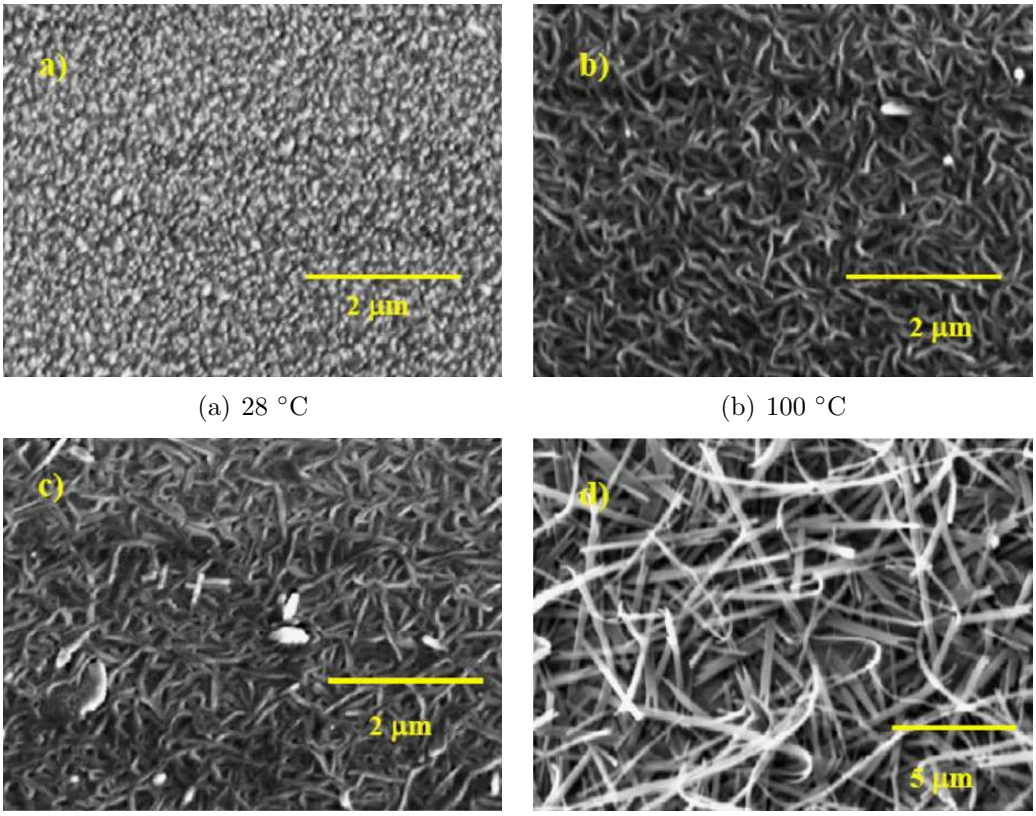

(a) 28 °C

(b) 100 °C

(c) 150 °C

(d) 200 °C

Figure 2.4: These SEM images taken by the author show the effects of substrate heating on the morphology of vacuum sublimed CuPc thin films [8]. In the absence of substrate heating, α phase CuPc grows grains with a relatively uniform size distribution. When the substrate is heated above 100 °C, β phase whiskers grow during vacuum sublimation. Further heating of the substrate results in more prevalent directional growth of these β phase whiskers.

and reproducibility, an α phase thin film is more suitable although the β phase can be more stable. As shown in in Figure 2.4, substrate heating results in whiskers and fibers that grow randomly. To achieve both a large conductivity change as well as good film stability, researchers have resorted to post-deposition annealing.

2.3.4 Deposition rate effects

Without substrate heating, the effect of deposition rate on MPc films is such that faster rates decrease the grain size and crystallinity of the thin film [20]. The cause can be attributed to the lack of adequate time and thermodynamic conditions for vacuum sublimed MPc particles at high deposition rates to diffuse and align itself within the structure of existing grains. The result is a film that is more conductive as oxidizing gas molecules are adsorbed, yet also much less stable due to more defects. Research has shown that for CuPc films deposited at rates greater than 2 nm/s, the film resistivity is drastically reduced, and further increases in deposition rate tend to be inconsequential, as the film cannot be more disordered [21]. For slow deposition processes ranging from 0.1-1 nm/s without substrate heating however, studies have shown that MPcs would form α phase grains that grow into rods as thickness is increased, and generally follow the surface geometry of the substrate [6]. Since this type of morphology provides the best balance between high specific surface area for gas adsorption and greater crystallinity for better stability, it is advisable to perform vacuum sublimation of MPc thin films at deposition rates less than 1 nm/s for gas sensor applications.

2.3.5 Post-deposition annealing effects

Post deposition annealing has been shown to induce α to β transition in MPc thin films at temperatures as low as 100 °C and up to 350 °C [22, 23]. To achieve both conductivity change in α films as well as the stability of β films, researchers have resorted to post-deposition annealing [24]. The results have been encouraging, and furthermore, the

transformed β film seemed to be less susceptible to oxygen doping. However, studies have shown that above a certain film thickness of approximately 100 nm, the grain size and grain separation within the MPc thin film does not allow the α to β phase transition to occur completely [4].

2.4 Conduction mechanism

The anisotropic nature of FePc molecular solids suggest a complex conduction mechanism. Within a FePc molecule, the covalent bonding between carbon and nitrogen, as well as the presence of the central iron ion result in many π orbitals located throughout the molecule [25]. From Figure 2.1, it is observed that b-axis stacking of FePc molecules can cause significant π orbital overlap, more so in α-FePc than in β-FePc, resulting in enhanced conductivity along the stacking direction. While the occurrence of conductivity across π orbital overlap can be explained and modeled with the application of band theory, conductivity in the a and c-axes can occur, but is based on an entirely different mechanism. Because charge carriers have a tendency to become localized in a FePc molecular solid due to low mobilitys, a hopping or tunneling mechanism occurs for conduction along the a and c-axes. Thus, the conduction mechanism in FePc thin films depends greatly on the direction in which conductivity is occurring as well as on the ordering of a thin film.

For FePc thin films obtained via vacuum sublimation onto non-interacting substrates, the film typically assumes an amorphous microcrystalline morphology dominated by small grains and many orientations. The intrinsic conductivity in amorphous microcrystalline FePc thin films is therefore be expected to be quite low. The presence of electron accepting oxidizing gases however, can greatly increase the conductivity of a FePc thin film. Up to eight orders of magnitude change has been observed upon exposure to oxidizing gases. It is determined from Raman spectroscopy, that oxidizing gases such as nitrogen dioxide tend to interact with the π orbitals in the periphery of the MPc molecule rather than coordinating with the central metal ion, although higher oxidation states in the metal ion can enhance

the donor power of the MPc [2, 26]. With the stacking structure and high surface area to bulk morphology of FePc grains, an abundance of nitrogen dioxide adsorption sites exist, and the amount of charge carrier complexes formed via adsorption can significantly increase the conductivity of amorphous microcrystalline films.

References

[1] D. R. Tackley, G. Dent, and W. E. Smith, "Phthalocyanines: structure and vibrations," *Physical Chemistry Chemical Physics*, vol. 8, pp. 1419–1426, 2001.

[2] C. Leznoff and A. Lever, eds., *Phthalocyanines: Properties and Applications*. VCH Publishers, 1989.

[3] F. Iwatsu, "Size effects on the alpha to beta transformation of phthalocyanine crystals," *The Journal of Physical Chemistry*, vol. 98 (6), pp. 1678–1681, 1998.

[4] S. Heutz, S. M. Bayliss, R. L. Middleton, G. Rumbles, and T. S. Jones, "Polymorphism in phthalocyanine thin films - mechanism of the alpha to beta transition," *Journal of Physical Chemistry B*, vol. 104, pp. 7124–7129, 2000.

[5] Y.-L. Lee, W.-C. Tsai, and J.-R. Maab, "Effects of substrate temperature on the film characteristics and gas-sensing properties of copper phthalocyanine films," *Applied Surface Science*, vol. 173, pp. 352–361, 2001.

[6] Y.-L. Lee, C.-Y. Hsiao, and R.-H. Hsiao, "Annealing effects on the gas sensing properties of copper phthalocyanine films," *Thin Solid Films*, vol. 468, pp. 280–284, 2004.

[7] J. K. O'Rourke, J. Brooks, N. Bell, J. Cawley, and S. C. Thorpe, "Mossbauer and microstructural studies of iron phthalocyanine as a potential gas sensor," *Sensors and Actuators B*, vol. 13-14, pp. 690–692, 1993.

[8] N. Padma, A. Joshi, A. Singha, S. Deshpandec, D. Aswala, S. Guptaa, and J. Yakhmia, "NO_2 sensors with room temperature operation and long term stability using cupc thin films," *Sensors and Actuators B*, vol. 143(1), pp. 246–252, 2009.

[9] A. Belghachi and R. Collins, "The effects of humidity on phthalocyanine NO_2 and NH_3 sensors," *Journal of Physics D: Applied Physics*, vol. 23, pp. 223–227, 1990.

[10] I. Zhivkov, E. Spassova, D. Dimov, and G. Danev, "Oxygen influence on the conductivity of copper phthalocyanine vacuum-deposited thin films," *Vacuum*, vol. 76, p. 237240, 2004.

[11] A. C. Varghese and C. Menon, "Electrical properties of iron phthalocyanine thin film device using gold and aluminium electrodes," *Journal of Materials Science: Materials in Electronics*, vol. 18, pp. 587–592, 2007.

[12] J. Martensson, H. Arwin, and I.Lundstrom, "Thin films of phthalocyanines studied with spectroscopic ellipsometry: an optical gas sensor?," *Sensors and Actuators B*, vol. 1, pp. 134–137, 1990.

[13] H.-Y. Wang and J. B. Lando, "Gas-sensing mechanism of phthalocyanine langmuir-blodgett films," *Langmuir*, vol. 10, pp. 790–796, 1994.

[14] C. Moldovan, L. Hinescu, M. Hinescu, R. Iosub, M. Nisulescu, B. Firtat, M. Modreanu, D. Dascalu, V. Voicu, and C. Tarabasanu, "Silicon micromachined sensor for gas detection," *Materials Science and Engineering B*, vol. 101, pp. 227–231, 2003.

[15] S. Dogo, J. P. Germain, C. Maleysson, and A. Pauly, "Gas-sensing properties of metallophthalocyanine thin films as a function of their crystalline structure," *Sensors and Actuators B*, vol. 8, pp. 257–259, 1992.

[16] C. J. Liu, J. C. Hsieh, and Y. H. Ju, "Response characteristics of lead phthalocyanine gas sensor - effect of operating temperature and postdeposition annealing," *Journal of Vacuum Science and Technology A*, vol. 14(3), pp. 753–756, 1996.

[17] K.-C. Ho and Y.-H. Tsou, "Chemiresistor-type no gas sensor based on nickel phthalocyanine thin films," *Sensors and Actuators B*, vol. 77, pp. 253–259, 2001.

[18] M. Krzywiecki, L. Ottaviano, L. Grzadziel, P. Parisse, S. Santucci, and J. Szuber, "Influence of substrate doping on the surface chemistry and morphology of copper phthalocyanine ultra thin films on si (111) substrates," *Thin Solid Films*, vol. 517, no. 5, pp. 1630 – 1635, 2009.

[19] B. E. Deal and M. Sklar, "Thermal oxidation of heavily doped silicon," *Journal of The Electrochemical Society*, vol. 112, no. 4, pp. 430–435, 1965.

[20] G. E. Collins, N. R. Armstrong, J. W. Pankow, C. Oden, R. Brina, C. Arbour, and J.-P. Dodelet, "Thin film sensors: The role of defects and impurity sites in controlling sensor response and selectivity," *American Vacuum Society*, vol. 11, no. 4, pp. 1383–1391, 1993.

[21] A. de Haan and A. Decroly, "Electrical resistance of copper phthalocyanine thin films as influenced by substrates, electrodes and physical features of the films," *Sensors and Actuators B*, vol. 30, pp. 143–150, 1996.

[22] Y.-L. Lee and C.-H. Chang, "Nitrogen dioxide sensing characteristics of copper phthalocyanine films: Effects of low temperature annealing and doping time," *Sensors and Actuators B*, vol. 119, pp. 174–179, 2006.

[23] K. Manandhar, T. Ellis, K. Park, T. Cai, Z. Song, and J. Hrbek, "A scanning tunneling microscopy study on the effect of post-deposition annealing of copper phthalocyanine thin films," *Surface Science*, vol. 601, p. 36233631, 2007.

[24] Y.-L. Lee, W.-C. Tsai, C.-H. Changb, and Y.-M. Yangb, "Effects of heat annealing on the film characteristics and gas sensing properties of substituted and un-substituted copper phthalocyanine films," *Applied Surface Science*, vol. 172, pp. 191–199, 2001.

[25] J. Ahlund, K. Nilson, J. Schiessling, L. Kjeldgaard, S. Berner, N. Martensson, C. Puglia, B. Brena, M. Nyberg, and Y. Luo, "The electronic structure of iron phthalocyanine probed by photoelectron and x-ray absorption spectroscopies and density functional theory calculations," *The Journal of Chemical Physics*, vol. 125, p. 034709, 2006.

[26] T. Basova, E. Koltsov, and I. Igumenov, "Spectral investigation of interaction of cupc with nitrogen dioxide," *Sensors and Actuators B*, vol. 105, p. 259265, 2005.

Chapter 3

Sensor design

The nitrogen dioxide gas sensor in this research consists of an active layer of FePc thin film deposited upon a gold inter-digitated electrode pattern. The interaction between FePc and nitrogen dioxide gas is that of a surface adsorption induced charge-carrier transfer complex [1, 2], thus nitrogen dioxide gas molecules adsorbed onto FePc films effectively dopes the film, enhancing its electrical conductivity. The changes in electrical properties are monitored via resistance measurements across the underlying electrodes. Based on such a working principle, the design considerations for this sensor lie primarily in three areas: the type of sensor substrate, the electrode pattern, and the type of FePc thin film active layer.

3.1 Sensor substrate

The sensor substrate is important because it acts as the base upon which the various sensor components come together. The sensor substrate should be an electrical insulator with resistivity significantly higher than the FePc thin film active layer. The substrate should also have good adhesion compatibility with the electrode structure. Furthermore, the thermal expansion coefficient of the substrate should be sufficiently low so that the sensor can remain stable within the operating temperature range of -46 to 71 °C. Lastly, the substrate morphology should be relatively smooth to allow for vacuum sublimation of a uniform FePc thin film. Due to these requirements, an oxidized silicon substrate and a quartz substrate were both chosen to be the substrate for the FePc thin film sensor. Thermally oxidized silicon is essentially amorphous silicon dioxide, and is produced by exposing silicon wafers to a high temperature environment in the presence of a controlled amount of oxygen. Oxidized silicon, with density 2.2 g/cm^3, is less dense than crystalline quartz, which has density of

2.65 g/cm^3. Oxidized silicon has a resistivity greater than 1 x $10^{20}\Omega$-cm, while quartz is only slightly lower at 7.5 x $10^{19}\Omega$-cm. The thermal expansion coefficient of both silicon dioxide and quartz are both very small at 0.5 and 0.59 ppm/K respectively. The surface roughness of oxidized silicon is found to vary with oxidation temperature and time, from a few nanometers to tens of nanometers, especially when the original silicon surface has been polished [3]. In general, oxidized silicon roughness is smoother than the typical grain size of vacuum sublimed FePc, which is typically 50 nm or more and increasing with thickness, thus it can be considered non-interfering. Such properties make oxidized silicon and quartz attractive sensor substrates. For this research, quartz and oxidized silicon, one micron thick oxidized over 400-500 micron thick wafers, are used as sensor substrates.

3.2 Electrode pattern

The physical geometry of the electrode pattern design for a FePc thin film sensor takes into account many physical considerations. As common knowledge of electrode design dictates, a larger surface area results in increased sensitivity, therefore many electrochemical sensors utilize an interdigitated finger geometry. Another advantage of interdigitated electrode designs is that the specific region within the active layer experiencing the largest conductivity increase becomes the path of least resistance. This represents a good arrangement because it allows the part of the deposited film that possesses the best conductivity characteristics to control the output signal. For the interdigitated electrode pattern, the gap spacing between the fingers should be sized according to the electrical properties of the active layer in use. For FePc thin films, with band gap energies exceeding 3 V, the film resistivity is relatively high, thus it is desirable to use a small electrode spacing such that driving voltages do not become exceedingly high and that film heating does not occur. Previous research efforts into MPc based sensors have implemented electrode spacings ranging from 25 microns to five millimeters, requiring a voltage bias ranging from 15 V to 1 V [1, 4]. For this research, a 15 micron electrode spacing and a 1 V bias is adopted. This allows

ordinary multimeters to make resistance readings without the need of a constant external voltage source, while also reducing the risk of electrically heating or altering the FePc thin film. The design for the interdigitated electrode pattern is shown in Figure 3.1.

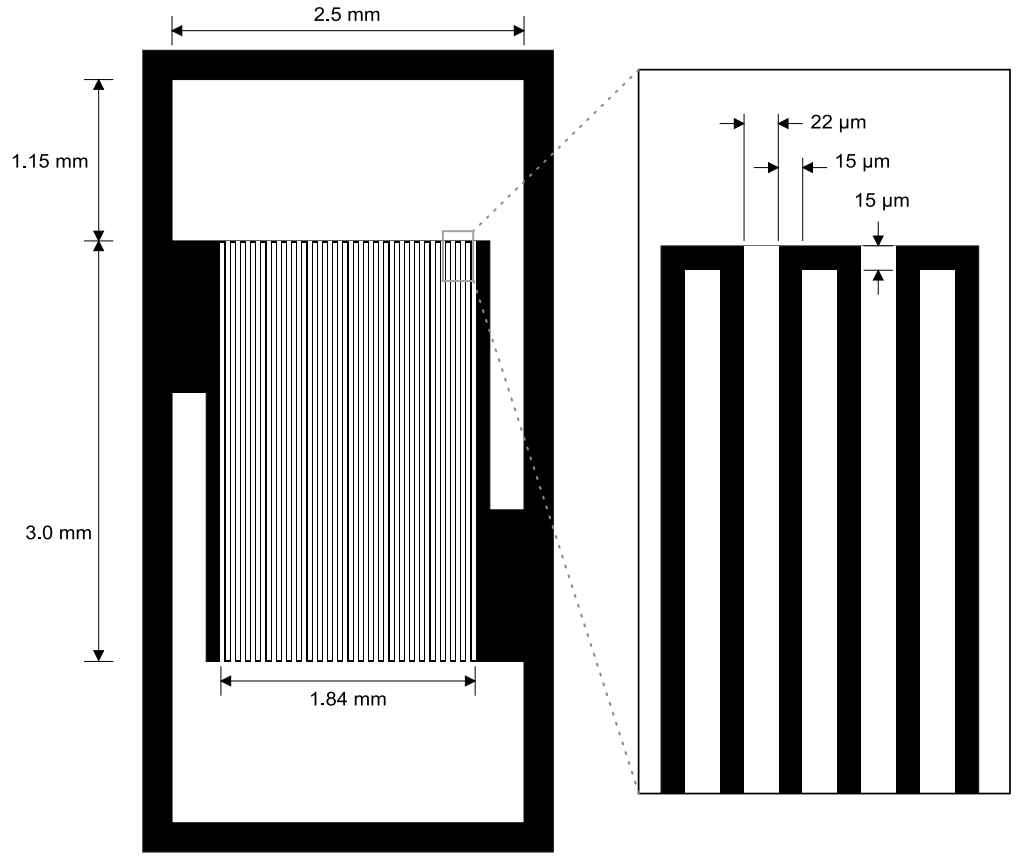

Figure 3.1: Sensor inter-digitated electrode pattern consists of two main electrode contacts for interface with measurement circuitry. The two main electrodes branch into 25 pairs of parallel electrode fingers. FePc thin film is deposited above and between the electrodes to serve as the active layer. In this design, the spacing between electrode fingers is a constant 15 microns.

The electrode height consists of a 150 nm thick layer of gold on top of a 50 nm thick titanium interlayer. The titanium interlayer serves as an important adhesion layer between the gold electrode and the oxidized silicon or quartz substrate. With a 15 micron electrode spacing, the applied voltage required for detection is within 1 V, allowing the use of simple resistance monitoring circuitry or handheld multi-meter devices. An ohmic type contact is expected at the FePc-electrode interface for a 1 V bias. For whole wafer production, a UV

mask containing 360 individual sensor patterns for use with 4" round wafers was created and used to make sensors for testing in this research.

3.3 FePc active layer

In this research, for its ease of evaporation, for good film uniformity, and for batch processing purposes, FePc thin films should be produced via vacuum sublimation onto batches of sensor substrates or entire wafers. It has been experimentally determined that as-deposited α-MPc thin films possess better sensitivity characteristics while β-MPc thin films, produced via post deposition heat treatment, exhibit better reversibility characteristics. While the former owes its sensitivity to its higher specific surface area due to its microcrystallinity, the latter owes its reversibility aspects to its more compact and stable structure. Both types of FePc film are investigated in this research. Fibrous or whisker like β-FePc thin films fabricated via substrate heating during vacuum sublimation are not considered in this research because its morphology is not compatible with the planar geometry of the electrode pattern. For passive sensors intended for use in an integrating fashion, it is postulated that α-FePc thin films are more suitable. The effect of FePc active layer thickness on morphology and gas sensitivity are worth investigating, as is post deposition heat treatment.

References

[1] B. Bott and T. Jones, "A highly sensitive nitrogen dioxide sensor based on electrical conductivity changes in phthalocyanine films," *Sensors and Actuators*, vol. 5, pp. 43–53, 1984.

[2] Y. Sadaoka, T. Jones, and W. Gopel, "Fast nitrogen dioxide detection at room temperature with optimized lead phthalocyanine thin-fllm structures," *Sensors and Actuators B*, vol. 1, pp. 148–153, 1990.

[3] Y. L. Khong, G. S. Tan, and G. A. Tan, "Surface and interfacial roughness of polished and oxidized silicon wafers evaluated by an infrared differential interference contrast technique," *Journal of The Electrochemical Society*, vol. 143, no. 11, pp. L254–L256, 1996.

[4] M. Newton, T. Starke, M. Willis, and G. McHale, "Nitrogen dioxide detection at room temperature with copper phthalocyanine thin film devices," *Sensors and Actuators B*, vol. 67, pp. 307–311, 2000.

Chapter 4

Experimental details

4.1 Fabrication of sensor

Fabrication of the sensor was based on common microelectronics fabrication procedures. Standard practices for wafer cleaning, oxidation, photolithography, and material deposition were performed primarily in the setting of a clean room at the Alabama Microelectronics Science and Technology Center (AMSTC) located in Auburn University. The main steps in the fabrication process are diagrammed in Figure 4.1. Figure 4.2 provides an illustration of the entire fabrication procedure. Experimental details regarding each procedure are documented in the following subsections.

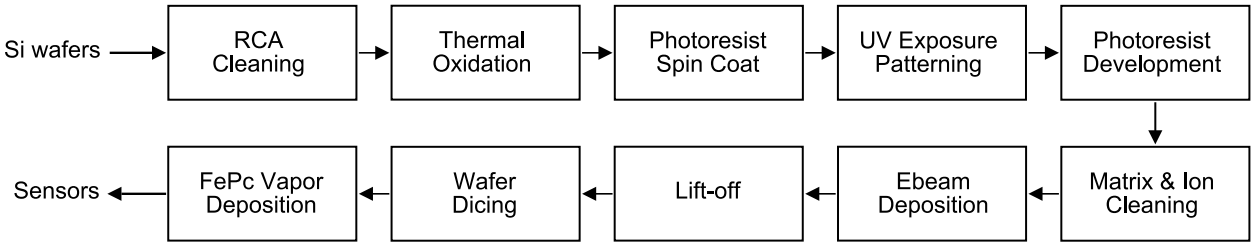

Figure 4.1: Microelectronics fabrication flow chart

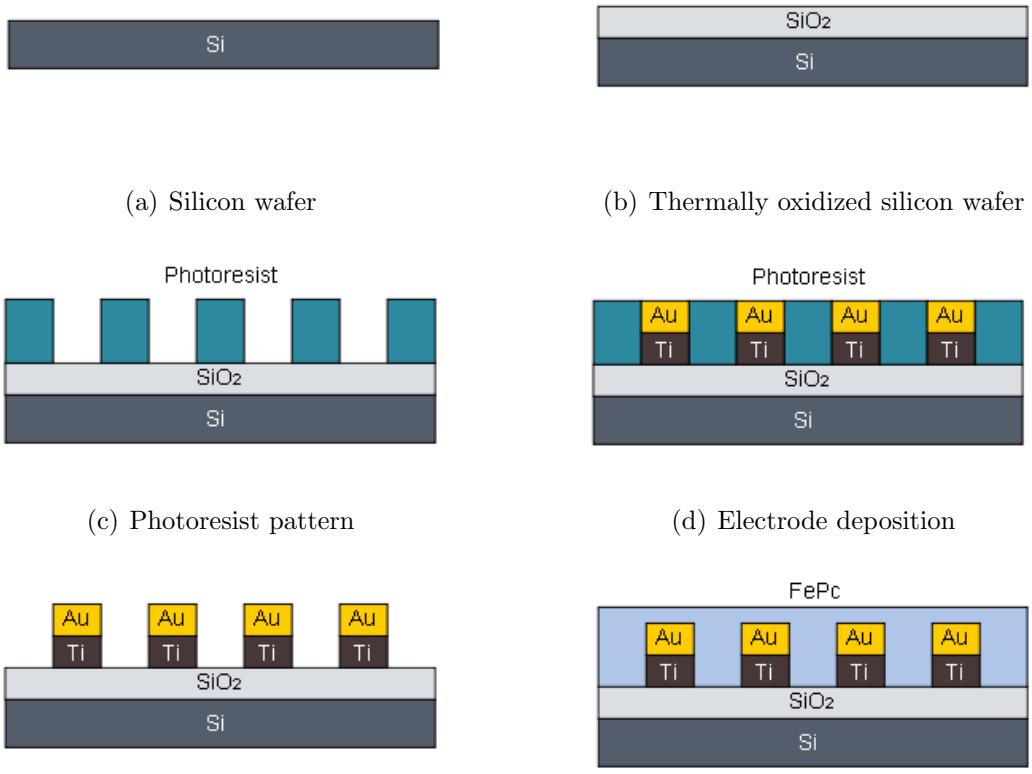

(a) Silicon wafer

(b) Thermally oxidized silicon wafer

(c) Photoresist pattern

(d) Electrode deposition

(e) Photoresist strip

(f) FePc deposition

Figure 4.2: A simple illustration of the microelectronics fabrication process used to produce the FePc thin film sensors used in this research. (a) A silicon wafer is initially cleaned using the RCA procedure in preparation for thermal oxidation. (b) Thermal oxidation is performed in a furnace using a wet process, resulting in a layer of silicon dioxide that acts as a smooth, electrically insulating, and chemically inert substrate. (c) Photoresist is spin coated onto the substrate, exposed to UV radiation through a patterned mask, and unwanted regions are dissolved away with solvent. (d) Electron beam deposition of the interdigitated electrode pattern is performed under a vacuum, with titanium acting as an adhesion layer between silicon dioxide and gold. (e) Remaining photoresist is stripped away with an ultrasonic batch in acetone. (f) Physical vapor deposition is performed to produce a FePc thin film over the interdigitated electrode pattern, completing sensor fabrication.

4.1.1 Substrate

N-type and p-type silicon wafer substrates four inches in diameter and roughly 500 microns in thickness were purchased commercially for use as sensor substrates. The n-type silicon wafers were doped with phosphorous and the p-type silicon wafers were doped with boron. Quartz wafers were also purchased as an additional substrate for fabrication to compare with. The details for each substrate type are listed in Table 4.1.

Table 4.1: Wafer substrate types

	N-type	P-type	Quartz
Material	Si	Si	SiO_2
Diameter	100 mm (4")	100 mm (4")	100 mm (4")
Dopant	Phosphorous	Boron	-
Orientation	100 ($\pm$0.9°)	100 ($\pm$0.9°)	111
Quality	Virgin prime	Virgin prime	-
Thickness	400 $\pm$25 μm	475 $\pm$50 μm	500 $\pm$50 μm
Polish	Single side	Single side	Single side
Resistivity	1-10 Ω-cm	0.03-0.05 Ω-cm	-
SiO_2 Thickness	1000 $\pm$50 nm	1000 $\pm$50 nm	-

4.1.2 Wafer cleaning

Prior to any fabrication procedure, a standard RCA cleaning method was performed on each wafer. The RCA cleaning process was either performed by the wafer suppliers for those wafers that have been purchased in oxidized form, or at AMSTC for those wafers purchased without oxidation. Standard RCA cleaning procedures are designed to remove organic contaminants, while simultaneously producing a thin layer of silicon dioxide, thus preparing the wafer surface for futher oxidation. To perform RCA cleaning, a solution of five parts deionized water, one part ammonium hydroxide (NH_4OH), and one part hydrogen peroxide (H_2O_2) was heated in a large beaker on a boiler plate in a well ventilated area to 55-60 °C, where the solution begins to bubble. The wafers were then immersed into the bubbling solution for 10 minutes, after which they are taken out and placed in a deionized water bath for another 10 minutes. To finish the cleaning process, the wafers were rinsed and dried in a spin-dry washer that rinsed the wafers with deionized water jets and spin-dried the wafers with nitrogen gas. Figure 4.3 is a picture of the spin-dry washer.

Figure 4.3: The spin dry washers at AMSTC rinses wafers with clean deionized water until the wash water has a resistance greater than a threshold value. It then automatically purges the wash chamber with nitrogen gas and spins the wafers until they are dry.

4.1.3 Thermal oxidation

Thermal oxidation on the silicon based wafers was mostly performed by the wafer supplier via a wet process, producing an amorphous layer of SiO_2 one micron in thickness. The oxide thickness of each wafer was independently verified using a laser interferometer at AMSTC. The laser interferometer can measure oxide thicknesses at 64 different locations around the wafer, and automatically compute the standard deviation. Table 4.2 is a list of wafer substrates fabricated for this project, with oxide thicknesses included for reference. Quartz wafers were intended for use as substrates in the as-received condition, and did not require oxidation. Thus no oxide thickness is listed in the table.

Table 4.2: Wafer oxide thickness measured using laser interferometer

Wafer ID	Type	Oxide Thickness Advertised (nm)	Oxide Thickness Measured (nm)	Std. Deviation (%)
1	N	800	750.58	1.776%
2	N	800	750.70	1.799%
3	N	500	495.30	2.850%
4	N	500	489.77	3.388%
5	P	800	747.53	1.782%
6	P	800	752.83	1.371%
7	P	500	489.83	2.838%
8	P	500	486.82	2.941%
9	P	1000 ±1%	1033.50	0.226%
10	N	1000 ±1%	1030.60	0.306%
11	N	1000 ±1%	1030.40	0.373%
12	N	1000 ±1%	1031.40	0.396%
13	N	1000 ±1%	1030.40	0.344%
14	N	1000 ±1%	1029.80	0.495%
15	N	1000 ±1%	977.24	0.748%
16	N	1000 ±1%	969.85	0.588%
17	N	1000 ±1%	992.30	0.515%
18	N	1000 ±1%	986.85	0.667%
19	P	1000 ±1%	1002.00	0.323%
20	P	1000 ±1%	997.55	0.500%
21	P	1000 ±1%	1009.40	0.392%
22	P	1000 ±1%	1006.20	0.448%
23	P	1000 ±1%	1024.40	0.398%
24	P	1000 ±1%	1022.10	0.475%
25	P	1000 ±1%	1030.90	0.468%
26	P	1000 ±1%	1031.10	0.397%
27	P	1000 ±1%	1021.20	0.643%
28	P	1000 ±1%	1025.50	0.546%
29	Quartz	-	-	-
30	Quartz	-	-	-
31	Quartz	-	-	-
32	Quartz	-	-	-
33	Quartz	-	-	-

4.1.4 Photoresist application

The application of photoresist involves a few steps. Initially, wafers were baked in a furnace under an air atmosphere at 120 °C for 20 minutes to kill any organic residue that may contaminate the wafers. Next, the wafers were subjected to vapor deposition treatment of HDMS (Hexamethyl disilazene, $((CH_3)_3Si)_2NH$) at room temperature for 20 minutes. HMDS improves photoresist adhesion to the substrate. After HDMS treatment, AZ5214-E IR photoresist was spin coated onto the wafers at 3000 RPM for 30 seconds, to produce a photoresist film of approximately 1.1-1.3 microns in thickness. AZ5214-E IR is a negative photoresist, where upon UV exposure, the exposed regions undergo a photochemical induced change that results in exposed regions being dissolved away during development. After photoresist has been spin coated onto the wafer, the wafer is soft baked on a hot plate at 110 °C for one minute to evaporate the residual solvent in the film and thus harden the photoresist.

4.1.5 UV exposure patterning

For deposition of the electrodes, a metallic mask encased in glass with 360 sensors arranged within a circular area 100 mm in diameter was designed using CAD software and commercially fabricated. The mask design is presented in Figure 4.4.

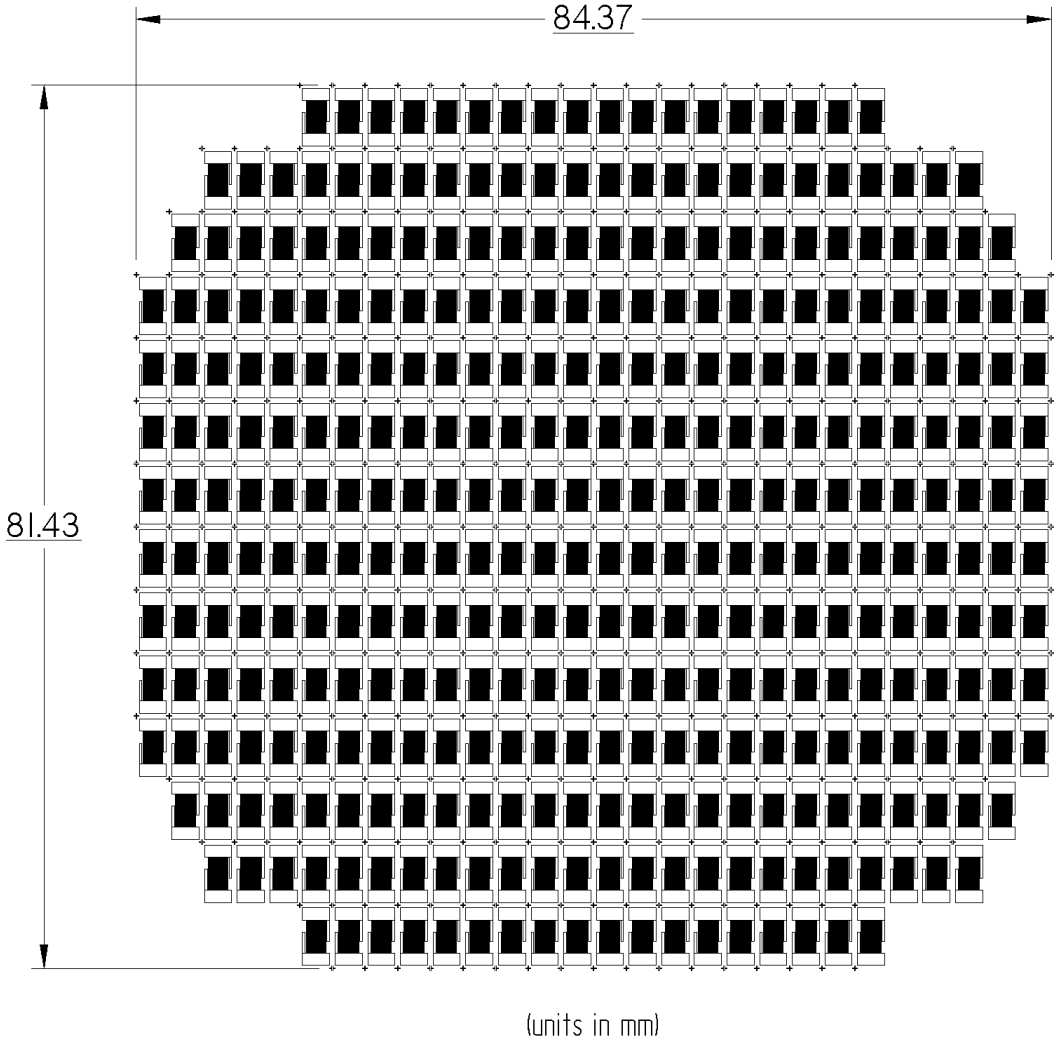

Figure 4.4: The wafer mask design consists of 360 individual sensors arranged in a circular area 100 mm (4") in diameter, intended for transfer onto 100 mm diameter wafers. Crosshair marks indicate the corners for each sensor, and serve as guides for wafer dicing.

This mask was then installed into a Karl Suss BA6/MA6 Mask aligner at AMSTC for UV exposure patterning. Photographs of the mask aligner are shown in Figure 4.5. Each wafer was continuously exposed for 12 seconds at a distance of 30 microns. The wafers were

exposed one at a time to the UV light source set at 300 W. These parameters were optimal in transferring the electrode pattern from the glass mask to the photoresist.

(a)

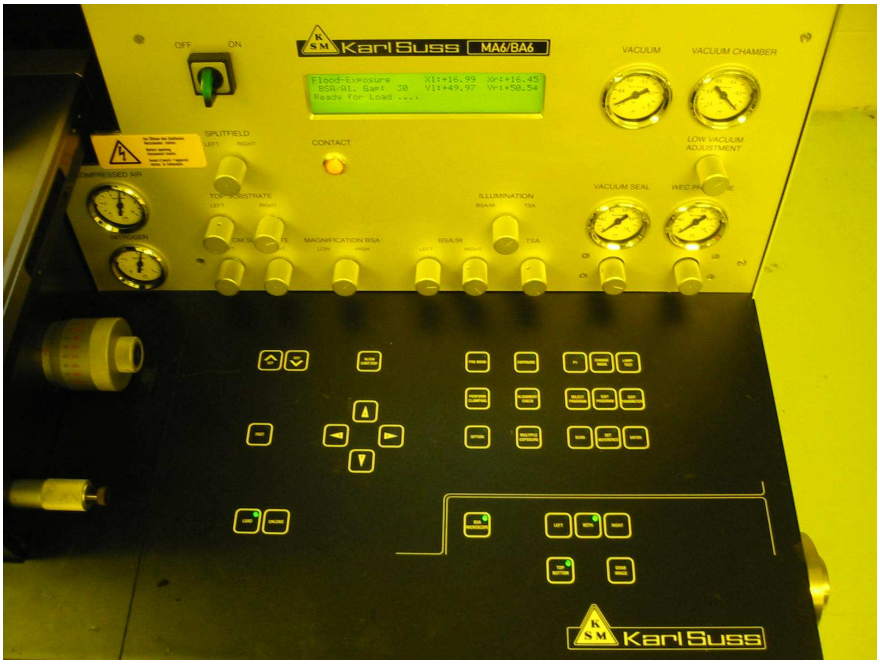

(b)

Figure 4.5: The Karl Suss BA6/MA6 Mask aligner at AMSTC exposes UV radiation through an installed electrode mask onto wafers coated with photoresist. Exposure was set in continuous mode for 12 seconds. The UV lamp power was set at 300 W.

4.1.6 Photoresist development

After pattern transfer onto the photoresist via UV exposure, the photoresist layer for each wafer was developed one wafer at a time in a developer solution consisting of one part AZ400K developer solution and three parts deionized water. The exposure duration was roughly one minute on average, although the exact duration of development varies with how fresh the developer solution is and how long it takes for the electrode pattern to become clearly noticeable via visual inspection. Upon determining that exposure is complete, each wafer is immediately immersed and rinsed in deionized water to arrest the development of photoresist. The wafers are then blow dried with nitrogen and further inspected under an optical microscope to check for major defects in the transferred photoresist pattern.

4.1.7 Electrode deposition

Matrix cleaning, ion cleaning, and electrode deposition were conducted at AMSTC. Matrix cleaning refers to the use of a matrix plasma asher which performs a dry etch to remove residual photoresist that have been developed but remain on the wafer, while ion cleaning refers to a plasma etching process that removes the thin layer of oxide that may have formed during storage and handling. The actual electrode deposition was conducted using a CHA Industries Mark 50 E-beam deposition system. Figures 4.6 and 4.7 show photographs of the machines used for electrode deposition at AMSTC. For 100 mm diameter wafers, this deposition unit has the capacity to perform deposition on 33 wafers in one batch. Thus to ensure sensor fabrication consistency, all 33 wafer substrates reported in this project had their electrode layers e-beam deposited in one batch. During deposition, 50 nm of titanium and 200 nm of gold were deposited in succession, producing a well adhering electrode pattern with total height of 250 nm.

Figure 4.6: The matrix plasma asher at AMSTC is a dry etch device used for stripping of residual photoresist to improve electrode deposition.

(a)

(b)

Figure 4.7: The CHA Industries Mark 50 E-beam Deposition System at AMSTC allowed electrode deposition on 33 wafers of 100 mm (4") diameter in one run. The electrode deposition for each sensor consists of 50 nm of titanium followed by 200 nm of gold.

4.1.8 Lift-off

After e-beam deposition, lift-off of unwanted features was accomplished by immersing the wafers one at a time into an ultrasonic acetone bath for 10 minutes. Removal of unwanted regions is accomplished as acetone dissolves away the photoresist pattern beneath the deposited electrode layer. After the ultrasonic bath in acetone, wafers were individually washed with methanol using a foam brush for 30 seconds, rinsed with deionized water, and finally washed again 10 wafers at a time with a spin dryer. The final electrode structure was inspected using a Tencor profilometer as shown in Figure 4.8. Electrode heights were roughly verified to have an average thickness of 230 nm ($\pm$20 nm across all wafers of the same process), which is slightly less than the 250 nm electrode thickness as intended. This did not pose a significant problem, as long as the electrodes possessed good adhesion to the substrate. To test electrode adhesion, a standard tape test was performed using Kapton tape. No peel off was observed for all wafers, indicating that the electrodes were well adhered to both the silicon dioxide and quartz surfaces.

4.1.9 Wafer dicing

Wafer dicing was performed on a Micro Automation 1100 Dicing Machine with a Kulicke & Soffa dicing blade. Each wafer was diced into 360 individual sensors without indexing or automated cutting; each cut was manually aligned to the crosshairs on the wafer and individually executed. The configuration parameters for wafer dicing are listed in Table 4.3. Figure 4.9 contains photographs showing the dicing machine with the installed blade and to be diced wafer.

4.1.10 FePc deposition

To complete sensor fabrication, a FePc active layer was vapor deposited onto batches of sensors using a Kurt J. Lesker Nano 38 physical vapor deposition system. Prior to placing the diced sensors into the deposition chamber, electrode end pads were masked off with

(a)

(b)

Figure 4.8: The Tencor profilometer runs a sensitive probe accross the surface of the wafer and graphs height versus displacement to generate a surface profile plot. By measuring the electrode height at the center of each of the 33 wafers, the average electrode height was roughly 230 nm in thickness, with a range of ±20 nm.

Table 4.3: Wafer Dicing Parameters

Parameter	Value
Mode	10 (circular wafer)
Dim 1	4000 mils (101.6 mm)
Dim 2	4000 mils (101.6 mm)
Height	5 mils (0.127 mm)
Thickness	40 mils (1.016 mm)
Angle	90 degrees
FWD Cut Speed	75
Spindle Speed	25,000 RPM

(a) Dicing platform

(b) Alignment control panel

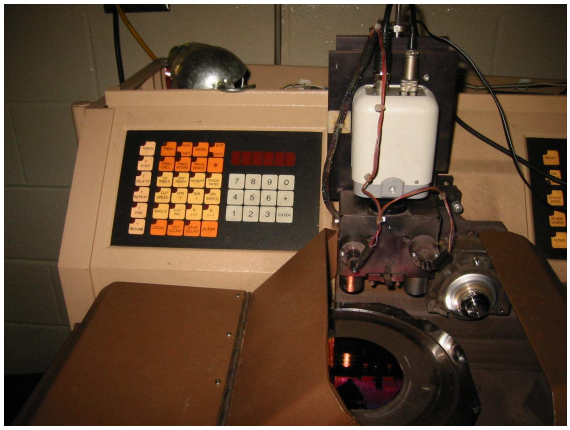

(c) Dicing parameters panel

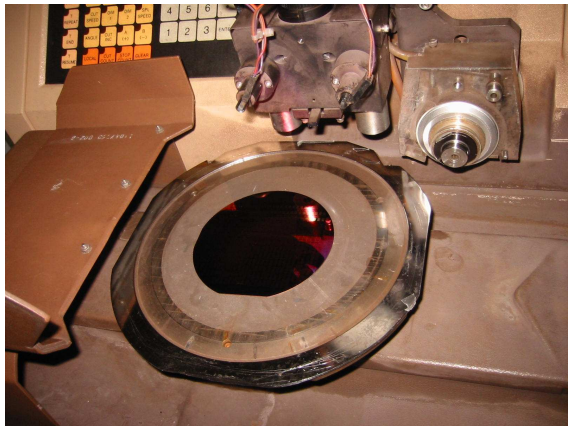

(d) Wafer mounted for dicing

Figure 4.9: The Micro Automation 1100 Dicing Machine was used to dice wafers into individual sensors.

Table 4.4: FePc deposition batches

Batch	Substrate	FePc film thickness (nm)	Average coating rate (nm/s)
A	SiO_2 (N, P) and quartz	50	0.1
B	SiO_2 (N, P) and quartz	100	0.1
C	SiO_2 (N, P) and quartz	150	0.1
D	SiO_2 (N, P) and quartz	200	0.09
E	SiO_2 (N, P) and quartz	250	0.08
F	SiO_2 (N, P) and quartz	300	0.08
G	SiO_2 (N, P) and quartz	350	0.07
H	SiO_2 (N, P) and quartz	450	0.07

kapton tape, while the rest of the sensor was left exposed. Inside the deposition chamber, the substrate was suspended approximately 10 inches from the target. FePc deposition was initiated at a vacuum pressure of $5x10^{-6}$ Torr, at an average rate of 0.1 nm/s, at room temperature. The coating rate and thickness of the FePc thin film deposition process was monitored using a Maxtek TM-400 quartz crystal microbalance thickness monitoring system. Several batches of sensors were coated to produce various FePc film thicknesses. For each batch, all three substrate types (SiO_2 from N-type Si, SiO_2 from P-type Si, and quartz) were used for comparison. The sensor batches and the thicknesses as well as coating rates for each batch are documented in Table 4.4.

The reason that the average coating rates for the thicker batches are slightly lower is because using more FePc powder required all three available evaporation sources to be filled with as much FePc powder as possible, resulting in more time required to switch sources and to get as much powder evaporated as possible in order to reach the intended thickness.

4.2 Gas exposure test setup

Gas exposure tests were performed in a safe and controlled environment to determine sensor response towards nitrogen dioxide gas as well as various other gases of interest. A setup diagram for a typical gas test is shown in Figure 4.10.

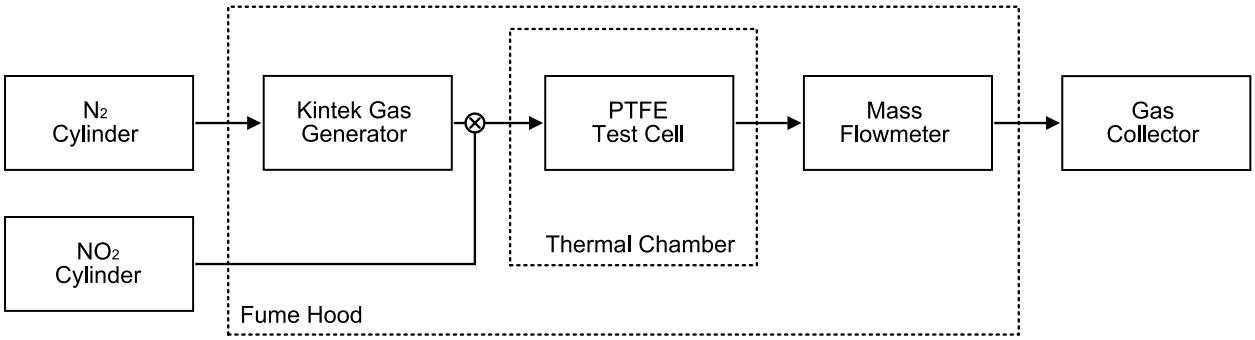

Figure 4.10: Gas test setup diagram. The source gas feed can be toggled between a Kin-Tek gas generator or premixed nitrogen dioxide cylinders. A downstream Omega mass flowmeter monitors the total flow rate of gas. The PTFE test cell is housed within a thermal chamber that controls the test temperature, and the entire test setup other than source gas cylinders is contained within a fume hood.

High purity nitrogen cylinders were commercially obtained from Airgas and provide the source gas for a Kin-Tek gas generator. A gas dryer and filter was installed between the nitrogen source and the gas generator. The generator accepts a liquid permeation source, heats the permeation source to optimal gas emission, and enables gas output of specific concentrations via adjustments on the nitrogen dilution flow rate. For higher concentrations of nitrogen dioxide gas where gas permeation sources are not feasible, premixed gas cylinders were acquired and used directly as the source gas. A chemically stable PTFE test cell holds the sensors in contact with electrical connections. The PTFE test cell is housed inside a thermal chamber, allowing temperature control for the test environment. Flow rate is monitored in real time via an Omega digital mass flowmeter placed downstream of the test cell. The entire test is conducted under a fume hood which collects the out-flowing gas into a collector that stores, filters, and cleans the exhaust gas.

4.2.1 Source gas cylinders

Source gas cylinders used for providing ultra high purity nitrogen gas or other premixed gases were commercially acquired from Airgas. For premixed nitrogen dioxide gas of 100 ppm used in many gas exposure experiments in this research, a certified standard specification provided by Airgas details the precise mixture as 96.42 ppm nitrogen dioxide balanced in 1050 ppm nitrogen with an analytical uncertainty of ± 2 %. Prior to shipment, Airgas verifies the concentrations by direct comparison to calibration standards traceable to NIST ASTM Class 1 weights and NIST gas mixture reference materials. For the ultra high purity grade nitrogen gas used for purging and establishing a sensor baseline throughout this research, Airgas specifies a 99.999 % purity of nitrogen gas, or a maximum of 10 ppm impurity.

4.2.2 Gas generator

For fine adjustment of nitrogen dioxide gas concentrations and flow rates, particularly at low concentrations, a Kin-tek 491MB gas generator was used to produce nitrogen dioxide gas. Gas permeation tubes containing high concentrations of liquid nitrogen dioxide were purchased and placed into the generator. The permeation tubes are calibrated to specific gas emission rates at certain temperatures, thus depending on the trace concentration and flow rates desired, various permeation tubes of different emission rates can be made to order from Kin-tek. The Kin-tek gas generator controls the output trace concentration via adjustments on the diluent gas flow rate. The built-in oven temperature is set at the emission temperature specified on the calibration sheet for each permeation tube. The trace concentration and gas flow rate observe a relationship described in Equation 4.1, where c is the output trace concentration, E is the given emission rate of the permeation tube, K_o is the mass rate to volume rate conversion constant, and r is the dilution gas flow rate.

$$c = \frac{E * K_o}{1000 * r} \tag{4.1}$$

Nitrogen dioxide concentrations at or near 1 ppm is of particular interest for this project becuse it has been set forth as a exposure limit above which significant health risk can occur. To generate nitrogen dioxide concentrations at or near 1ppm, a permeation tube with an emission rate of 987 ng/min at 30 °C and mass rate to volume rate conversion of 0.487 was purchased from Kin-tek. Table 4.5 documents the dilution flow rates that should be set to obtain certain trace nitrogen dioxide concentrations using this permeation tube. Notice that the actual flow rate is always 0.1 L/min greater than the dilution flow rate set on the Kin-tek generator, because by design, 0.1 L/min of diluent gas is used to bring gas out from the emission chamber.

Table 4.5: Dilution flow rate for target nitrogen dioxide concentrations

Concentration (ppm)	Dilution flow rate (L/min)	Actual flow rate(L/min)
0.25	1.923	2.023
0.50	0.961	1.061
0.75	0.641	0.741
1.00	0.481	0.581
1.25	0.385	0.485
1.50	0.320	0.420
1.75	0.275	0.375
2.00	0.240	0.340

4.2.3 Thermal chambers

Several thermal chambers were used to provide the temperature conditions necessary for sensor experiments. An Espec ECT temperature chamber, shown in Figure 4.11(a), housed long term temperature cycling experiments due to it having a built in refrigeration unit capable of -70 °C. The maximum temperature for this chamber is 200 °C. For experiments involving non-inert gases, a smaller Despatch 900 temperature chamber shown in Figure 4.11(b) is capable of fitting inside a standard fume hood and was thus used to regulate temperatures for nitrogen dioxide and other gas exposure experiments. This unit requires the use of an external liquid nitrogen source for cooling. Both thermal chambers are programmable and can run temperature profiles unattended. A hole on the left side of each chamber acts as a feedthrough port for gas tubes, electrical wires, and thermocouples to enter and exit each chamber.

4.2.4 Test cell

Test cells were constructed to house multiple sensors and contain them for gas exposure tests. The material of choice for test cell construction was Teflon PFA (Perfluoroalkoxy copolymer resin) or PTFE (polytetrafluoroethylene), due to its inert chemical properties and excellent thermal stability. The test cells also prevent visible light or UV radiation from entering the cell, to prevent the effects of photoconduction on FePc thin films. All the materials inside the test cells, including fittings, tubings, and wire coatings were made of Teflon PFA or PTFE, with the exception of a small amount of gold electrode contacts, stainless steel fixtures, and electrical connectors. The four sensor test cell is shown in Figure 4.12. The Teflon PFA and PTFE housing of the test cell were constructed of blow molded surfaces to ensure minimal adsorption when exposed to trace levels of nitrogen dioxide gas. Furthermore, the electrical clip, electrical connector, thermocouple, and wires are all situated downstream of the sensor position, removing the possibility of any interference on gas sensing.

(a) Espec ECT temperature chamber

(b) Despatch 900 temperature chamber

Figure 4.11: (a) The Espec ECT temperature chamber is used mainly for temperature cycles and inert gas exposure tests. Its built in refrigeration unit is capable of maintaining a low temperature of -70 °C, while its high temperature is 200 °C. (b) The Despatch 900 temperature chamber is smaller, and only has a built in heater while relying on an external liquid nitrogen source for cooling. Since it fits under a normal fume hood, its primary use is for regulating temperatures for gas exposure experiments involving hazardous gases.

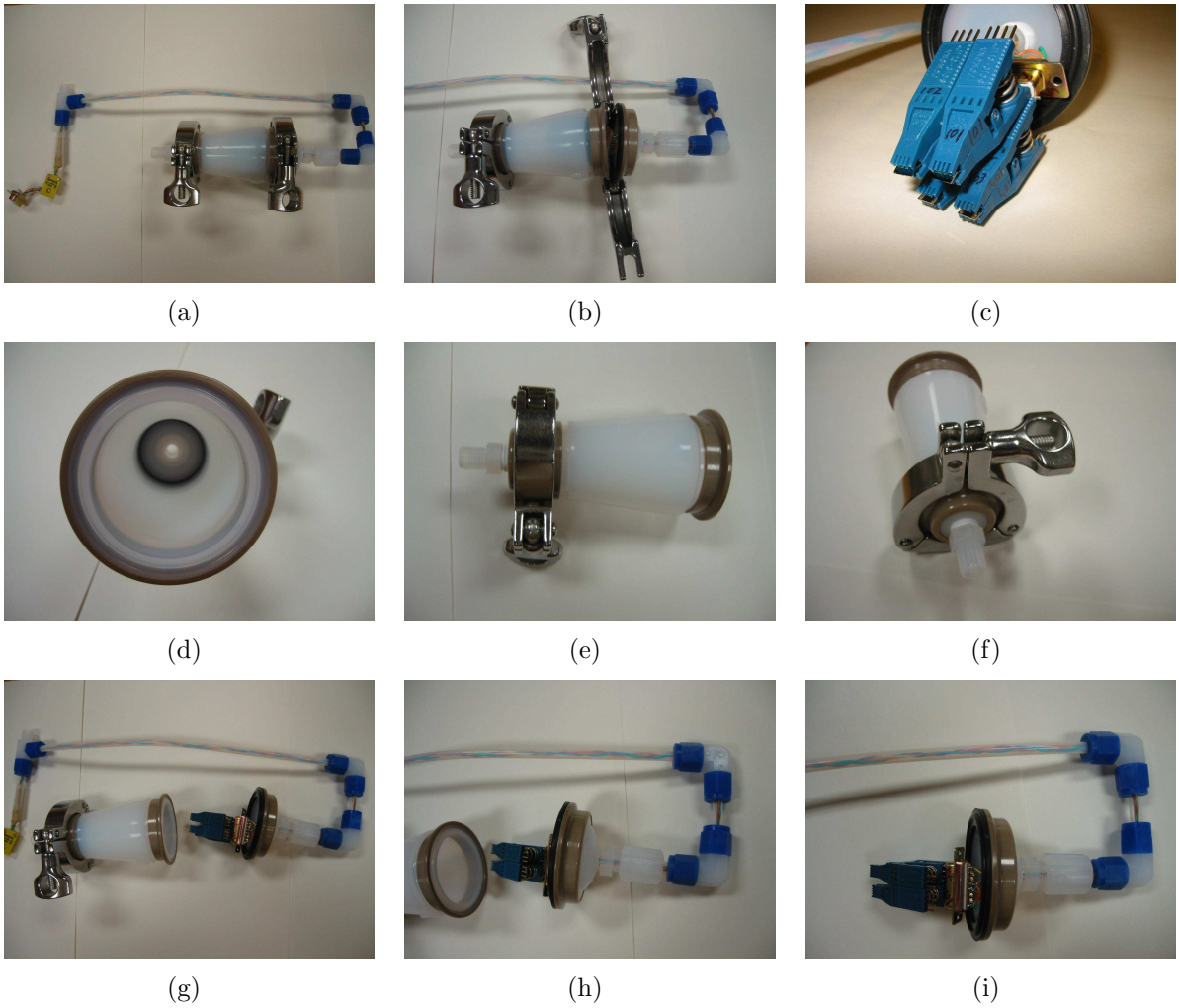

Figure 4.12: The four sensor test cell houses four sensors parallel to the flow. The chamber is a circular tube of expanding radius. Electrical test clips have been adapted to hold the sensors via its front contacts. The back contacts of the test clips are then inserted into a DB15 female connector. PTFE coated lead wires are fed out out of the test cell along with outflowing gas. A T-junction with one end sealed separates the lead wires, which are connected to the data acquisition system, from the outflowing gas, which is fed through the exhaust channels of the fume hood. Since most of the fixture components are downstream of the sensor positions, contamination due to component outgassing is minimized.

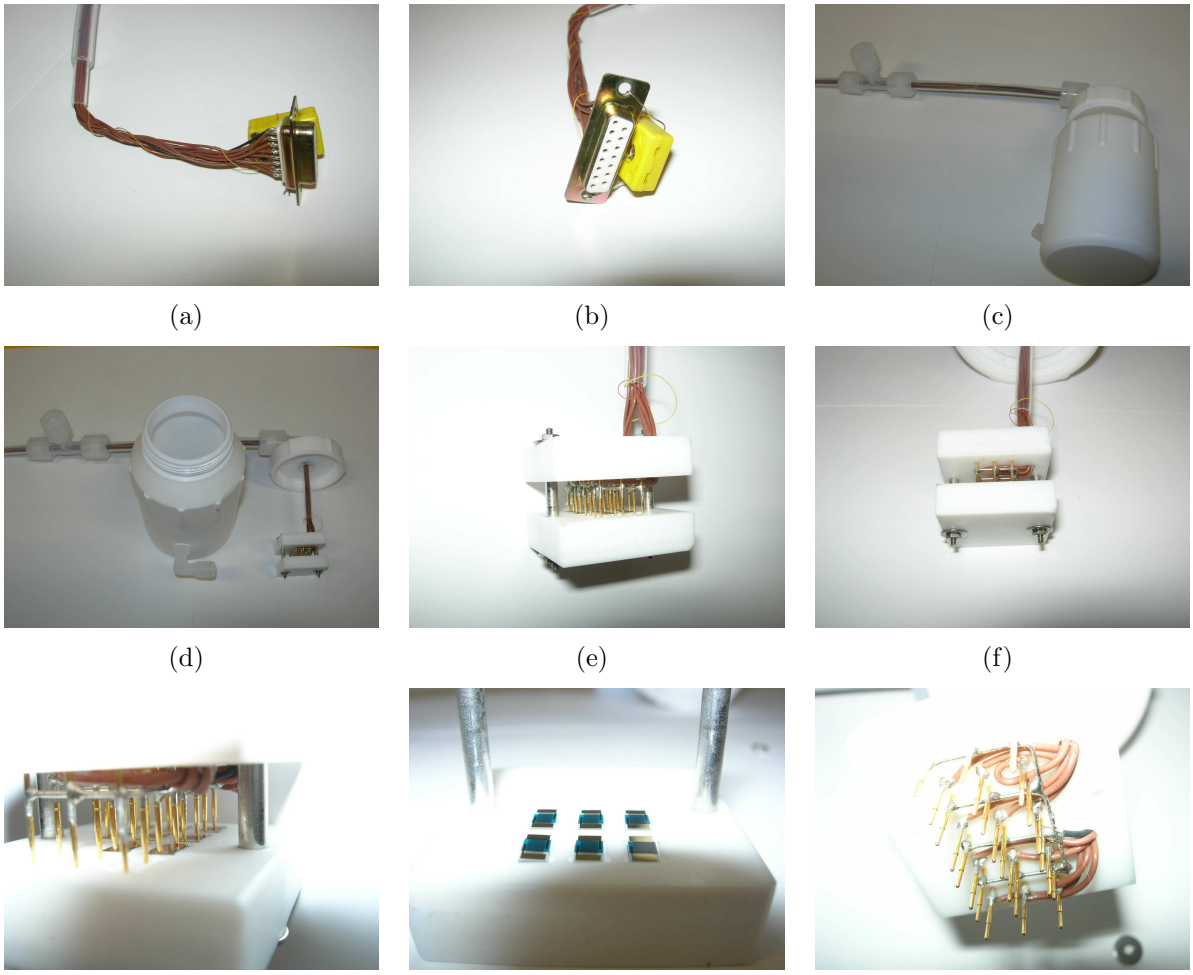

Figure 4.13: The twelve sensor test cell mainly consists of a PTFE fixture housed within a PTFE bottle. Two holes have been drilled into bottle, one on the top cap and one on the side. Gas flows into the cell from the side hole and out through the top hole, along with PTFE coated wires that carry the electrical output from the sensors. The PTFE fixture consists of a base that holds sensors and a top that holds electrode pins. The base contains 12 rectangular indentations about quarter of a millimeter deep to hold the 12 sensors. The top contains 24 small holes inserted with spring-loaded pogo pins that come into contact with sensor electrode pads when the top and bottom of the fixture is put together. The fixture is held together via two stainless steel screws. PTFE coated wires were soldered onto the pogo pins and led out through the outflowing 3/8" PFA tube fitting. In comparison, gas flows into the cell through a 1/4" PFA tube. A k-type thermalcouple is positioned on top of the test fixture inside the bottle. The total volume of the PTFE bottle is 240 mL.

4.2.5 Data acquisition setup

Data acquisition for the FePc based nitrogen dioxide sensor consists primarily of monitoring the resistance across each sensor's two electrodes. In addition to holding sensors in place, the test cells provide electrical contact with each sensor's electrodes. The lead wires from the test cell are then connected to a data acquisition system. Figure 4.14 depicts the electrical wiring diagram for data acquisition. Each sensor in the test cell is monitored almost simultaneously this setup. The data acquisition system consists of an Agilent 34970 data acquisition switch connected to a Windows PC running Agilent Benchlink software. The Agilent 34970 data acquisition switch has a 20 channel multiplexer module installed. Any of the 20 channels can be configured to detect AC/DC voltage, 2/4-wire resistance, current, or temperature (via a thermocouple).

Due to the high initial resistances of FePc films, thick film high stability 10 MΩ resistors were placed in parallel to each sensor, effectively scaling the sensor resistance to within a desirable measurement range of the Agilent data acquisition switch; the measured resistance is thus capped at 10 MΩ, and the true resistance value of each sensor is determined using equivalent resistance calculations. The primary reason for this configuration is to prevent the Agilent switch from applying a voltage greater than 1 V for the measurement of resistance, which may overheat and damage the FePc thin film.

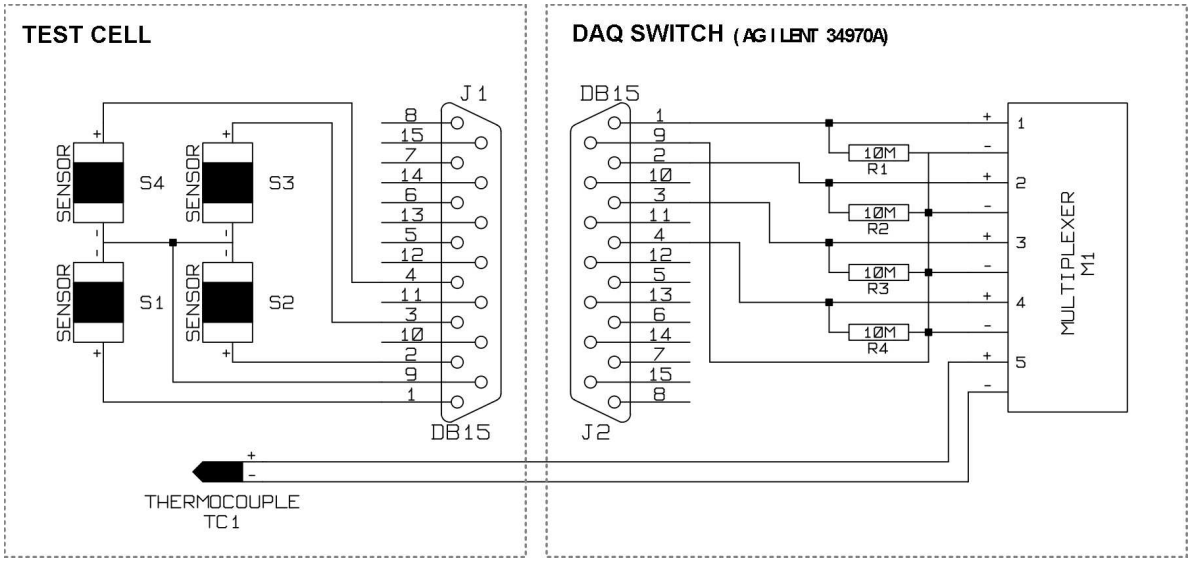

Figure 4.14: An electrical layout diagram for the data acquisition setup depicts four sensors housed in a PTFE test cell, sharing a common ground. PTFE coated wires connected to the sensors are fed to a DB15 connector at the test cell wall. A shielded DB15 cable connects the test cell to an Agilent 34970A data acquisition switch. A 20 channel onboard multiplexer can monitor up to 20 channels of resistance, voltage, current, or temperature via the use of thermocouples. Parallel resistors with stable 10 MOhm resistance are placed in parallel to the sensors for each channel. A k-type thermocouple placed inside the test cell monitors the temperature in close vicinity of the sensors. The measured resistances and temperatures are captured and stored on a PC running Agilent Benchlink software.

Chapter 5

Results and Discussion

5.1 Sensor fabrication results

The sensor substrates used for experiments were fabricated in the AMSTC clean room at Auburn University. In total, 32 wafers were fabricated with electrodes based on the sensor design and fabrication procedures detailed in the previous two chapters. Although these wafers consisted of n-type, p-type, and quartz substrates, all wafers were processed in one batch, and can be considered to share identical electrode dimensions. This reduces production cost, while also ensuring sensor electrode consistency, thereby enabling reliable comparison of substrate type, film thickness, and sensor response results.

After electrode deposition, the FePc thin film active layer was vacuum sublimed using a Kurt J. Lesker Nano 38 physical vapor deposition system. Deposition of each film thickness was conducted under room temperature at 5 x 10−6 Torr. Figure 5.1 shows photographs of eight vacuum sublimed batches of sensors, with film thickness ranging from 50 nm to 450 nm, as monitored during deposition with a QCM thickness monitor and verified via profilometry. Within each FePc deposition batch, p-type oxidized silicon, n-type oxidized silicon, and quartz substrates were used.

To evaluate the uniformity of FePc film thickness, a Tencor profilometer was used to measure thickness on a batch of vacuum sublimed FePc sensors. For this batch, the vacuum sublimation process was stopped when the QCM thickness sensor inside the physical vapor deposition system reached 450 nm. Figure 5.2 shows the results of the Tencor profilometer thickness measurements. These measurements were taken across the diameter of the wafer on four different axes. The results show a ± 16 nm difference between the average thickness measured via profilometry compared to the QCM thickness measurement. As expected,

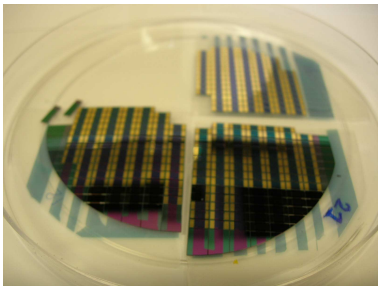

(a) 50 nm FePc

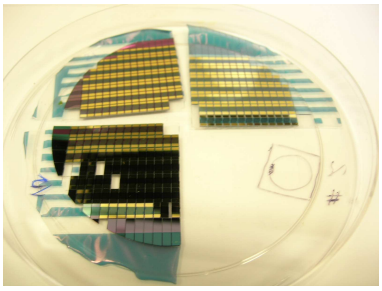

(b) 100 nm FePc

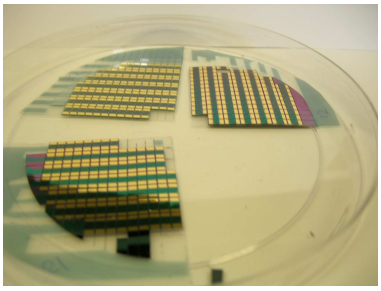

(c) 150 nm FePc

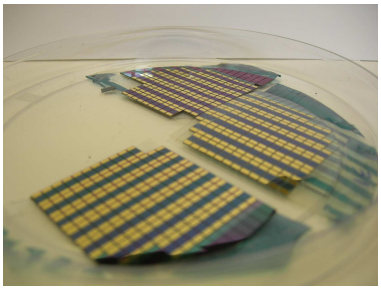

(d) 200 nm FePc

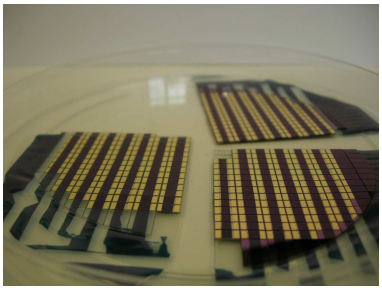

(e) 250 nm FePc

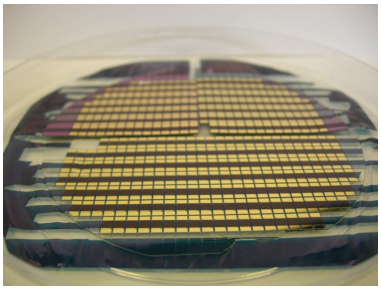

(f) 300 nm FePc

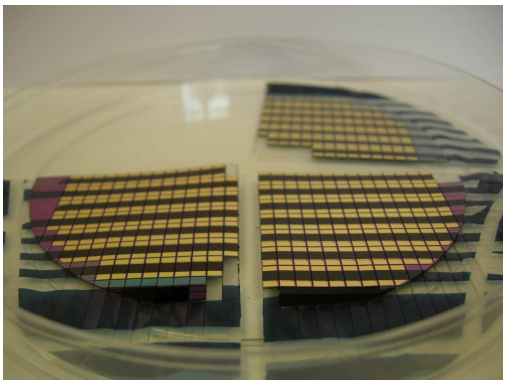

(g) 350 nm FePc

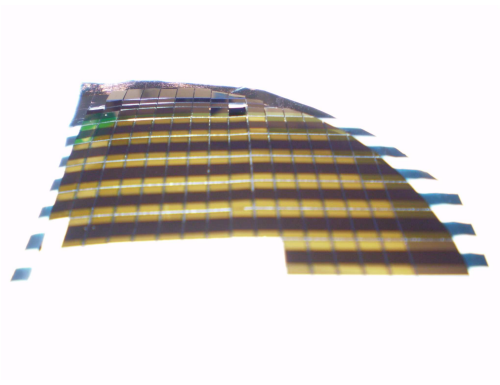

(h) 450 nm FePc

Figure 5.1: Physical vapor deposition of FePc thins was performed for six different thicknesses: (a) 50 nm, (b) 100 nm, (c) 150 nm, (d) 200 nm, (e) 250 nm, (f) 300 nm, (g) 350 nm, and (h) 450 nm. The thickness of each FePc film was monitored using a QCM thickness monitor and verified with a profilometer. The sensor electrode region for contact with measurement probes were masked off with Kapton tape during deposition and removed after.

film thickness closer to the edge of the wafer is thinner than at the center. Profilometer measurements indicate that this thickness reduction may reach up to 50 nm.

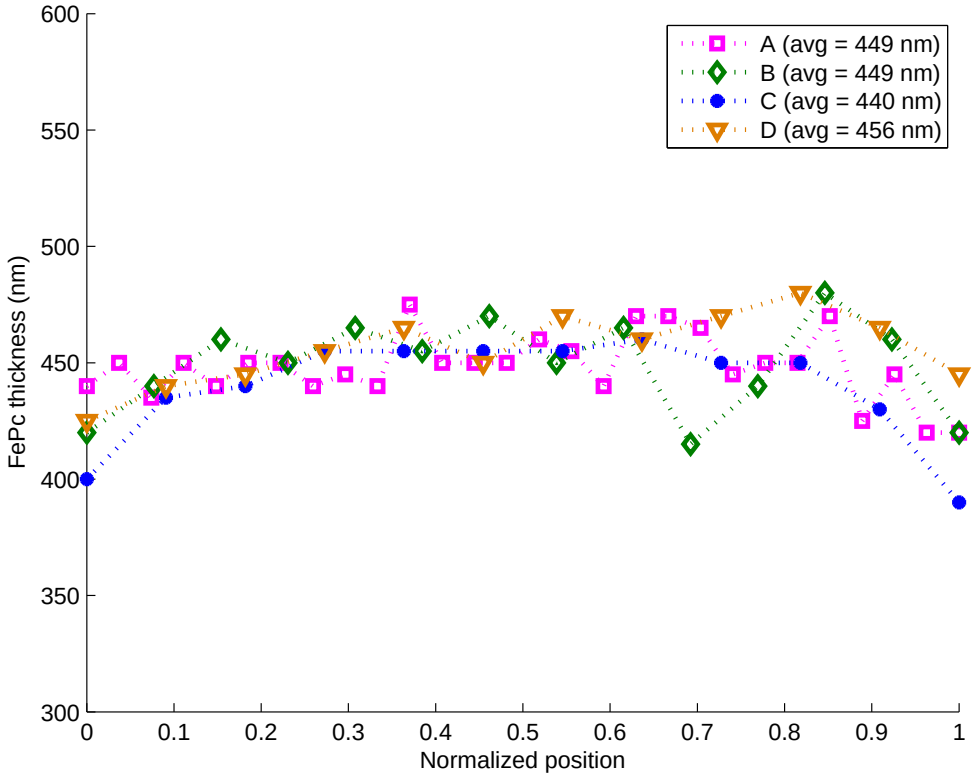

Figure 5.2: Tencor profilometer thickness measurements were taken across the diameter of the wafer on four different axes. The results show a ± 16 nm difference between the average thickness measured via profilometry compared to the QCM thickness measurement. As expected, film thickness closer to the edge of the wafer is thinner than at the center. Profilometer measurements indicate that this thickness reduction may reach up to 50 nm.

5.2 Characterization of response

Fundamentally, FePc thin films experience increased conductivity in the presence of nitrogen dioxide gas. The principle behind its conductivity change is that nitrogen dioxide molecules adsorb onto the surface of FePc thin films and effectively dope the film, creating hole charge carriers and making the film essentially a p-type semiconductor. Like typical semiconductor materials, FePc experiences significant temperature dependencies that affect detection. It is adopted from military specifications that a maximal diurnal temperature range of -46 °C to 71 °C represents the extremes in operating temperatures for a field sensor. To investigate the sensor's general performance over this range, sensors were exposed to 100 ppm nitrogen dioxide gas inside a temperature chamber set at -46, 20, and 71 °C. Such a high concentration of nitrogen dioxide can allow the determination of saturation durations as well as saturation resistance levels at each temperature. To further investigate temperature dependence, sensors were exposed to temperature cycles ranging from -50 to 80 °C under nitrogen gas and then under 100 ppm nitrogen dioxide gas. The results can be used to establish a resistance boundary for this temperature range and also to produce an Arrhenius plot. The Arrhenius plot can be used to estimate activation energies for this specific FePc film under saturated (extrinsic) and unsaturated (intrinsic) conditions. Since several government and international health agencies have identified the concentration of 1 ppm nitrogen dioxide to be the permissible limit, passive sensing response at or near 1 ppm is of importance. To investigate sensor concentration dependence to nitrogen dioxide in the range of 1 ppm, and to determine the feasibility of passive sensing, sensors were exposed to 0.5, 1, and 2 ppm nitrogen dioxide gas at room temperature. Finally, to investigate repeatability of sensor response to the target nitrogen dioxide concentration of 1 ppm, sensors were repeatedly exposed to 1 ppm nitrogen dioxide in between nitrogen flush cycles. The results of these experiments are presented in the following subsections.

5.2.1 Introduction to sensor response

The FePc thin film sensor is operated by detecting changes in electrical conductivity accross a FePc film as it is exposed to an analyte gas. In the presence of highly oxidizing gases such as nitrogen dioxide, the gas molecules react with FePc molecules and adsorb onto the surface of FePc thin films. Each reaction results in a charge carrier complex that liberates hole charge carriers in the FePc bulk, thereby significantly increasing the FePc thin film conductivity when an electric field is applied. The change in film conductivity can be monitored via periodic resistance measurements across the electrode pads on the sensor. Figure 5.3 shows photos of the FePc thin film sensor prepared for testing.

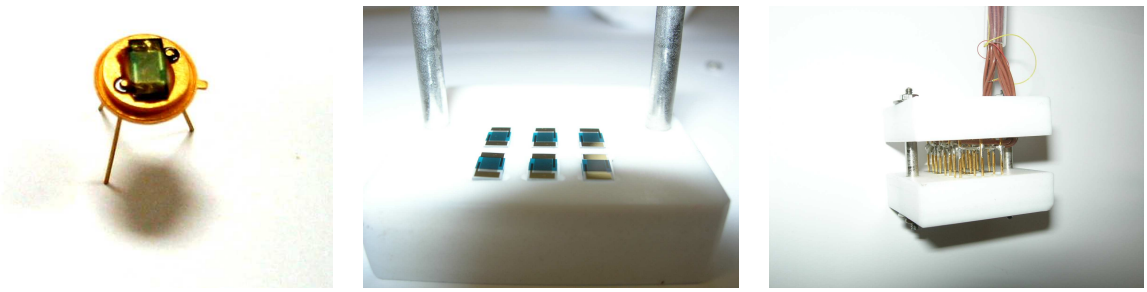

(a) Mounted sensor (b) Six quartz sensors (c) Sensors in test cell

Figure 5.3: (a) For field operation, a sensor is packaged on a common transistor outline header, with its gold contacts wire bonded to corresponding contact points on the header. (b) For experimental purposes, many sensors need to be tested together; shown here are six sensors based on quartz substrates ready for testing. (c) A PTFE test cell was constructed to hold multiple sensors for simultaneous testing.

Once resistance measurements across underlying electrodes are recorded, its change over time can be analyzed to determine analyte gas concentration. A typical resistance vs. time plot of a sensor exposed to 100 ppm nitrogen dioxide gas is presented in Figure 5.4. In this basic gas exposure experiment, the FePc thin film sensor was initially stabilized in ultra high purity nitrogen gas for 30 minutes, then exposed to 100 ppm concentration nitrogen dioxide gas for 30 minutes, and finally allowed to recover under nitrogen gas for another 30 minutes, all at a constant flow rate of 0.25 L/min. FePc thin films are known to be non-interacting

with the inert nitrogen gas, therefore the purpose of the initial 30 minute nitrogen exposure is to establish a stable baseline. When nitrogen dioxide gas is introduced, since its content consists of nitrogen dioxide diluted in nitrogen gas, any changes in the sensor thin film can be attributed to the presence of nitrogen dioxide. From the resistance plot, the presence of nitrogen dioxide decreased film resistance from 8.2 x 10^7 Ω to 5.2 x 10^4 Ω in a nonlinear trend. In this example, sensor saturation was not achieved in one hour, because resistance continues to decrease after one hour of exposure. The reason may be due to greater film thickness or rougher surface morphology, which will require longer timeframes for nitrogen dioxide molecules to reach all the adsorption sites. After nitrogen dioxide exposure, the sensor is allowed to recover under nitrogen gas, to investigate its recovery characteristics. Typically, at room temperature or lower, the recovery characteristics of FePc thin films is less than ideal, with sensors recovering to only a fraction of its initial resistance. In previous MPc thin film sensor research, reversibility can be improved with increased operating temperature, β phase crystal structures, and thinner films. However, in this research, a non-reversible FePc thin film is fabricated for passive detection. In the latter parts of this chapter, results are presented for experiments designed to investigate the performance of a FePc thin film passive sensor.

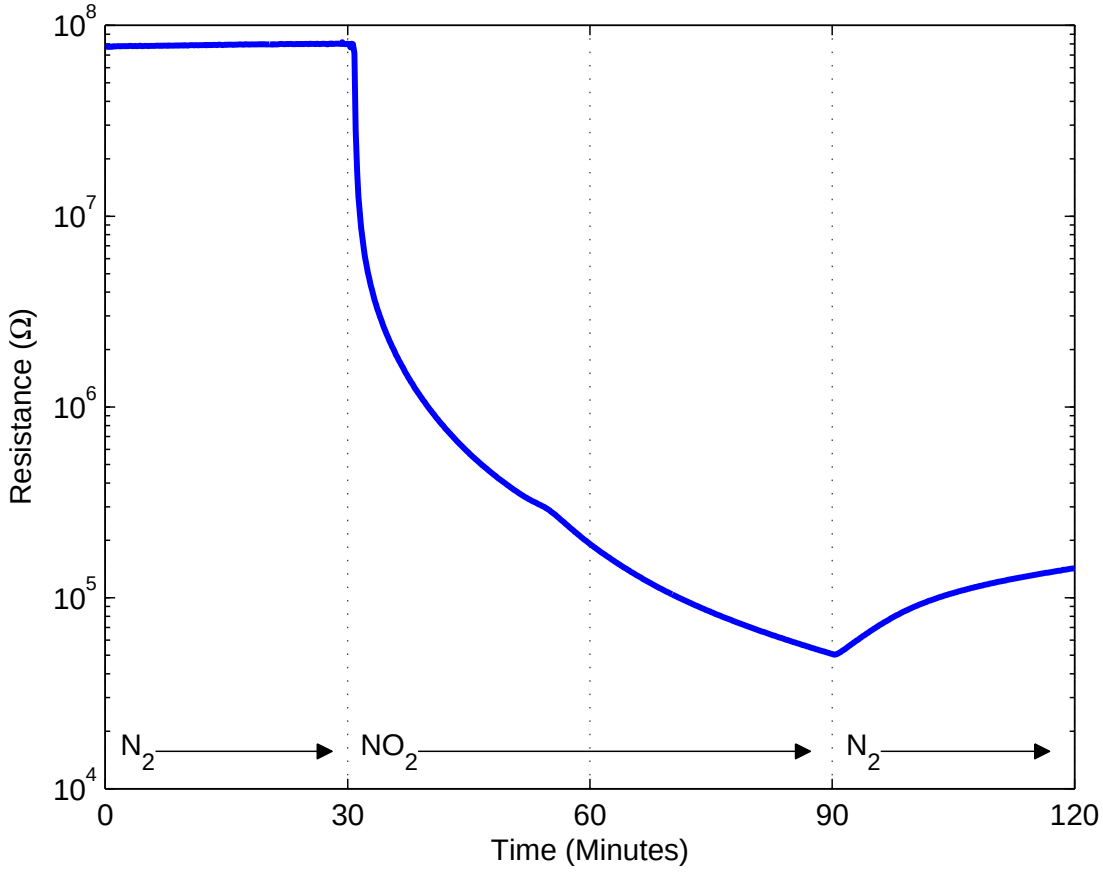

Figure 5.4: Typical FePc thin film sensor response to nitrogen dioxide. The nitrogen dioxide concentration was 100 ppm and the gas exposure test was performed at 20 °C. The gas flow rate was maintained at a constant 0.25 L/min. In this standard gas exposure experiment, the sensor was initially allowed to stabilize under ultra high purity nitrogen gas for 30 minutes, then exposed to nitrogen dioxide for one hour, and finally allowed to recover under nitrogen gas for another 30 minutes.

5.2.2 General sensor response

To determine general response at different temperatures, sensors were exposed to 100 ppm concentration nitrogen dioxide gas at a constant flow rate of 0.25 L/min under three different temperatures of -46 °C, 20 °C, and 71 °C. The change in resistance over time is plotted in Figure 5.5. All three sensors were heat treated in air at 130 °C for a total duration of two hours prior to nitrogen dioxide exposure. This anneal step was performed as a precaution to avoid potential structural changes in the FePc film during operation, for elevated temperatures can induce morphological changes in the film. For each test, the sensors were stabilized in nitrogen for 10 minutes before 100 ppm nitrogen dioxide gas is introduced into the test cell. The gas flow rates were held at a constant 0.25 L/min throughout each experiment. All three exposure tests were run for 30 minutes until sensor saturation was achieved.

At 20 °C, the sensor showed a decrease in resistance from 1.3×10^8 to $1.8 \times 10^5 \Omega$. At 71 °C, the sensor showed a decrease in resistance from 9.6×10^6 to $1.5 \times 10^5 \Omega$. At -46 °C, the sensor showed a decrease in resistance from 5.4×10^8 to $2.3 \times 10^5 \Omega$. The differences in initial resistances of the sensors can be attributed to the different operating temperatures that affect the mobility of hole carriers within FePc thin films. The similarities in the saturation resistances reveals that the nitrogen dioxide doping mechanism on FePc thin films is relatively unaffected by the ambient temperature. These results indicate that at least two orders of magnitude change in resistance can be expected for nitrogen dioxide saturated sensors operating within the temperature range of -46 °C and 71 °C, and that total saturation time does not exceed 30 minutes for 100 ppm nitrogen dioxide gas at 0.25 L/min.

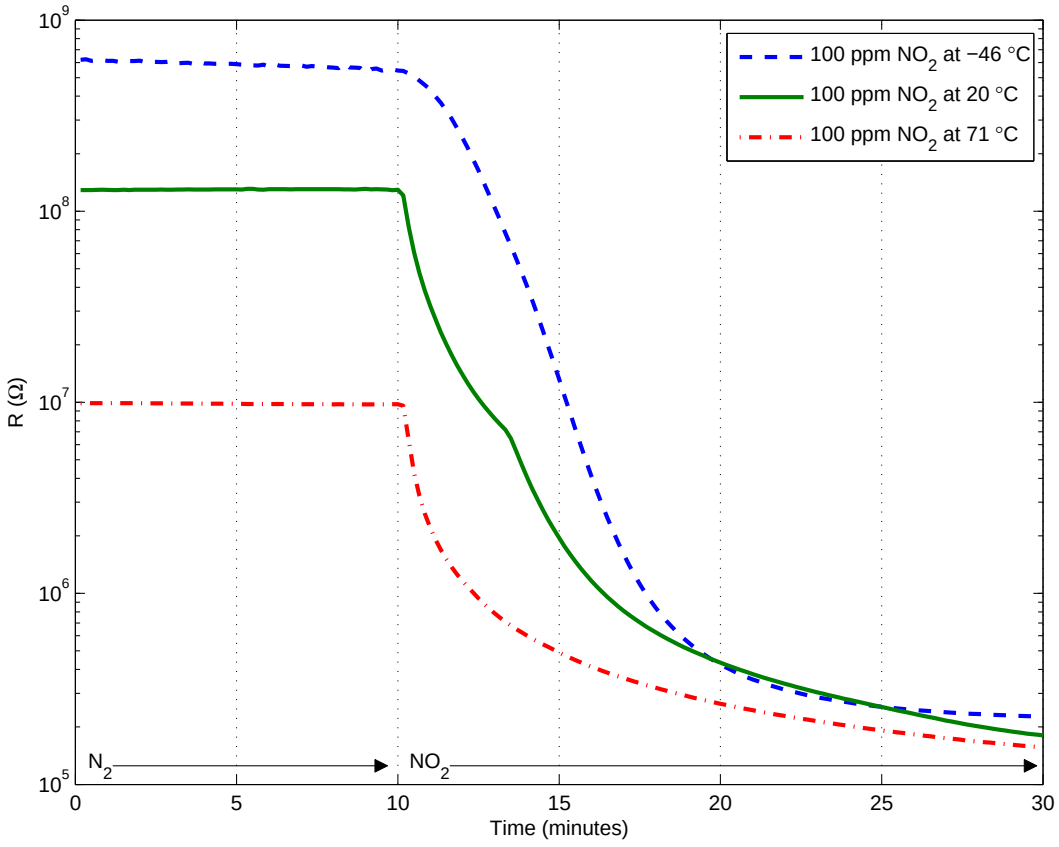

Figure 5.5: Response of sensors to 30 minutes of 100 ppm nitrogen dioxide at -46, 20, and 71 °C.

5.2.3 Temperature dependence

Similar to typical semiconductors, the conductivity of FePc thin films increases with an increase in temperature. As mentioned before, the conductivity of FePc thin films originates primarily from a reaction with electron accepting oxidizing gases, which creates a charge transfer complex and liberates hole charge carriers into the bulk. The role of temperature is such that it affects the reaction rate and equilibrium of this doping reaction. An increase in temperature leads to increased reaction rates between oxidizing gases and FePc thin films, creating more hole charge carriers, and thereby increasing film conductivity.

To investigate the magnitude of temperature dependence, film resistance levels on a 450 nm sensor were monitored every 15 seconds as temperature was varied from 71 to -46 °C at a rate of 2 °C per minute. Prior to taking data, the sensor was allowed to stabilize under ultra high purity nitrogen gas for one day. For the first thermal cycle, the nitrogen gas flow rate was maintained at 0.1 L/min. Film conduction under nitrogen gas can reveal the intrinsic, non-doped conductivity of FePc thin films as nitrogen gas is considered to be non-interacting. To also investigate the temperature dependence of extrinsic, doped conductivity, the sensor was then exposed to 100 ppm nitrogen dioxide gas for one hour at 71 °C. After sensor saturation was achieved, a second thermal cycle was conducted under 100 ppm nitrogen dioxide gas at a constant flow rate of 0.1 L/min. Figure 5.6 shows the resistance response of the sensor under both thermal cycles. In the figure, the resistance response curve for the sensor under nitrogen gas represents changes in the intrinsic conductivity, while the response curve under nitrogen dioxide gas represents changes in the extrinsic conductivity of the FePc film. For the intrinsic curve, it is observed that temperature dependence remains significant, possibly due to inadequate desorption of adsorbed oxygen, or that trace quantities of dopant gases reside in the ultra high purity nitrogen gas. Thus the intrinsic result may not represent true intrinsic film conduction. However, as expected, the resistance levels for extrinsic conduction under nitrogen dioxide gas are much lower compared to the resistance levels for intrinsic conduction as observed under nitrogen gas. These two curves reveal the maximum resistance change

at any operating temperature between -46 to 71 °C for a 450 nm FePc thin film sensor exposed to nitrogen dioxide gas. The region between the two curves can be also assumed to be the operating resistance regime of this FePc thin film sensor. Approximately 5 orders of magnitude change occurs at -46 °C, compared to 3 orders of magnitude change at 71 °C, indicating that the sensor experiences a larger conductivity change at lower temperatures.

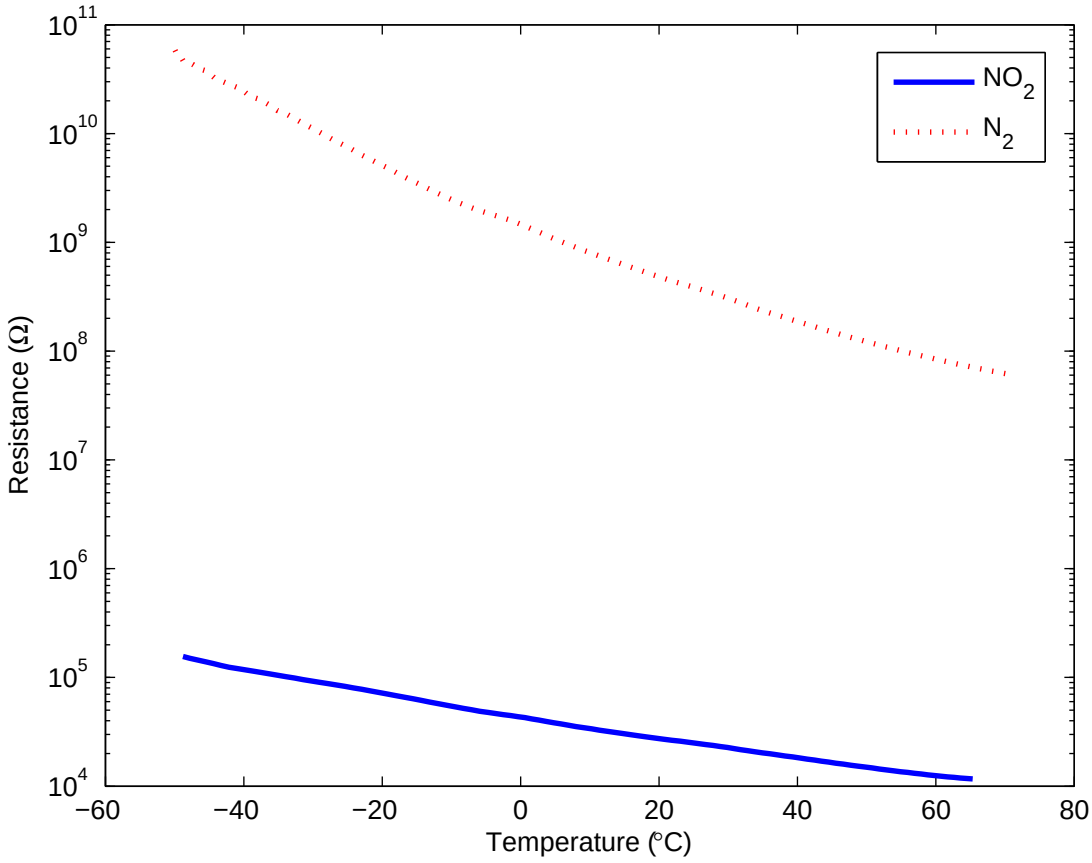

Figure 5.6: Resistance trends of a 450 nm FePc thin film sensor shows decreasing resistance as temperature increases from -46 to 71 °C. The dotted line shows intrinsic resistance levels as the sensor is subjected to flowing nitrogen gas at 0.1 L/min, while the solid line shows extrinsic resistance levels as the sensor is exposed to 100 ppm nitrogen dioxide gas at 0.1 L/min. Although the intrinsic case may involve trace levels of oxygen or other forms of atmospheric doping, these trends indicate that nitrogen dioxide saturation of the FePc thin film can still cause 3-5 orders of magnitude change within this temperature range, with greater resistance changes occurring at lower temperatures.

Since the reaction between oxidizing gas species and FePc thin films forms the mechanism behind FePc thin film conductivity, it can be assumed that film conductivity is directly proportional to the reaction rate. With this assumption, a model for temperature dependence of conductivity can be derived from the Arrhenius equation, which describes reaction rates in terms of temperature. A modified form of the Arrhenius equation relating conductivity to temperature for FePc thin films is presented in Equation 5.1.

$$\sigma \propto exp(\frac{-E_a}{2kT}) \tag{5.1}$$

In this equation, σ is the FePc film conductivity, E_a is the activation energy for charge carrier formation, k is Boltzmann's constant (8.614 eVK^{-1}), and T is the temperature. Physically, the activation energy term in this model includes all the energy steps required for charge carrier formation. This includes the energies for gas adsorption, charge transfer, and delocalization of charge carriers in the FePc thin film. Using the resistance data as a function of temperature presented in Figure 5.6, an Arrhenius plot with $ln(\sigma)$ versus $1/T$ was constructed to determine whether the temperature dependence of FePc thin films fits the Arrhenius conductivity model. But first, the resistance values from the thermal cycling experiment under nitrogen and nitrogen dioxide gas need to be converted to conductivity by considering sensor geometry and film thickness. Equation 5.2 details this conversion.

$$\sigma_b = \frac{d}{R}\left[\frac{1}{(2n-1)lh + 2neh}\right] \tag{5.2}$$

In this equation, d is the electrode gap spacing (15 x 10^{-6} m), R is the measured resistance, n is the total number of electrode fingers (25), l is the length of electrode fingers (2.97 x 10^{-3} m), h is the film thickness (450 x 10^{-9} m), and e is the width of electrode fingers (22 x 10^{-6} m). With conductivity determined, an Arrhenius plot with $ln(\sigma)$ versus $1/T$ for both intrinsic conduction under nitrogen and extrinsic conduction under nitrogen dioxide is

presented in Figure 5.7. Curve fitting results are also presented in the figure, based on the Arrhenius conductivity model in Equation 5.1.

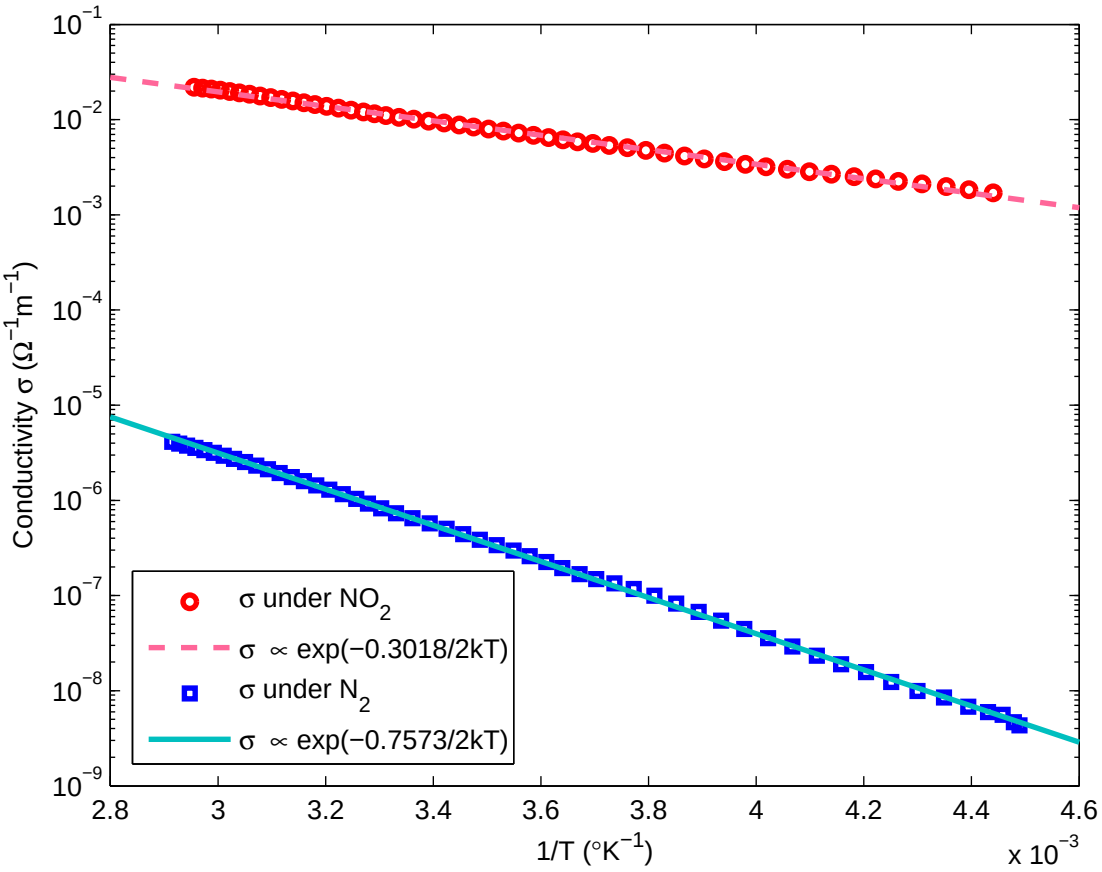

Figure 5.7: A plot of conductivity versus the inverse of temperature shows that temperature dependence of the FePc thin film sensor follows an Arrhenius conductivity model. The Arrhenius conductivity model makes the assumption that FePc thin film conductivity is proportional to the reaction rate of oxidizing gas species. The data yields fitted activation energy values of approximately 0.76 eV and 0.30 eV for intrinsic and extrinsic conductivity respectively.

In Figure 5.7, the Arrhenius conductivity model provides good fits with each series of data, yielding activation energies of approximately 0.76 eV and 0.30 eV for intrinsic and extrinsic conductivity respectively. For reference, activation energies for various MPc thin films are detailed in Table 5.1. From the results of this experiment, the 0.46 eV difference in activation energy can be attributed to the reduction in energy required to activate charge

carriers from a nitrogen dioxide-FePc complex. As mentioned before, exposing the sensor to ultra high purity nitrogen gas may not provide a true measure of intrinsic FePc thin film conductivity due to inadequate desorption of oxygen or other dopant gases. However, while the conductivity levels of the intrinsic case presented here may actually represent the effects of adventitious atmospheric dopants such as oxygen or relative humidity, the extrinsic conductivity results indicate that nitrogen dioxide doping can further reduce the activation energy of FePc film conductivity regardless of any previous atmospheric doping. In summary, regardless of intrinsic conductivity, extrinsic conductivity, dopant type, or doping levels, the temperature dependence of the FePc thin film sensor follows an Arrhenius conductivity model in temperature range of -46 to 71 °C.

Table 5.1: Activation energies for various MPcs

MPc	Intrinsic (eV)	Extrinsic (eV)	Reference
NiPc	0.703	0.32	[1]
PbPc	-	0.47	[2]
CoPc	0.66	0.24	[3]
CuPc	0.80	0.54	[4]
FePc*	0.76	0.30	-

* Experimental results from this research

5.2.4 Concentration dependence

Nitrogen dioxide concentrations at or near one part per million is of significant interest in that it has been set forth as the exposure limit by several health agencies. Military specifications have also set the leak criteria for nitrogen tetroxide at 1 ppm nitrogen dioxide. To determine sensor response around this concentration range, tests were conducted at nitrogen dioxide concentrations of 0.5 ppm, 1 ppm, and 2 ppm under room temperature (20 °C). For each test, two sensors were allowed to stabilize in ultra-high purity nitrogen for 30 minutes before nitrogen dioxide gas is introduced into the test cell for 30 minutes. This cycle was repeated. The flow rates for the 0.5 ppm, 1 ppm, and 2 ppm nitrogen dioxide tests were 0.95 L/min, 0.43 L/min, and 0.25 L/min respectively. Figure 5.8(a) is a superimposed plot of sensor response vs. time for the three concentrations. Figure 5.8(b) is a normalized resistance plot for the first 10 minutes of response to the three concentrations of nitrogen dioxide. The reference resistance value used for each series is the first resistance reading upon introduction of nitrogen dioxide. The slopes for the normalized resistance plot can be used to tell the concentration of nitrogen dioxide gas. From the plot, concentrations 0.5, 1, and 2 ppm nitrogen dioxide have average slopes of 0.1479 x 10^{-3} s^{-1}, 0.2121 x 10^{-3} s^{-1}, and 0.39309 x 10^{-3} s^{-1} respectively.

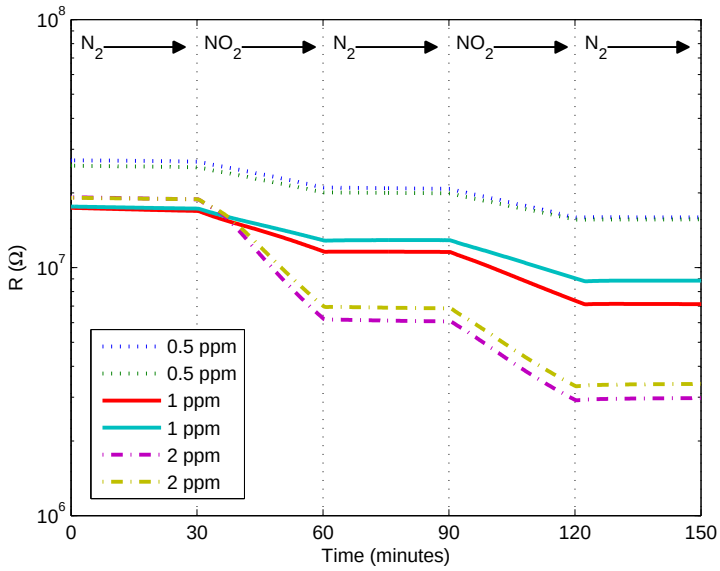

(a) Low concentration response

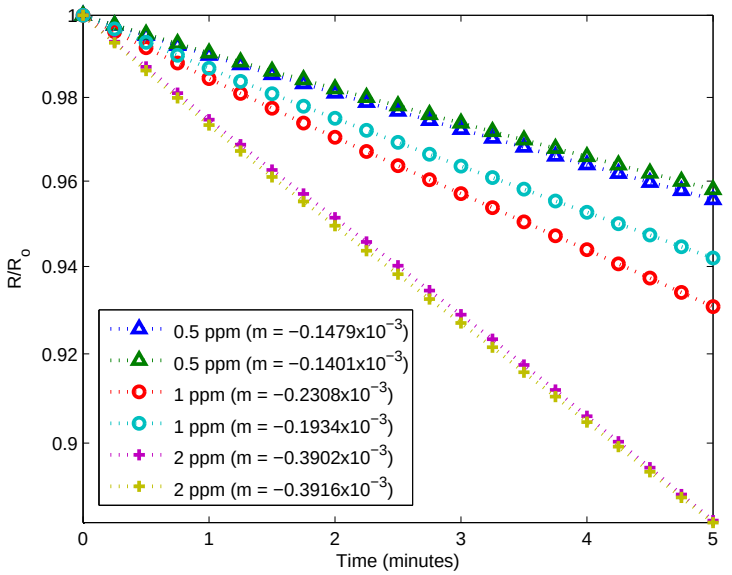

(b) Low concentration normalized response

Figure 5.8: (a) Room temperature response of sensors to 0.5, 1, and 2 ppm nitrogen dioxide, with high purity nitrogen introduced before and after each nitrogen dioxide exposure. (b) Normalized sensor response to nitrogen dioxide exposure; the reference value used for normalization is the first resistance reading for each exposure. The normalized resistance plot shows different rates of change in relative resistance corresponding to detection of different concentrations. The values for the slopes m for each series are provided in the legend and have units of s^{-1}.

5.2.5 Repeatability of sensor reponse

To investigate the repeatability of sensor response, two sensors were exposed to four successive 1 ppm nitrogen dioxide tests at 20 °C. Each cycle consisted of 30 minutes nitrogen dioxide exposure followed by 30 minutes of ultra high purity nitrogen. Figure 5.9 shows the response of the sensors for the duration of the entire test. Figure 5.9(b) is a superimposed resistance plot of each sensor's initial 5 minute response, normalized with respect to the first resistance reading of each exposure. For both sensors, subsequent exposure to 1 ppm nitrogen dioxide yielded consistent slopes, with the eight results showing an average slope of 0.2049 x 10^{-3} s^{-1} and a standard deviation of 2.0 x 10^{-5}. The sensors did not exhibit significant signs of reversibility despite the nitrogen flush cycles. This may be explained by the sensor possessing sufficient nitrogen dioxide adsorption sites such that the concentration levels and exposure durations at this operating temperature cannot provide the necessary conditions to saturate the sensor, thereby adsorption mechanisms control the sensor output while desorption mechanisms remain minimal. As reference, from previous high concentration experiments, sensor saturation occurred at roughly 30 minutes of 100 ppm nitrogen dioxide exposure. Therefore, empirically, the sensor can repeatedly sense 100 such nitrogen dioxide exposures until inevitably reaching saturation. These results demonstrate that a passive FePc sensor relies on its irreversibility at low concentrations to produce normalized resistance output that is mainly a function of the ambient nitrogen dioxide gas concentration.

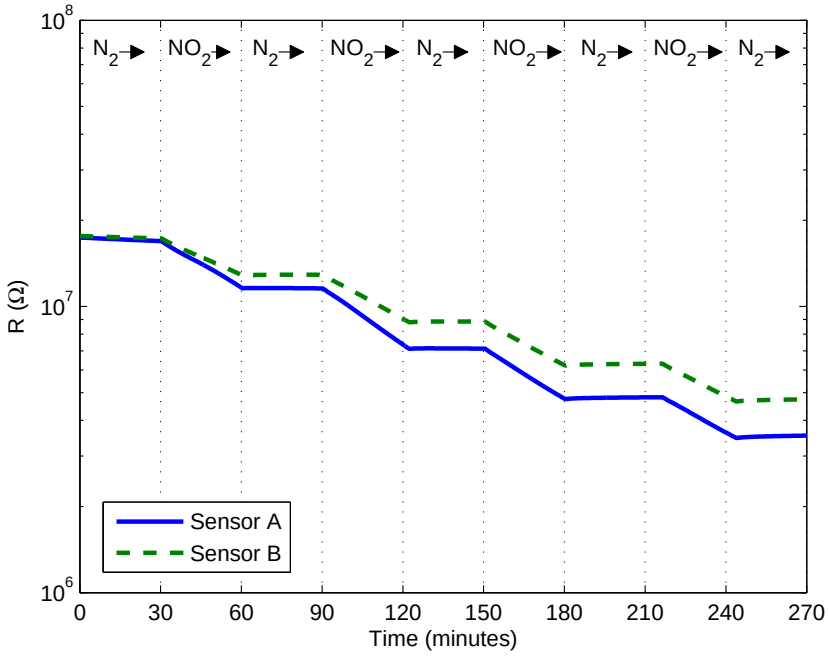

(a) Fixed concentration response

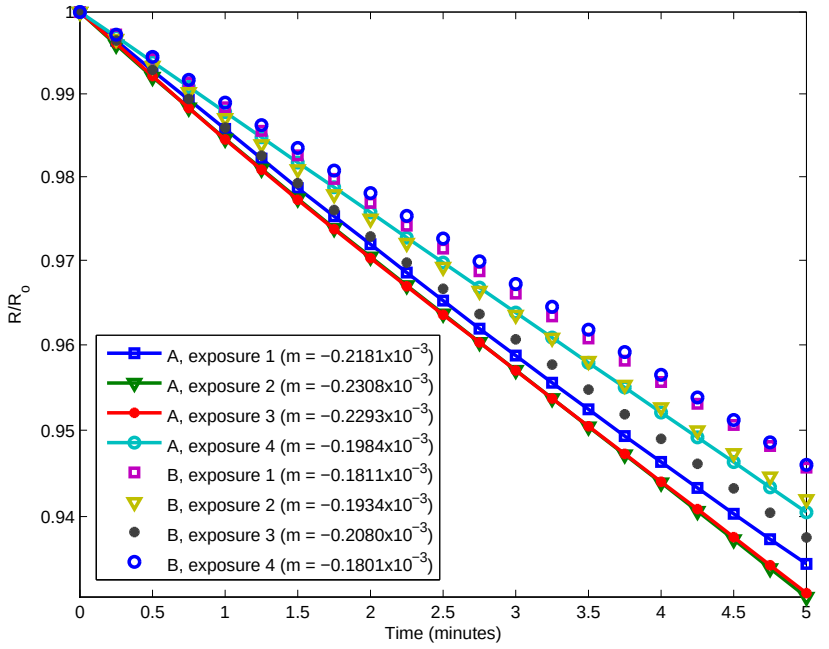

(b) Fixed concentration normalized response

Figure 5.9: (a) Room temperature response of two sensors to four repeat exposures of 1 ppm nitrogen dioxide, with high purity nitrogen introduced before and after each nitrogen dioxide exposure. (b) Normalized resistance plots of the first 10 minutes of each nitrogen dioxide exposure.

5.3 Sensor specificity

In these series of experiments, sensor response to other gases was investigated by observing the response of sensors to potential interferant gases, such as ammonia, high humidity air, and pure oxygen. High humidity air and pure oxygen were chosen for each species' constant yet unpredictable presence in atmospheric air, while ammonia has been known to affect MPc thin films and is a common cleaning chemical used in nitrogen textroxide storage containers.

5.3.1 Ammonia

General purpose chemical cleaning agents contain ammonium hydroxide (NH_4OH), which is composed of ammonia (NH_3) dissolved in water. Containers that hold nitrogen tetroxide are commonly cleaned with such cleansers and thus a good nitrogen dioxide leak detector is expected to show stability towards ammonia gas. Because ammonia is a polar molecule that acts as an electron donor, it readily reacts with strong electron accepting gases such as nitrogen dioxide or oxygen. For FePc thin films with lowered resistivity due to adsorbed oxygen or nitrogen dioxide, the presence of ammonia will remove the adsorbed molecules and increase the resistivity of the film, effectively reversing the effect of any adsorbed molecules and cleansing the film. This effect is observed in an experiment where a sensor stored in a desiccator under air is exposed to 100 ppm ammonia at room temperature for a duration of one hour. The response is plotted in Figure 5.10. During the experiment, the sensor resistance increased from approximately 1.3 x $10^8\Omega$ to over 6.3 x $10^8\Omega$. Although ammonia significantly affects the resistivity of FePc thin films, its effect represents a favorable condition, since it has an opposite effect compared to nitrogen dioxide; ammonia exposure can clean the surface of a FePc thin film and return its resistance to a higher baseline level. Ammonium treatment may thus be performed to establish consistent baseline resistance levels for sensors, or to revise sensors that have undergone calibration.

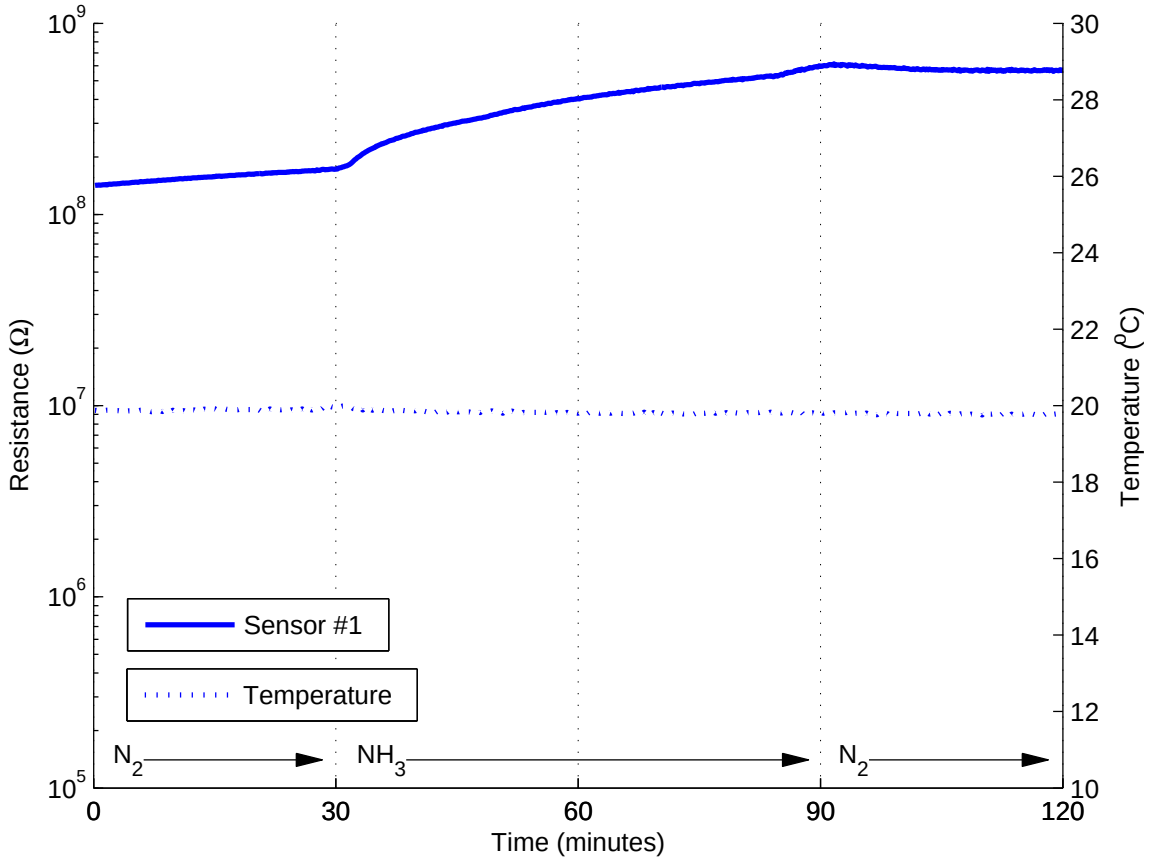

Figure 5.10: Sensor response to 100 ppm ammonia gas shows an increasing resistance trend upon exposure. The sensor resistance rose from approximately 1.3 x $10^8\Omega$ to over 6.3 x $10^8\Omega$ during a one hour exposure period. Ammonia gas is a reducing agent able to mildy remove oxidizing dopants on FePc thin films.

5.3.2 High humidity air

Humidity has been reported to affect MPc thin films such that researchers have believed certain MPc based sensors were not viable at temperatures below 100 °C due to humidity concerns. To investigate whether humidity affects the α-FePc thin film sensor, an experiment was conducted where a 450 nm sensor was stabilized in air and then suspended over water in a closed glass container for two hours with resistance monitored in real time. Figure 5.11 shows the resistance response of the sensor, along with the output from a Honeywell HIH-3610 humidity sensor and a T-type thermocouple. While the temperature remained a steady 22 °C throughout the experiment, the relative humidity in the container reached a stable 95%. The sensor resistance experienced an initial decrease from 1.2 x 10^7 to 1.1 x 10^7 Ω within a minute of entering the container. However, after remaining in the container for 20 minutes, the sensor resistance steadily returned to a value of 2 x 10^7 Ω and remained stable. It can be concluded that high humidity levels do not have a significant effect on the 450 nm FePc thin film sensor.

5.3.3 Oxygen

Oxygen in the air is known to adsorb onto FePc thin films and contribute to conductivity. To test the extent of the oxygen doping effect, four 450 nm FePc sensors were exposed to high concentration oxygen after being stored under dry air at approximately 21% RH under room temperature in a desiccator for many weeks. For the oxygen source, a standard industrial oxygen cylinder of 99.8% purity was obtained from Airgas. Figure 5.12 shows the oxygen response of the sensors. From the results, oxygen adsorbed onto FePc thin films does not contribute significantly to increased conductivity. The effect is small, with sensor resistances reduced by an average of 3 x 10^7 Ω over a duration of roughly 13.5 hours. However, for the duration of the test, there is an observable long term decrease in resistance that is enhanced on average from -8.61 x 10^5 Ω/hour to -2.3 x 10^6 Ω/hour as the oxygen flow rate is increased from 0.25 L/min to 1 L/min. This decrease in resistance due to oxygen is an

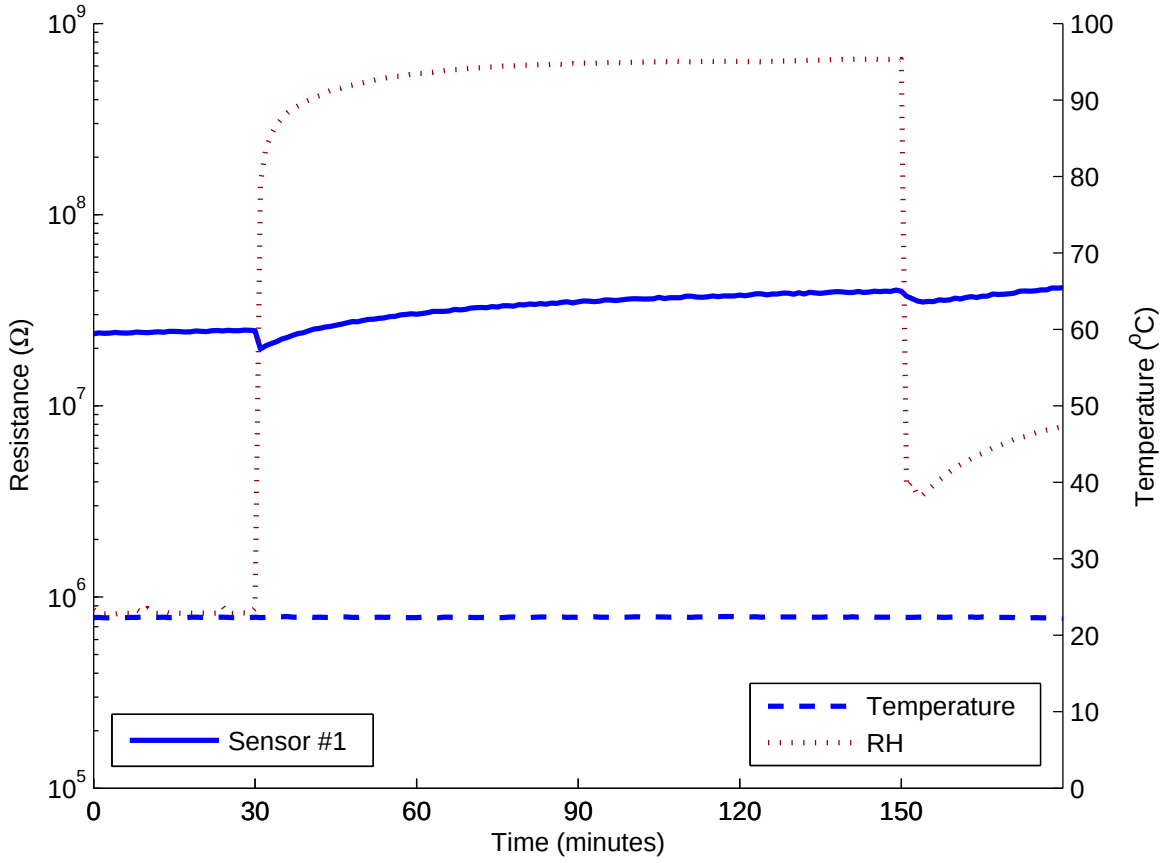

Figure 5.11: Resistance response of a sensor to high humidity, plotted with output from a Honeywell HIH-3610 humidity sensor and a T-type thermocouple. This plot shows that 450 nm α-FePc thin films possess a morphology that is stable to relative humidity levels as high as 95%.

exponentially decaying trend, thus it may be safe to assume that equilibrium with the pure oxygen environment will eventually be reached should the duration of the experiment be extended by roughly one to two days. In normal nitrogen dioxide detection, the slow oxygen doping effect observed in this experiment is very small compared to the many orders of magnitude decrease of resistance within an order of seconds. Therefore it can be concluded that while the concentration of oxygen in atmospheric air may be insufficient to saturate the FePc thin film sensor, in other words pure oxygen gas does result in additional conductivity increases, yet the effect of oxygen doping even with pure oxygen is too slow to significantly affect nitrogen dioxide detection.

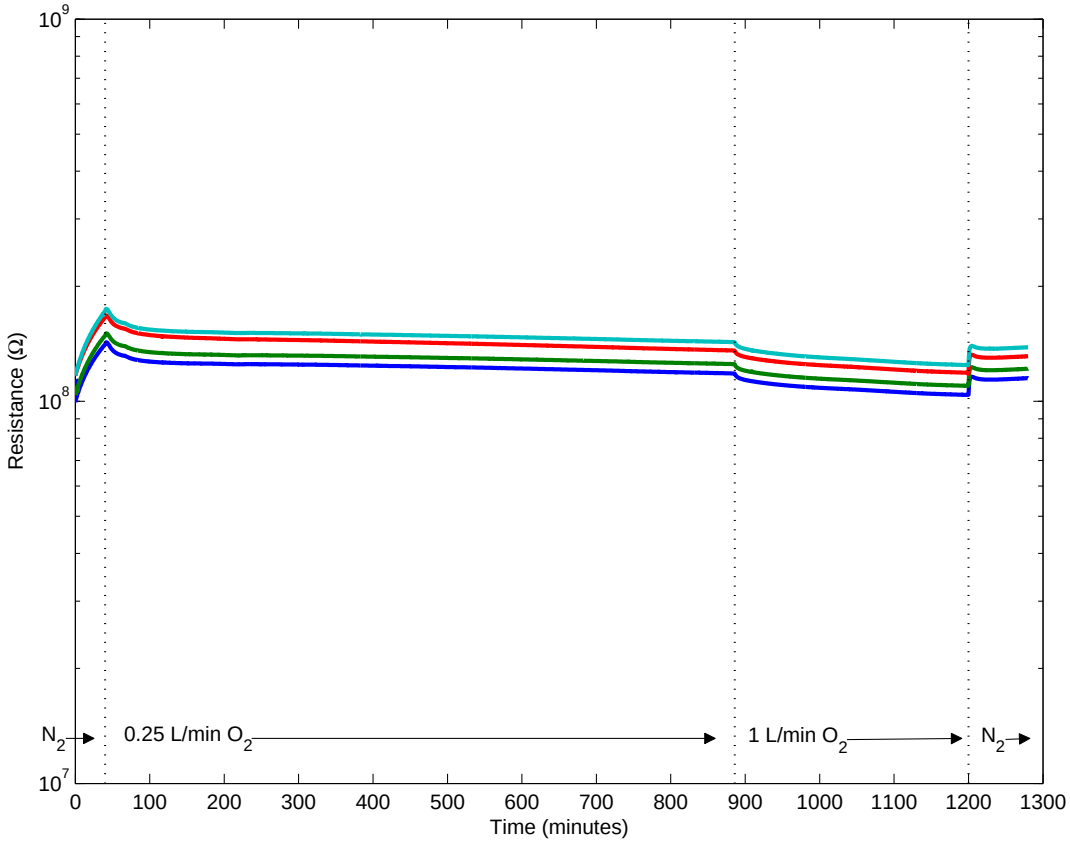

Figure 5.12: Sensor response to 99% oxygen.

5.4 Sensor longevity

In this section, sensor longevity is investigated. The passive FePc thin film sensor relies on high initial resistance levels to ensure a high capacity for adsorption and a large order of magnitude change upon exposure to analyte gas. Atmospheric interferants such as water vapor and oxygen may cause deterioration in sensing capability by reducing sensor resistance levels. For these reasons, sensor baseline resistance is a good indicator towards sensor longevity. To investigate sensor storage longevity, sensors were subjected to different storage conditions with resistances monitored over time. The storage conditions include open air, sealed air, and sealed nitrogen. To investigate sensor longevity during operation, a thermal cycle over the range of -50 to 80 °C under flowing nitrogen gas was conducted to determine how extremes in operating temperature affect baseline resistance. The results for sensor longevity are documented in the following subsections.

5.4.1 Storage longevity

Sensor storage is of significant importance in that storage conditions essentially determine a sensor's baseline resistance. Two primary constituents of atmospheric air that are known to affect FePc thin film resistivity are oxygen and humidity. Both oxygen and water vapor tend to adsorb onto FePc thin films and increase conductivity. Additionally, the presence of visible light or UV radiation is expected to affect FePc films due to its inherent photoconductivity, thus particular attention was paid towards UV shielding and proper storage. In this section, a set of tests were conducted to investigate sensor storage and how sensor resistance is affected.

To investigate the differences in storing sensors under a static air environment in the dark versus under an open air environment within a laboratory setting, an experiment was conducted where four 450 nm FePc sensors placed in each environment were monitored until sensor resistances reached an equilibrium. For reference, an additional four sensors were stored in a dark container under a static nitrogen atmosphere and monitored. For this

experiment, all 12 sensors were chosen from the same batch of fabricated sensors. Prior to subjecting the sensors to each respective storage condition, the sensors were stored in a dark vacuum box. The resistance versus time plot for this experiment is shown in Figure 5.13. Throughout the experiment, laboratory room temperature was a steady 20 °C. The results show that while initial sensor resistances were roughly $1G\Omega$ under vacuum, the sensors stored in nitrogen gas dropped to $500M\Omega$, the sensors stored under air in a closed dark container dropped to $40M\Omega$, and the sensors stored under open air dropped to $100K\Omega$ in resistance. The durations required to reach equilibrium resistance are one hour for sensors stored in nitrogen, four hours for sensors stored in closed air, and 20 hours for sensors stored in open air. These results indicate that while dark storage under static air is sufficient to arrest any resistance reduction within three hours, sensors in open air conditions require roughly a day to stabilize; by then, its resistance values would have decreased by an order of magnitude.

To test sensor response to proper storage environments, UV shielded desiccators were used. After fabrication, all sensors produced for this project were stored in UV shielded desiccators made with 99.9% UV-shielding clear acrylic material, and controlled to provide a dry air environment with less than 20 % relative humidity. To test the storage stability within these desiccators, newly fabricated sensors were placed inside and monitored. Prior to placement into the desiccator, although much care was taken, each sensor was briefly exposed to open air for about half an hour due to handling and transfer into the test cell. Figure 5.14 is a resistance plot of these sensors over the course of 10 days. As expected, the thicker 450 nm sensors exhibited higher stable resistance values of 10-50 MΩ, while the 200 nm sensors exhibited lower stable resistance values of 200-300 KΩ.

A high baseline resistance for a FePc thin film sensor indicates a pristine surface free of adsorbed gas species. Although FePc thin film sensors inevitably lose some of its resistivity when exiting a vacuum, storage in a dry, dark, and static environment can preserve most of its resistivity. In these storage experiments, sensors stored in a desiccator at 20% RH under air at room temperature are stable for 10 days, and there is no indication of any potential

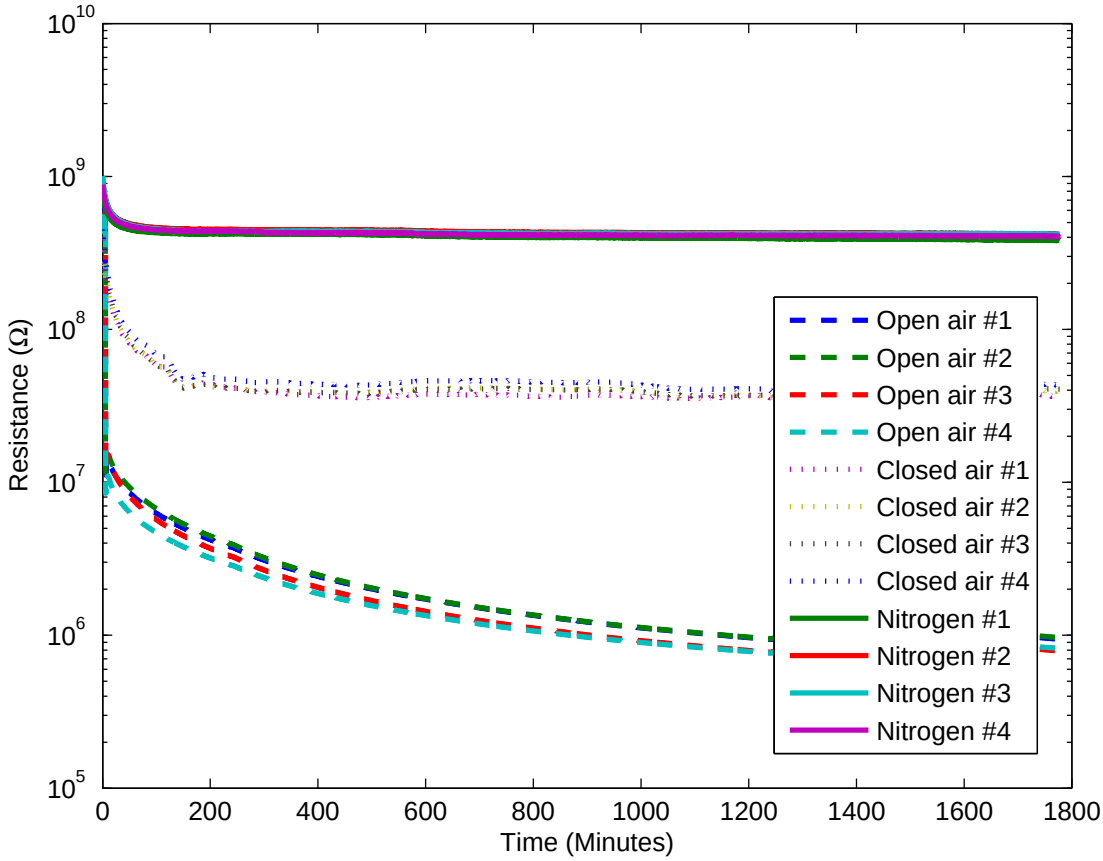

Figure 5.13: A resistance plot of sensors placed in open air, in a dark container with air, and under ultra high purity nitrogen gas to simulate and compare storage conditions. The temperature was a constant room temperature. Sensors stored under nitrogen and in a dark container were able to achieve stable resistances of 500 MΩ and 40 MΩ respectively within 3 hours. For the open air case, while stability is achievable within 20 hours, results show the reduction in baseline resistance to only 100 KΩ due to the compound effects of atmospheric oxygen doping, humidity, and various light radiation on FePc thin films.

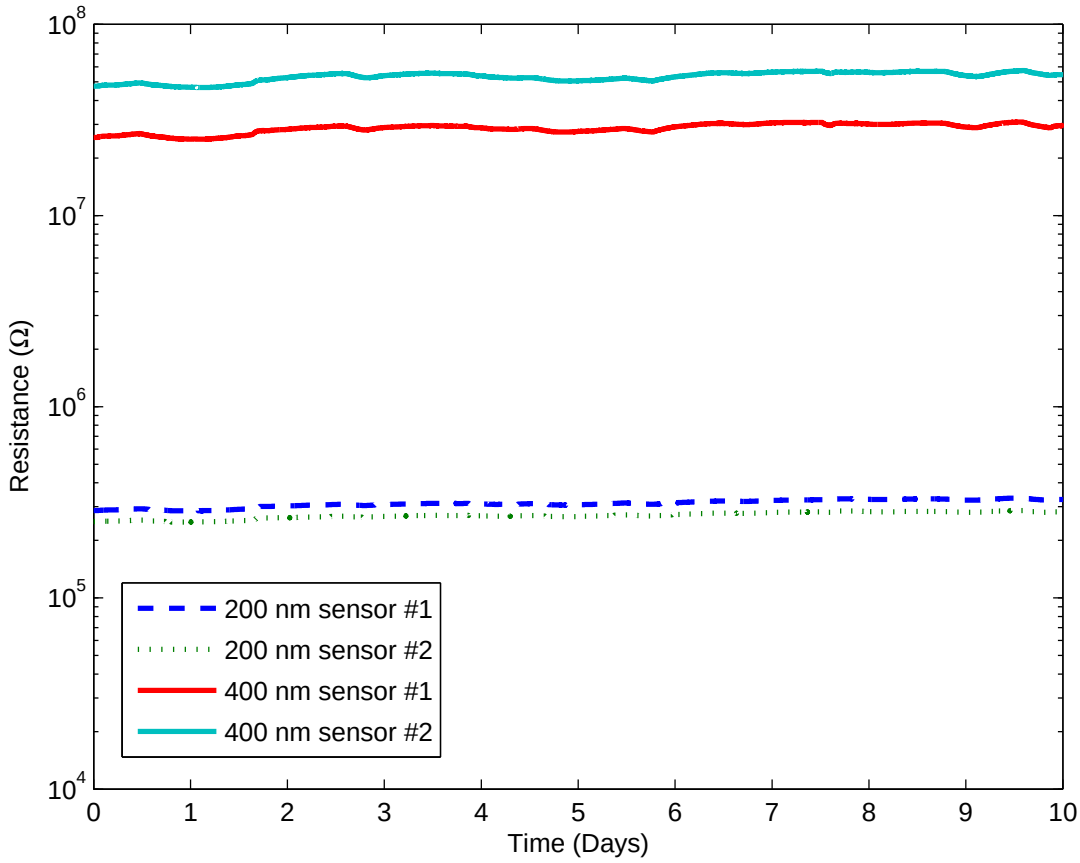

Figure 5.14: A 10 day resistance response plot for sensors placed in a UV shielded desiccator with relative humidity maintained at 20 %. The thicker 450 nm sensors exhibited higher stable resistance values of 10 50 MΩ, while the 200 nm sensors exhibited lower stable resistance values of 200 300 KΩ.

loss of that stability over time. Film morphology also plays a role in stable resistance values. Thicker 450 nm FePc thin films possess the thickness and morphology to remain at higher resistance values under storage in a desiccator (>1 x $10^7\Omega$), while 200 nm FePc sensors possess a much lower resistance (2-3 x 10^5 Ω). Thus not only are thicker 450 nm FePc thin film sensors more suitable as a passive sensor due to its adsorption capacity, but it is also more able to retain resistivity under storage. A downside to thicker FePc films is the longer durations required to reach stability, where nitrogen and contained air storage required 3 hours, reaching equilibrium with open air can take over 20 hours.

5.4.2 Operational longevity

To investigate operational longevity, sensors were subjected to repeating temperature cycles under 0.1 L/min flowing nitrogen gas. The temperature cycle profile begins at 20 °C, decreases to -50 °C, increases to 80 °C, and finally decreases back down to 20 °C. The temperature ramp rates are a constant 2 °C per minute. In this experiment, 11 total cycles were performed, spanning a total duration of roughly three and a half days. To compare the temperature dependence of film thickness and substrate type, one N-type oxidized silicon substrate, one P-type oxidized silicon substrate, and one quartz substrate sensor were taken from each of four different FePc deposition batches. The four different batches have FePc thin film thicknesses of 50, 100, 150, and 200 nm. This makes a total of 12 different sensors all exposed to the same test conditions under simultaneous monitoring. The complete resistance response plots for all 12 sensors are shown in Figure 5.15, while Figures 5.16, 5.17, 5.18, and 5.19 show the results for sensors with film thicknesses of 50, 100, 150, and 200 nm respectively.

From the resistance responses in Figure 5.15, it can be observed that the initial thermal cycles show steadily increasing resistance readings. This can be explained by the desorption of oxygen molecules, which have been allowed to dope the FePc thin films while the sensors were exposed to air during handling and storage. However, after a few cycles, the resistances stabilize as the adsorption-desorption kinetics of the film achieve equilibrium with the nitrogen environment. At that point, the resulting changes in resistance become a strict function of temperature. It can also be observed that sensors with thicker films require more thermal cycles in order to reach equilibrium. From Figures 5.16, 5.17, 5.18, and 5.19, the 50 nm sensors required three cycles to reach a steady equilibrium, the 100 nm sensors required four cycles to reach a steady equilibrium, the 150 nm sensors required at least six cycles to reach a steady equilibrium, and 200 nm sensors only approach a steady equilibrium even after 10 cycles. For comparison between the substrate types, sensors with N-type and P-type oxidized silicon substrates generally behaved the same, while sensors with quartz substrates consistently showed higher resistance readings at low temperatures, especially with the 200

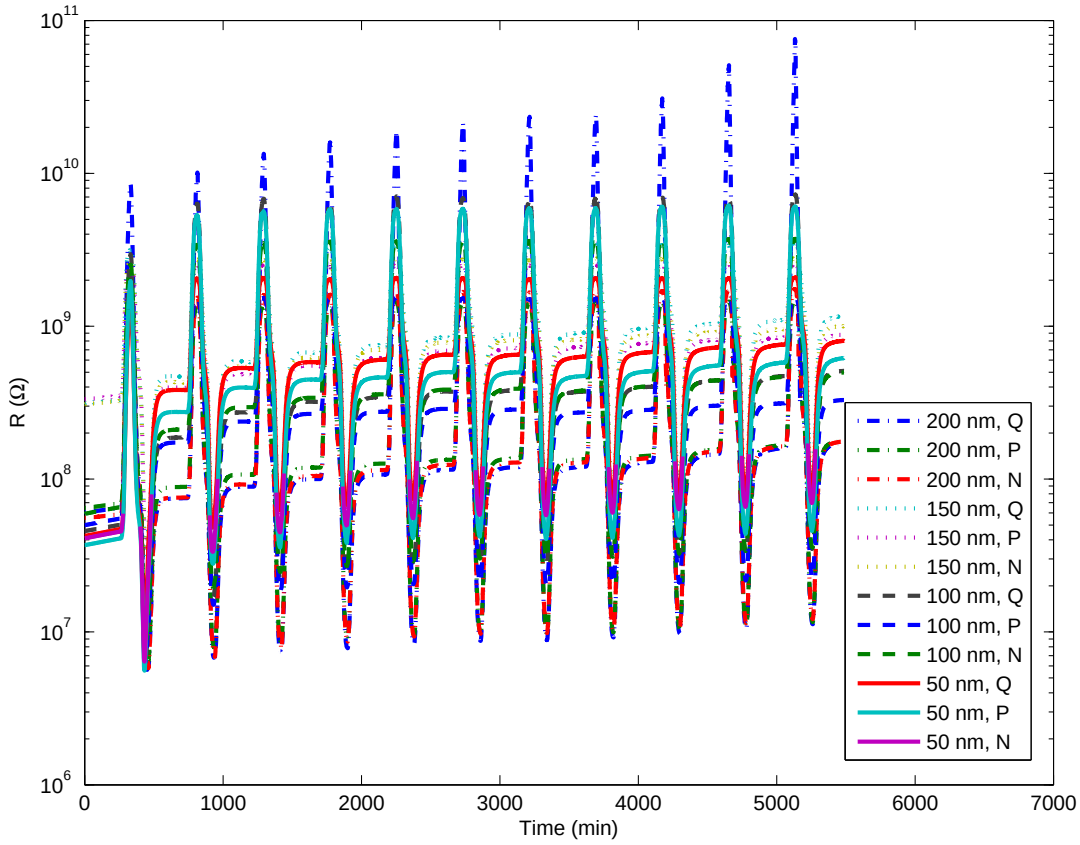

Figure 5.15: Under nitrogen gas, the temperature cycle of 12 different sensors representing three different substrate types and four different film thicknesses show that film resistance is mainly a function of temperature. The initial few cycles show steadily increasing resistance readings due to the desorption of oxygen molecules, which tends to dope the film. After a few cycles, the resistances reach stability as the adsorption-desorption kinetics of the film achieve equilibrium with the environment. The resulting changes in resistance become a strict function of temperature.

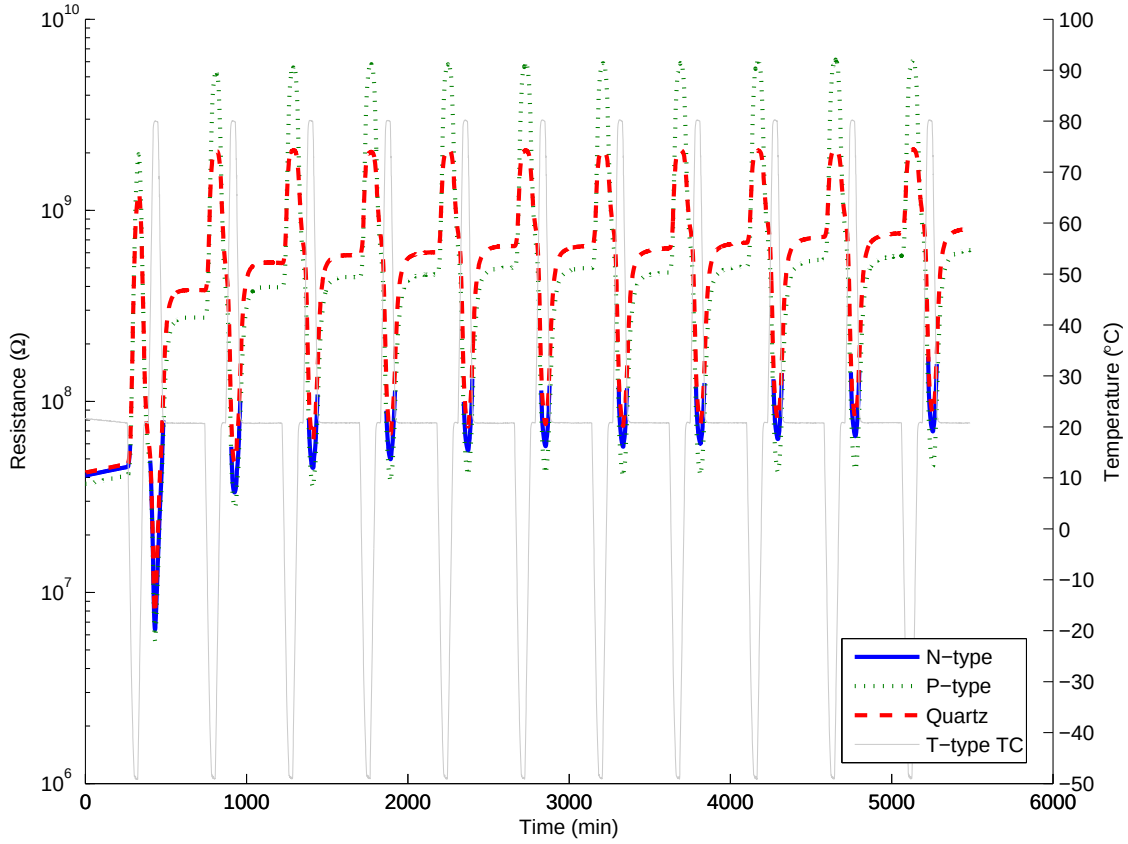

Figure 5.16: Temperature cycle of 50 nm FePc thin film sensors show that steady gas adsorption-desorption equilibrium with the environment is reached after three cycles, upon which the resistance values become mainly a function of temperature. For these sensors, p-type oxidized silicon substrates exhibited a much higher resistance value at -50 °C compared to the quartz and n-type oxidized silicon substrates.

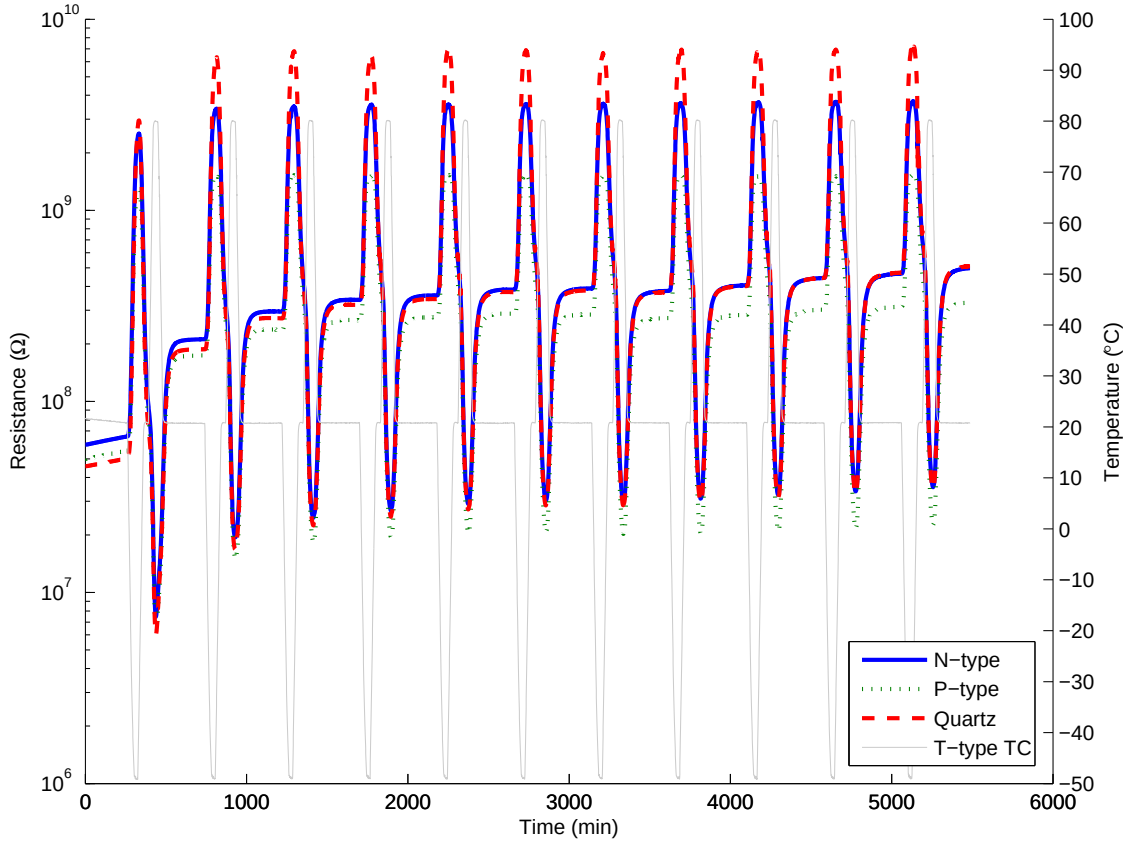

Figure 5.17: Temperature cycle of 100 nm FePc thin film sensors show that steady gas adsorption-desorption equilibrium with the environment is reached after four cycles, upon which the resistance values become mainly a function of temperature. For these sensors, quartz substrates exhibited a much higher resistance value at -50 °C compared to the p-type and n-type oxidized silicon substrates.

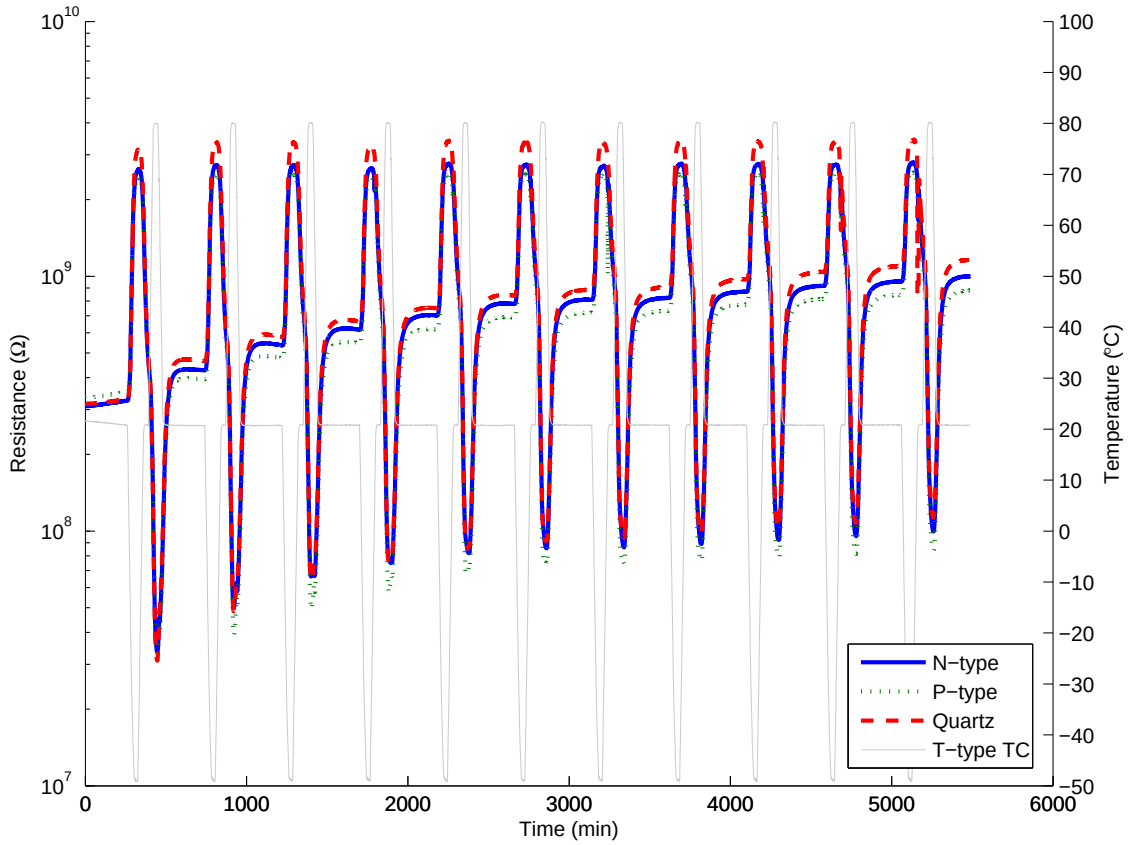

Figure 5.18: Temperature cycle of 150 nm FePc thin film sensors show that steady gas adsorption-desorption equilibrium with the environment is not reached until after six cycles, upon which the resistance values become mainly a function of temperature. The difference between n-type, p-type, and quartz substrates is not as pronounced as the other cases.

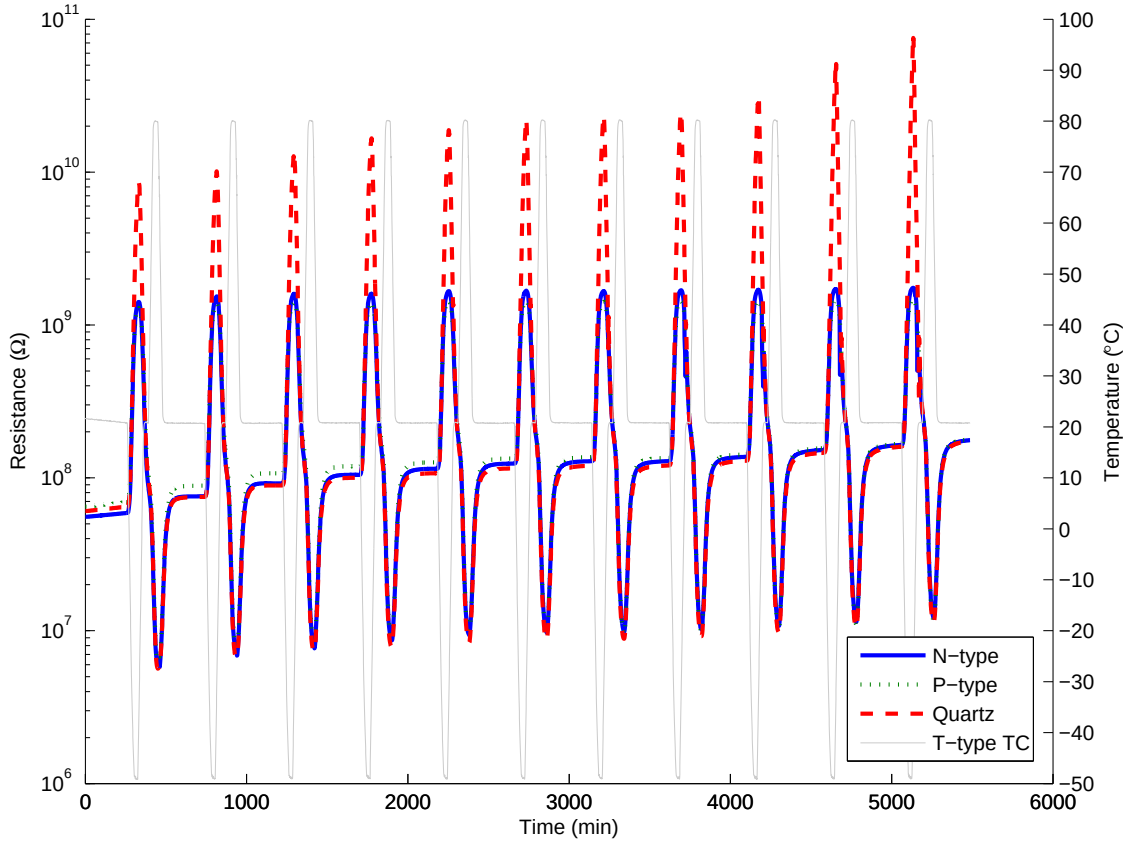

Figure 5.19: Temperature cycle of 200 nm FePc thin film sensors show that steady gas adsorption-desorption equilibrium with the environment is not reached even after 11 cycles. While the p-type and n-type substrate sensors behave almost identically, the quartz substrates show extremely high resistance values in excess of 1 x $10^{10}\Omega$ when temperatures reach -50 °C, and these resistance peaks increase with each temperature cycle.

nm film. It is postulated here that this is due to quartz possessing a slightly larger thermal expansion coefficient with 0.59 ppm/K, compared to amorphous silicon with 0.5 ppm/K. However, the most important result of this thermal cycling experiment is that FePc thin films can reach stability in a nitrogen atmosphere within the temperature range of -50 to 80 °C.

5.5 Sensor fabrication parameters

In this research, the major sensor fabrication parameters are film thickness, substrate type, and post-deposition heat treatment. During fabrication, FePc thin films of various thicknesses ranging from 50 to 450 nm were produced. These films were vacuum sublimed onto three substrate types: n-type oxidized silicon, p-type oxidized silicon, and quartz. To optimize the FePc thin film morphology, post-deposition heat treatments ranging from 20 to 340 °C were conducted. Results from the analysis of these fabrication parameters are presented in this section.

5.5.1 Film thickness

Film thickness in vapor deposited polycrystalline FePc films plays a large role in its morphology, which in turn greatly impacts its electrical characteristics. An observation in preliminary findings is that under air, sensors with thicker FePc films exhibit higher and more stable resistance values compared to sensors with thinner films. This can be explained by the increased distance between the surface of the film and underlying electrodes. In preliminary findings as well as previous work, it can also be generalized that for sensors saturated under 100 ppm nitrogen dioxide, thicker FePc film sensors possess greater conductivity than thinner films. The hypothesis is that given sufficient doping, charge carriers liberated in the thicker FePc film have more conducting pathways to travel, due to the greater bulk and cross sectional area between electrodes. Understanding the film morphology of FePc films that were vacuum sublimed onto the sensor substrates can shed more light on these effects.

To investigate film morphology, scanning electron microscope (SEM) images at 40,000-45,000x magnification were taken for all fabricated FePc thin films and presented in Figures 5.20 to 5.27. The FePc thin films in this experiment were vacuum sublimed onto sensor substrates at room temperature resulting in a microcrystalline α-FePc thin film. The regions observed in these images lie within the 15 micron gap that exists between electrodes. The substrate underneath this region is amorphous silicon dioxide, thermally oxidized from silicon wafers. The evolution of grain growth as thickness increases is obvious, as small grains initially grow in size until they begin impeding each other's growth, upon which vertical rod-like growth proceeds as seen in Figure 5.22. As thickness increases, the rod-like structures may occasionally combine, to form larger rods, resulting in structures with increasingly larger diameter, as seen in Figures 5.24 to 5.27. The total surface area of FePc thin films does increase as thickness increases, potentially allowing for more surface adsorption sites upon which electron accepting gas molecules can be adsorbed. The result is more charge carriers are liberated in the bulk and thus less resistance is detected between the electrodes.

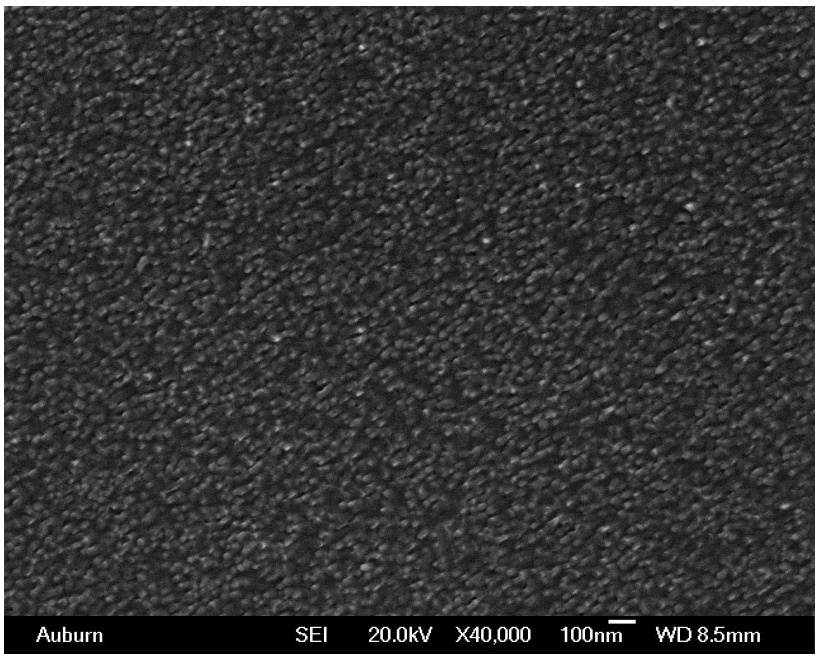

Figure 5.20: SEM image of 50 nm FePc thin film vacuum sublimed at room temperature onto amorphous silicon dioxide shows fine α-FePc grains of roughly 20-30 nm in size well distributed throughout the substrate.

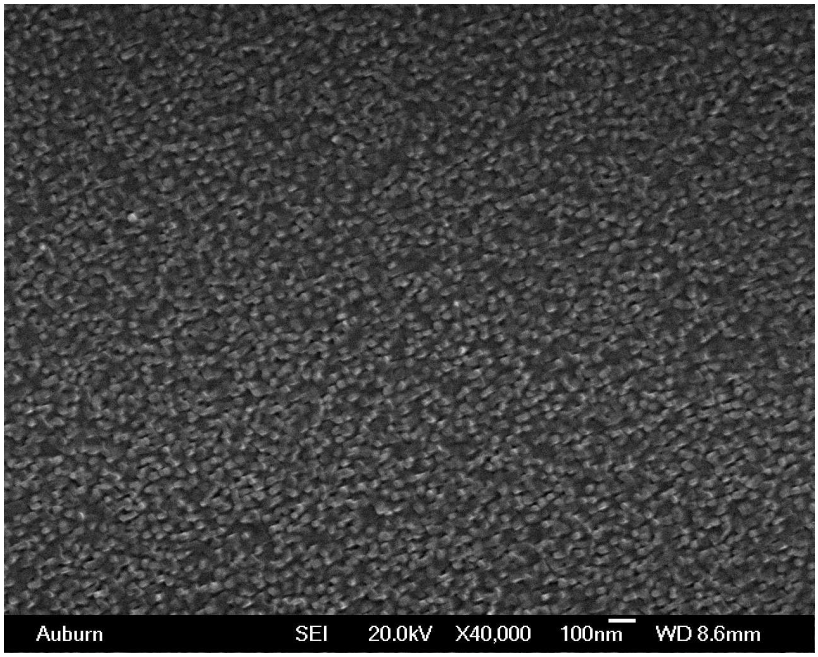

Figure 5.21: SEM image of 100 nm FePc thin film shows slightly larger grain sizes and a more dense distribution of grains across the surface of the substrate.

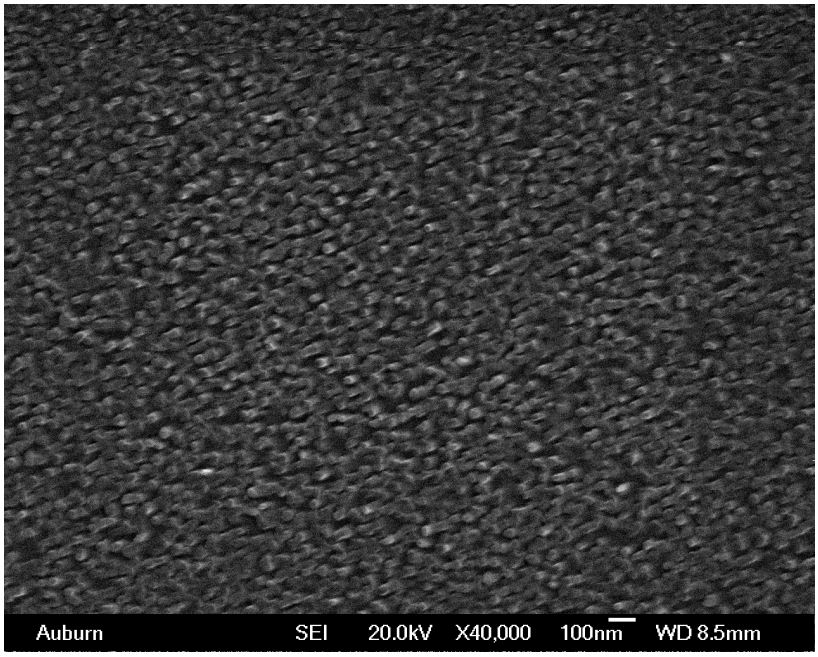

Figure 5.22: SEM image of 150 nm FePc thin film shows the onset of grains growing into rod-like structures in a vertical direction away from the substrate. Grain sizes are also visibly larger.

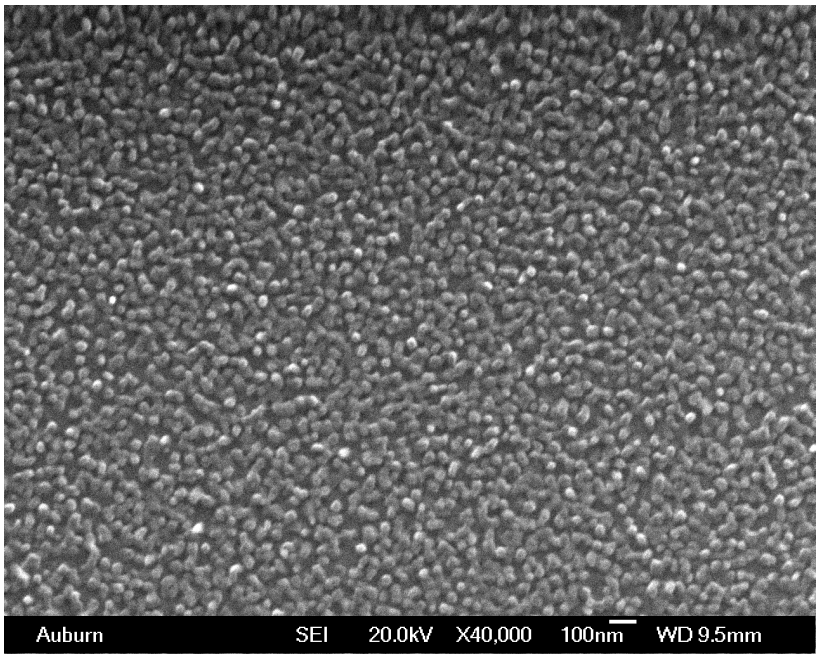

Figure 5.23: SEM image of 200 nm FePc thin film shows continued vertical growth of the α-FePc grains. The grain size is now at roughly 40-60 nm.

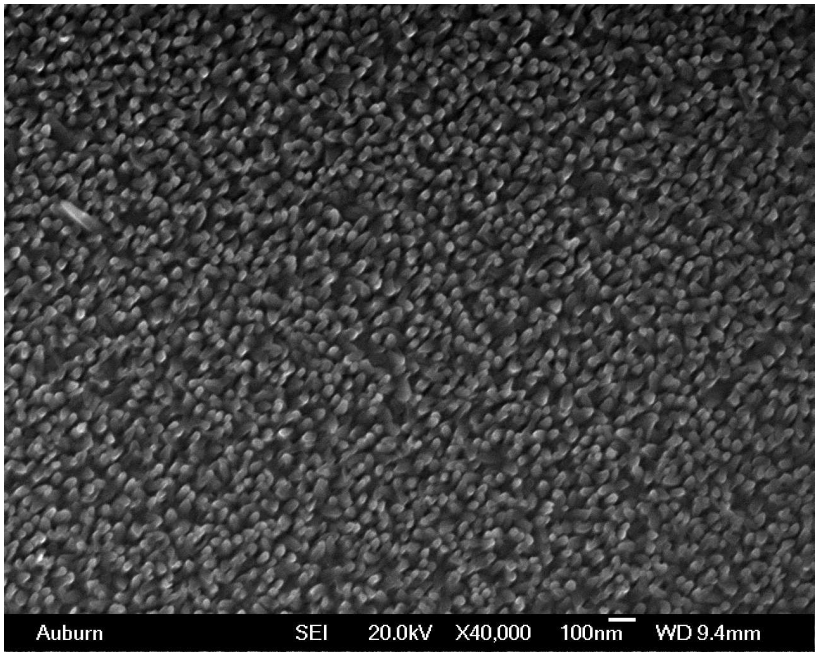

Figure 5.24: SEM image of 250 nm FePc thin film shows very well saturated growth of rod structures, without a significant increase in grain size, each slightly oriented in a seemingly random direction.

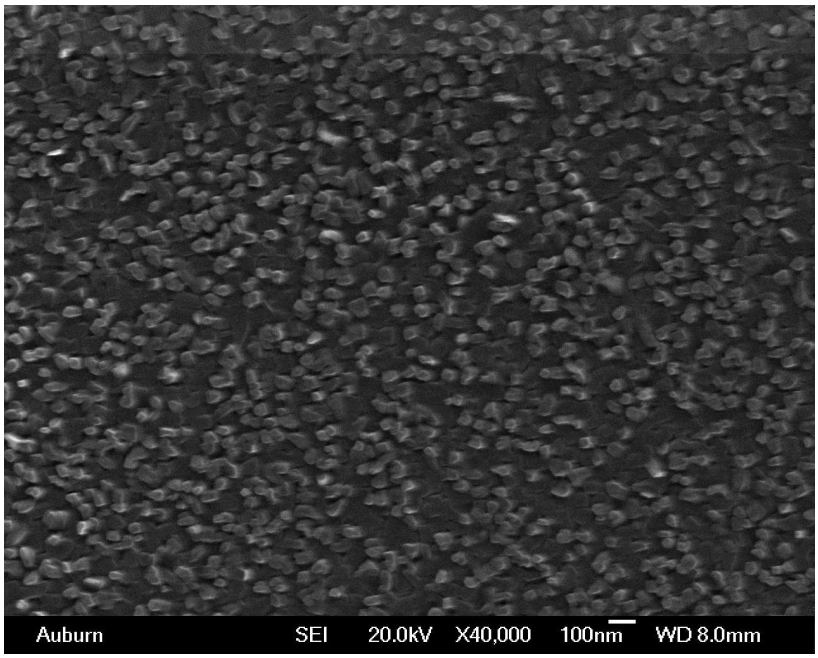

Figure 5.25: SEM image of 300 nm FePc thin film shows that as available space is exhausted, some grains combine and experience preferable growth, while others stop growing at a certain level. The new grain growth actually creates space atop other grains.

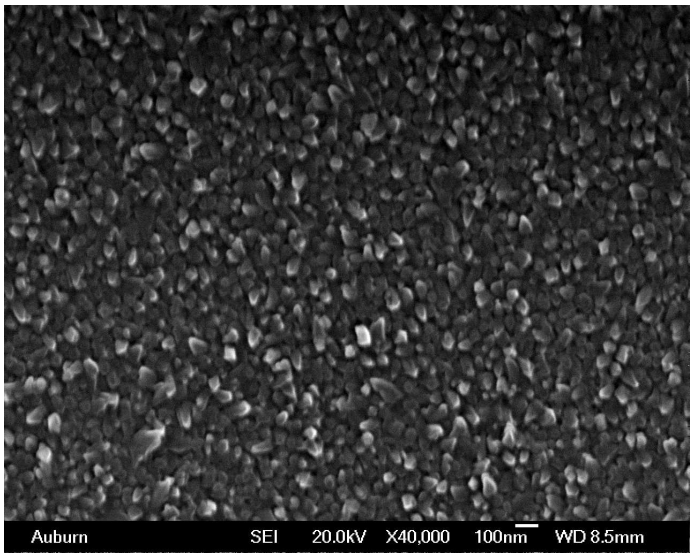

Figure 5.26: SEM image of 350 nm FePc thin film shows available space consumed by further grain growth. Existing grains growing in size and new grains seeded on top of old grains have both combined to create a very rough microcrystalline surface, with grain sizes ranging from 20 to over 100 nm.

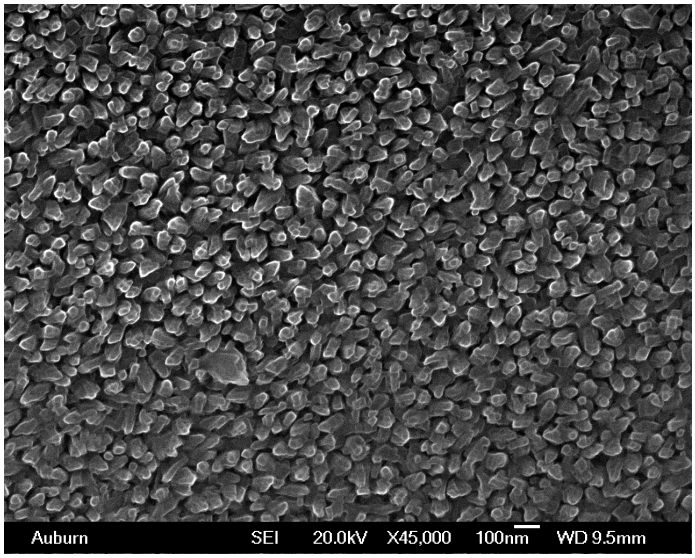

Figure 5.27: SEM image of 450 nm FePc thin film shows even more pronounced grain growth, both vertically in rod-like fashion and laterally to take up available space. This markedly rougher film simultaneously possesses the highest resistance values under air as well as the lowest resistance values under nitrogen dioxide, a character attributable to the film's roughness and continuity.

Film thickness also affects film resistance due to the quality of contact with the electrode fingers. Since the electrodes were deposited to a thickness of 200 nm over the silicon dioxide or quartz substrate, the side face that serves as the contact face with the FePc thin film is oriented perpendicular to the substrate. Assuming that FePc grain growth orientation on gold is similar to that on silicon dioxide (away from the substrate plane), then it is expected that FePc grains growing from the side of the electrode and FePc grains growing from the silicon dioxide substrate would result in grain orientation mismatch at the interface. This discontinuity in the FePc thin film may affect measured sensor resistance values. To examine this discontinuity, SEM images at the interface region were taken for sensors with FePc thin films of 250, 350, and 450 nm in thickness. These images are presented in Figure 5.28. From the images, it is noticeable that for the 450 nm film, grain growth bridging the interface is possible, whereas for the thinner films, there is a greater film discontinuity at the interface. In air at room temperature, the measured resistance values are roughly 5, 10, and 50 MΩ on average, and after reaching saturation from exposure to 100 ppm nitrogen dioxide, the sensor resistance values reach around 50, 10, and 3 kΩ, for the 250, 350, and 450 nm sensors respectively. While the 450 nm sensors possess the highest initial resistance, it also has the lowest saturation resistance. From the SEM images, the reason for this characteristic may simply be due to an improved film interface with the electrode.

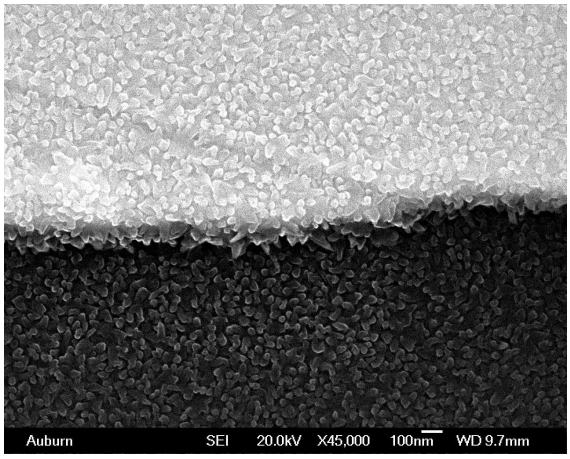

(a) 250 nm FePc

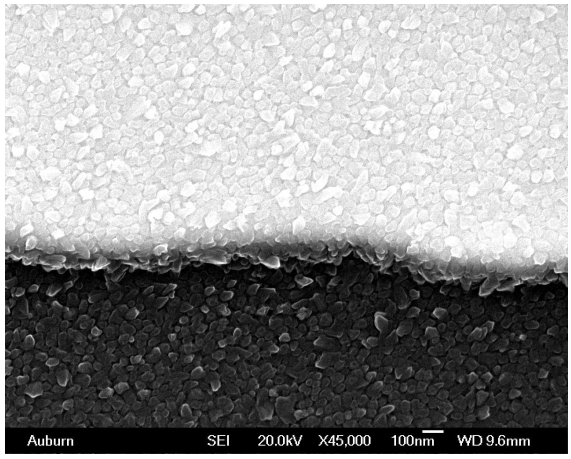

(b) 350 nm FePc

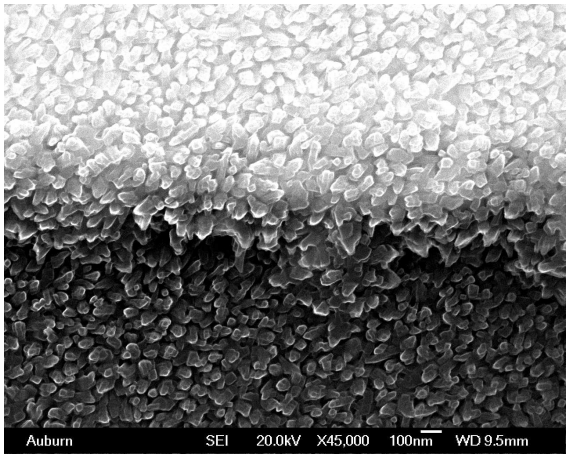

(c) 450 nm FePc

Figure 5.28: SEM images taken at the interface between FePc thin film and the gold electrodes for 250, 350, and 450 nm sensors. For the 450 nm film, grain growth bridging the interface is possible, whereas for the thinner films, there is a greater film discontinuity at the interface.

5.5.2 Substrate type

The FePc thin film sensors in this research were fabricated on three substrate types: amorphous silicon dioxide from n-type (phosphorous) silicon oxidation, amorphous silicon dioxide from p-type (boron) silicon oxidation, and (100) quartz. The silicon dioxide layer thickness for both n-type and p-type wafers were performed via wet etching to a thickness of approximately 1 micron. To investigate any difference in morphology, SEM images were taken. Figure 5.29 shows SEM images for 250 nm and 350 nm FePc thin films vacuum sublimed onto each substrate type. For each thickness, the images show that FePc film morphologies are relatively similar in terms of grain size and distribution, despite the difference in substrate type. Some slight visual difference can be detected, however these can be attributed to the different brightness levels and contrast ratios for each image. Electrical resistance measurements also confirm the similarity in morphology across the substrates, as presented in the thermal cycling results of Figure 5.15. Since all three substrates essentially consist of the same material in silicon dioxide, and that both amorphous silicon and quartz are relatively smooth compared to the large molecular and unit cell size of FePc, this result is somewhat expected. In summary, the differences in sensors based on each substrate type are less significant compared to the differences from the other fabrication parameters.

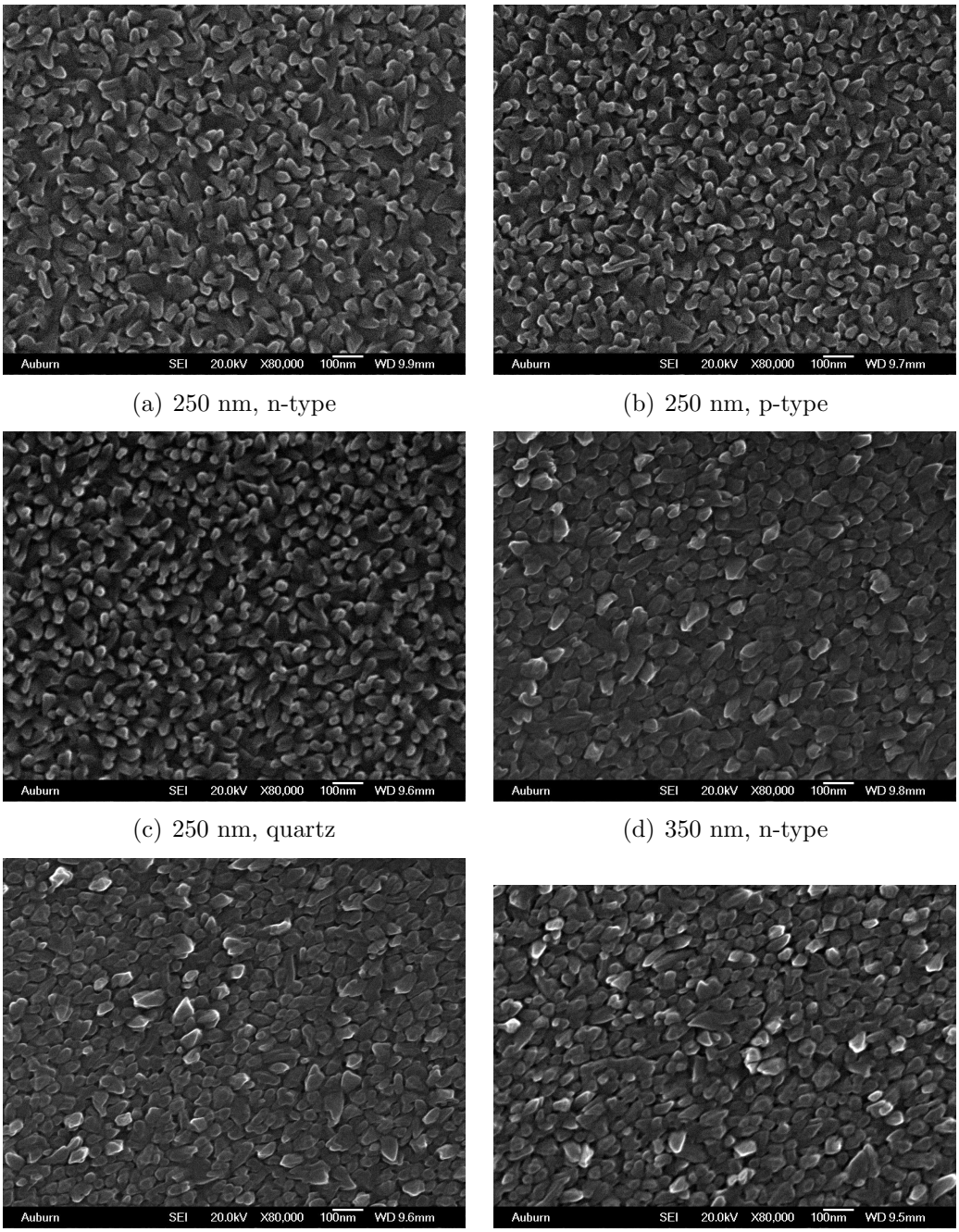

(a) 250 nm, n-type

(b) 250 nm, p-type

(c) 250 nm, quartz

(d) 350 nm, n-type

(e) 350 nm, p-type

(f) 350 nm, quartz

Figure 5.29: Visual comparison of FePc films deposited on n-type oxidized silicon, p-type oxidizied silicon, and quartz substrates show similar morphologies under SEM for 250 nm and 350 nm thick films respectively. (In these images, contrast and brightness were not normalized.)

5.5.3 Post-deposition heat treatment

Heat treatment of FePc thin films can affect film morphology and crystal structure, and in turn affect sensor response to nitrogen dioxide. To investigate the effect of heat treatment, identical 450 nm FePc thin film sensors fabricated from the same batch were subjected to nine different temperatures for a duration of two hours. Each heat treatment was conducted in a furnace under air. The annealing temperatures ranged from 20 (no heat treatment) to 340 °C. For reference, at temperatures above 200 °C, revaporization of Pc thin films has been reported to occur. Figure 5.30 shows AFM images taken from the surfaces of sensors for each heat treatment. For reference, a sensor that had not been heat treated was included in this test. Though grain growth was expected to occur at higher temperatures, for annealing temperatures of 250 °C and below, no significant visual change in the surface morphology of the FePc thin film was observed. At annealing temperatures of 280 °C and higher, significant re-evaporation of the film occured, as visual surface features increasingly diminished. For sensors with annealing temperatures 220 °C and higher, resistances were unable to be measured at the standard 1 V bias, indicating film continuity between electrodes has been sufficiently disrupted by the heat treatment.

In addition to investigating heat treatment effects on film morphology, a secondary objective of this experiment is to identify the best film for passive nitrogen dioxide detection. After AFM analysis, the 10 sensors were subjected to a 100 ppm nitrogen dioxide gas exposure experiment at room temperature. The resulting relative resistance change versus time for each sensor is plotted in Figure 5.31. In this test, only sensors heat treated at under 220 °C managed to produce a resistance response; the sensors that have been heat treated at temperatures above 220 °C may have experienced substantial reevaporation, such resistance readings could not be recorded. From the plot, the response trends indicate that as heat treatment temperatures increases towards 190 °C, the relative resistance decrease is larger. Assuming that relative resistance is a measure of the saturation state of surface adsorption sites on the sensor, a lower relative resistance indicates greater surface coverage.

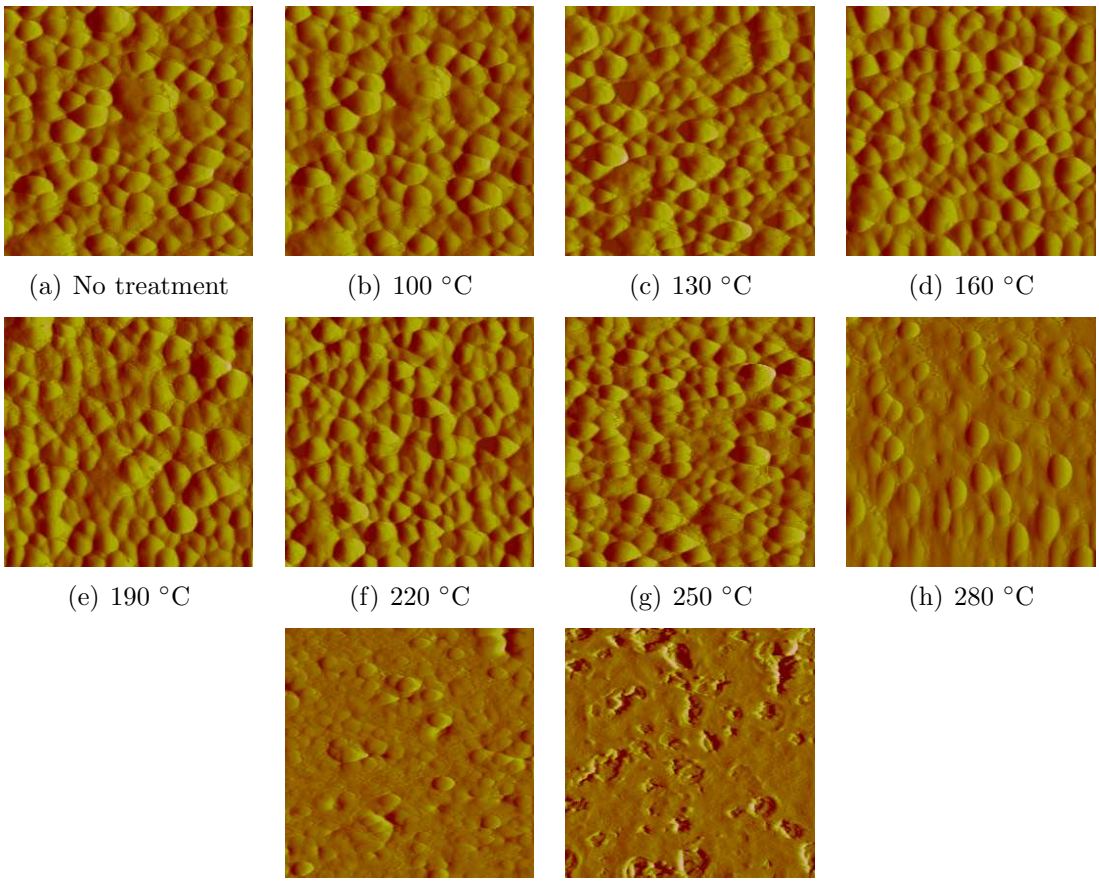

(a) No treatment (b) 100 °C (c) 130 °C (d) 160 °C

(e) 190 °C (f) 220 °C (g) 250 °C (h) 280 °C

(i) 310 °C (j) 340 °C

Figure 5.30: For sensors treated at or below 250 °C, AFM of 450 nm FePc thin films heat treated at various temperatures show no significant effect of heat treatment on sensor morphology, although grain restructuring and growth was anticipated to occur. The reason may be that a heat treatment duration of two hours was insufficient to allow significant diffusion, or that grain restructuring from α-FePc to β-FePc has occured beneath the surface within the bulk. As for films heat treated at 280 °C and higher, significant reevaporation of the FePc thin film can be observed, which can explain why resistances were not measureable accross the underlying electrodes.

For higher temperature treated films, the larger decrease in relative resistance suggest that heat treatment either reduces the total amount of surface coverage sites available for gas adsorption, or exposes hard to reach adsorption sites and makes all adsorption sites more uniformly accessible. Either case suggests that FePc films without heat treatment possess greater capacity for detection without reaching saturation. Saturation conditions should be avoided because at such conditions, the analyte adsorption-desorption kinetics are no longer dependent on analyte concentrations but instead are dominated by the low availability of adsorption sites on the film.

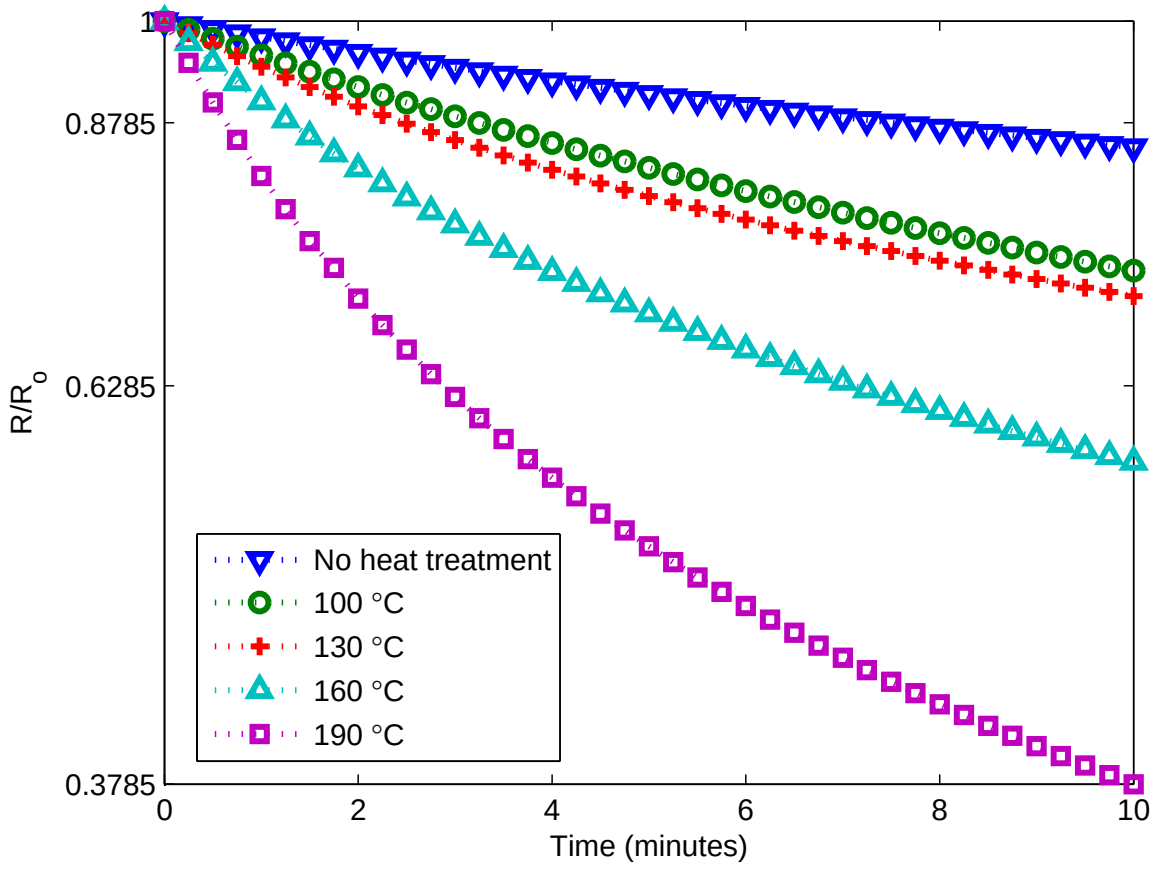

Figure 5.31: The relative resistance change of various heat-treated sensors exposed to 100 ppm nitrogen dioxide show that as-deposited FePc thin films without heat treatment forms a linear trend when plotted on a log scale, while heat treated films tend to experience higher order effects as heat treatment temperature increases.

For a sensor that monitors relative resistance change as a response to presence of analyte, higher temperature annealed sensors may possess greater sensitivity (due to its larger relative resistance change), but would also require a functioning reversing mechanism to address its ease of saturation. Thus, for a passive integrating sensor, FePc films without heat treatment would provide better characteristics for detection, provided that its sensitivity is adequate for the target analyte concentrations that it is designed to detect.

References

[1] M. EL-Nahass, A. EL-Deeb, and F. Abd-El-Salam, "Influence of temperature and frequency on the electrical conductivity and the dielectric properties of nickel phthalocyanine," *Organic Electronics*, vol. 7, pp. 261-270, 2006.

[2] C. J. Liu, J. C. Hsieh, and Y. H. Ju, "Response characteristics of lead phthalocyanine gas sensor - effect of operating temperature and postdeposition annealing," *Journal of Vacuum Science and Technology A*, vol. 14(3), pp. 753–756, 1996.

[3] F. Yakuphanoglua, M. Kandazb, M. Yarasir, and F. Senkal, "Electrical transport and optical properties of an organic semiconductor based on phthalocyanine," *Physica B*, vol. 393, pp. 235-238, 2007.

[4] I. Zhivkov, E. Spassova, D. Dimov, and G. Danev, "Oxygen influence on the conductivity of copper phthalocyanine vacuum-deposited thin films," *Vacuum*, vol. 76, pp. 237-240, 2004.

Chapter 6

Models and Predictions

There are two primary mechanisms that occur in the FePc thin film sensor presented in this research. The first involves the electrical conduction mechanism in the FePc thin film, as hole carriers mobilize under the application of a potential difference across the underlying electrodes. The second mechanism involves sensor resistance changes due to gas adsorption and desorption interactions between the FePc thin film and analyte gas molecules. Modeling each mechanism can yield a method of evaluating sensor output as well as lead to a better understanding of the sensor's performance.

The modeling of electrical conduction in the FePc thin film involves two approaches, one assuming bulk conductivity, and the other assuming only surface conductivity; although in reality the complexity of film morphologies might suggest simultaneous contributions from both bulk and surface conduction. A simple model that accounts for the electrode pattern of the FePc sensor for each method of conduction shall be presented.

The response of FePc thin film sensors to analyte gases presented in this research can be modeled based on gas adsorption-desorption kinetics. Gas chemisorption onto solids has been extensively modeled by prior researchers using the Elovich equation [1], which expresses film surface coverage as a function of time. However, for the passive FePc thin film sensor, a model that accounts for a level of film saturation is of primary importance. Since the sensor possesses a thin film morphology that was not designed for reversibility, accounting for the differences between adsorption and desorption rates is also important. Construction of such a model can offer a theoretical basis for calibration and sensitivity analysis that can be applicable for any general passive sensing film. In this chapter a working model is developed and the model's predictions evaluated.

6.1 Conductivity model for FePc thin films

There is some uncertainty as to whether gas adsorption induced MPc thin film conductivity is predominately a surface or bulk process. Two models are presented in this section to describe surface and bulk conductivity. Each model takes into account the geometry of the interdigitated electrode pattern on each sensor. These models provide a means by which measured sensor resistance values can be converted to actual FePc film conductivity values. The predicted conductivity values will be compared to known values for MPc thin films in order to determine which conductive mechanism is more plausible.

The bulk conductivity model treats the FePc thin film as a bulk conducting film and obtains conductivity from the inverse of bulk resistivity. The surface conductivity model assumes surface conductivity as the only conductive mechanism and models the FePc film between electrodes as a multitude of parallel conducting pathways along the surface. Because electrical conductivity occurs across an interdigitated sensor electrode pattern, it is necessary to account for the physical geometry of the electrodes. Thus both models incorporate the electrode geometry used in this research. The sensor electrode geometry is presented in Figure 6.1. The relevant variables and dimensional values are defined as follows:

σ_b = Film bulk conductivity

σ_s = Film surface conductivity

J = Current density

E = Electric field

I = Current flow

A = Total cross sectional area

V = Voltage

R = Resistance

d = Electrode gap spacing = 15 x 10^{-6} m

n = Number of electrode fingers = 25

l = Length of electrode fingers = 2.97 x 10^{-3} m

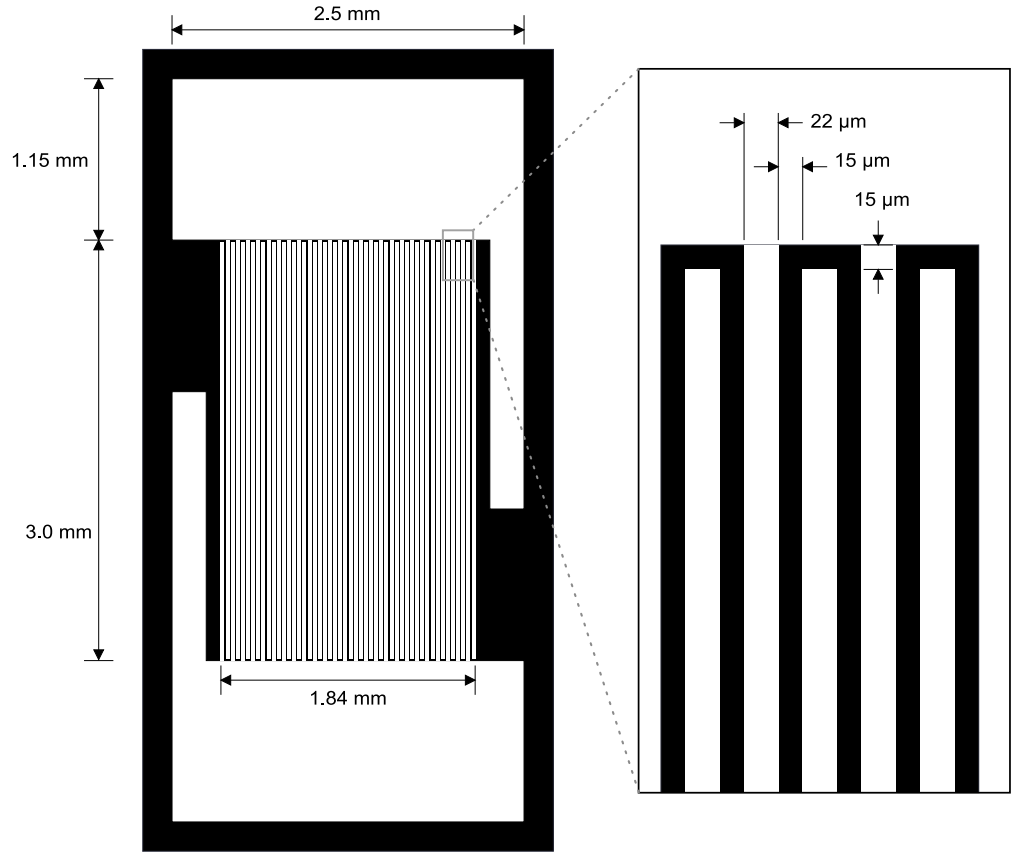

Figure 6.1: Sensor inter-digitated electrode pattern consists of two main electrode contacts for interface with measurement circuitry. The two main electrodes branch into 25 pairs of parallel electrode fingers with a constant 15 micron gap in between fingers.

e = Width of electrode fingers = 22 x 10^{-6} m

h = Height of thin film

6.1.1 Bulk conductivity model

Bulk conductivity is quantified by the current flow through a cross sectional area due to an electric field:

$$\sigma_b = \frac{J}{E} = \frac{I/A}{V/d} = \frac{Id}{VA} = \frac{d}{RA} \tag{6.1}$$

With reference to the sensor design diagrammed in Figure 6.1, the cumulative cross sectional area between the electrode fingers can be expressed as:

$$A = (2n-1)lh + 2neh \tag{6.2}$$

Substituting Equation 6.2 into Equation 6.1 yields the equation for bulk conductivity:

$$\sigma_b = \frac{d}{R}\left[\frac{1}{(2n-1)lh + 2neh}\right] \tag{6.3}$$

6.1.2 Surface conductivity model

The surface conductivity model treats the continuous FePc thin film between the interdigitated electrodes as a series of parallel resistors. With this treatment, the surface conductivity equation is expressed in Equation 6.5

$$\frac{1}{R} = \sum_{1}^{\frac{(2n-1)l+2ne}{d}} \frac{1}{R_s} = \frac{(2n-1)l + 2ne}{R_s d} \tag{6.4}$$

$$\sigma_s = \frac{1}{R_s} = \frac{d}{R\left[(2n-1)l + 2ne\right]} \tag{6.5}$$

6.1.3 Model comparisons

To compare which model more adequately describes the conductivity of the FePc thin film sensor, intrinsic resistance values from a temperature cycle experiment were converted to conductivity using each model. Figure 6.2 shows the plot of conductivity values as a function of temperature for each model. The FePc film thickness of the sensor was 450 nm. Due to the thickess of the FePc film, a rough, grainy surface morphology with a high surface area to bulk ratio is expected.

From the figure, the surface conductivity model predicts intrinsic values ranging from 9.51 x 10^{-15} Ω^{-1} at -50 °C to 8.75 x 10^{-12} Ω^{-1} at 70 °C. For the bulk conductivity model,

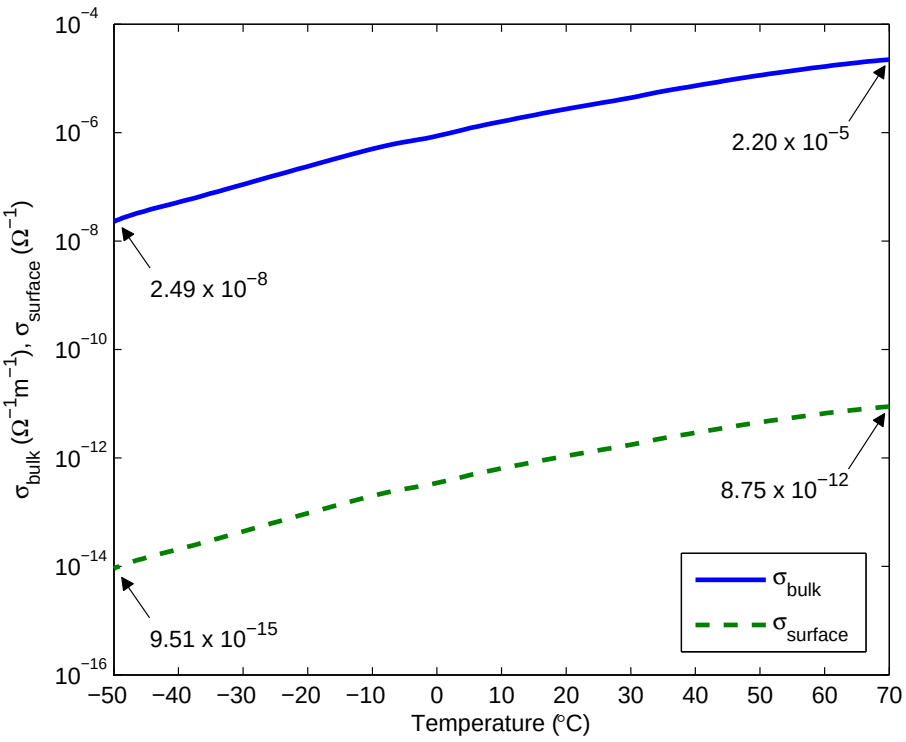

Figure 6.2: Plot of conductivity values obtained from the bulk and surface conductivity models for a 450 nm FePc sensor, under nitrogen gas in the temperature range of -50 to 70 °C. The bulk conductivity levels range from 2.49 x 10^{-8} to 2.2 x 10^{-5} $\Omega^{-1}m^{-1}$, while the surface conductivity levels range from 9.51 x 10^{-15} to 8.75 x 10^{-12} Ω^{-1}.

intrinsic conductivity values range from 2.49 x 10^{-8} $\Omega^{-1}m^{-1}$ at -50 °C to 2.2 x 10^{-5} $\Omega^{-1}m^{-1}$ at 70 °C. The conductivity values from each model are compared in Table 6.1 along with reference values for other MPc films.

Table 6.1: Measured conductivity values for various MPcs

Phthalocyanine	Condition	Conductivity	Reference
MnPc	Vacuum	7.14 x 10^{-5} $\Omega^{-1}m^{-1}$	[2]
CoPc	Vacuum	1.11 x 10^{-8} $\Omega^{-1}m^{-1}$	[2]
	2.8 ppb NO_2	1.0 x 10^{-7} Ω^{-1}	[3]
	44 ppb NO_2	1.8 x 10^{-7} Ω^{-1}	[3]
NiPc	Vacuum	1.00 x 10^{-8} $\Omega^{-1}m^{-1}$	[2]
	2.8 ppb NO_2	4.2 x 10^{-9} Ω^{-1}	[3]
	44 ppb NO_2	8.6 x 10^{-9} Ω^{-1}	[3]
CuPc	Vacuum	8.33 x 10^{-9} $\Omega^{-1}m^{-1}$	[2]
	2.8 ppb NO_2	2.4 x 10^{-8} Ω^{-1}	[3]
	44 ppb NO_2	8.4 x 10^{-8} Ω^{-1}	[3]
FePc (Bulk)*	N_2 at 70°C	2.2 x 10^{-5} $\Omega^{-1}m^{-1}$	-
	N_2 at -50°C	2.49 x 10^{-8} $\Omega^{-1}m^{-1}$	-
FePc (Surface)*	N_2 at 70°C	8.75 x 10^{-12} Ω^{-1}	-
	N_2 at -50°C	9.51 x 10^{-15} Ω^{-1}	-

* From experimental resistance values converted with presented models.

Although some previous research have suggested surface conductivity as the conductive mechanism of MPc thin films, it is reasonable to observe that due to the rough morphology of polycrystalline α-FePc films, the actual conductive mechanism may be more of a combination of both bulk and surface effects, and that the two models each apply to two different extremes in film morphology. The surface conductivity model can be applied to perfectly smooth, single crystal, or monolayer type MPc films, where conductivity occurs strictly on the surface because permeation of doping agents into the bulk is not possible. Meanwhile the bulk conductivity model applies to very rough polycrystalline films with many defects and trap sites, where charge carriers are liberated to form conducting pathways all along the thickness of the film. Due to the FePc thin film morphology of sensors observed under SEM, particularly for the 250-450 nm films, the conductive mechanism described by the

bulk conductivity model will be assumed for this research. Comparison of bulk conductivity values with other MPc conductivity values in Table 6.1 support this assumption.

6.2 Response model for passive FePc sensor

The kinetics of gas adsorption and desorption on FePc thin films forms the basis of modeling passive sensor reponse. The interaction of nitrogen dioxide gas molecules with FePc thin films can be described by an electron donor-acceptor mechanism, where free electrons in the FePc molecule participate in π-bonding with adsorbed nitrogen dioxide gas molecules. The resulting complex creates hole charge carriers within the FePc bulk that can be mobilized under the application of an electric field [4, 3, 5, 6]. Based on the principles of chemical equilibrium and chemical activity, a simple model for surface coverage as a function of gas concentration, adsorption rate, desorption rate, and time can be derived. Once the gas adsorption and desorption kinetics is modeled, modifying the model to predict the induced conductivity change on MPc thin films is possible. This relies on finding the underlying relationship between surface coverage (or surface concentration) and film conductivity. As this relationship is established, the model for gas adsorption-desorption kinetics can be used to predict film conductivity as a function of time or concentration. Some researchers suggest a proportional relationship between surface coverage and film conductivity while others suggest a higher order power relationship [7, 8]. Both relationships shall be considered and investigated. With this, the derivation of the sensor response model is presented.

6.2.1 Derivation of model

The basic chemical reaction for chemical adsorption and desorption of nitrogen dioxide gas onto FePc thin films is as follows:

$$NO_{2(g)} + FePc_{(s)} \rightleftharpoons NO_2FePc_{(s)} \tag{6.6}$$

The major assumptions made for this model are:

1. Adsorption only occurs at the surface; no diffusion into the bulk is considered.
2. All adsorption sites have identical energy; only one type of adsorption site exists.

3. Film conductivity varies with the surface coverage.

Variable definitions:

N_o = Total number of adsorption sites

N_s = Number of occupied sites

k_a = Adsorption rate constant

k_d = Desorption rate constant

C_o = Analyte gas concentration

θ = Surface coverage ($\frac{N_s}{N_o}$)

I = Film conductivity

I_{ss} = Steady state film conductivity

k_i = Proportionality constant relating surface coverage to film conductivity ($I = k_i\theta$)

S = Power constant relating surface coverage to film conductivity ($I = \theta^S$)

R = Sensor resistance

R_o = Sensor initial resistance

$R_s s$ = Sensor saturation resistance

The governing equation for this sensor response model was adopted from the work of Low, who performed extensive investigation into the kinetics of chemisorption of gases on solids [9]. This governing equation describes a simple site balance, stating that the change in number of occupied sites with respect to time is equivalent to the number of analyte molecules undergoing absorption minus the number of analyte molecules undergoing desorption:

$$\frac{\mathrm{d}N_s}{\mathrm{d}t} = k_a C_o(N_o - N_s) - k_d N_s \tag{6.7}$$

Recognizing that the surface coverage is simply the fraction of occupied sites to total number of sites, dividing Equation 6.7 by the total number of sites yields the differential change in surface coverage with respect to time.

$$\frac{\mathrm{d}\theta}{\mathrm{d}t} = k_a C_o(1-\theta) - k_d\theta \tag{6.8}$$

By separating the variables and integrating both sides, the general surface coverage equation is thus arrived at in Equation 6.12:

$$\frac{\mathrm{d}\theta}{\left(\frac{k_a C_o}{k_a C_o + k_d}\right) - \theta} = (k_a C_o + k_d)\mathrm{d}t \tag{6.9}$$

$$\int \frac{1}{\alpha - \theta}\,\mathrm{d}\theta = \int \beta\,\mathrm{d}t \quad , \quad \alpha = \frac{k_a C_o}{k_a C_o + k_d} \quad , \quad \beta = k_a C_o + k_d \tag{6.10}$$

$$-\ln(\alpha - \theta) + c = \beta t \tag{6.11}$$

$$\theta = \alpha - e^{(-\beta t - c)} \tag{6.12}$$

A. Proportional relationship between conductivity and surface coverage

For the assumption that film conductivity is proportional to the surface coverage, a proportionality constant k_i can be introduced to obtain conductivity:

$$I \propto \theta \tag{6.13}$$

$$I = k_i\theta = k_i\left[\alpha - e^{(-\beta t - c)}\right] \tag{6.14}$$

Since sensor output is resistance and resistance has an inverse relationship to conductivity ($R = 1/I$), this equation can be rewritten as:

$$R = \frac{1}{k_i\left[\alpha - e^{(-\beta t - c)}\right]} \tag{6.15}$$

The initial boundary condition where $R = R_o$ when $t = 0$ can be applied to determine the constant c:

$$R_o = \frac{1}{k_i\left(\alpha - e^{-c}\right)} \quad , \quad c = -\ln\left(\alpha - \frac{1}{R_o k_i}\right) \tag{6.16}$$

Similarly, the steady state boundary condition where $R \to R_{ss}$ as $t \to \infty$ can be applied to resolve the constant α:

$$R_{ss} = \frac{1}{k_i \alpha} \tag{6.17}$$

Substitution of the boundary condition results back into Equation 6.15 yields the final form of this sensor response model:

$$R = \frac{1}{\frac{1}{R_{ss}} - \left(\frac{1}{R_{ss}} - \frac{1}{R_o}\right) e^{(-\beta t)}} \tag{6.18}$$

A reorganized form of Equation 6.18 can be more useful for analysis:

$$-\beta t = \ln\left(\frac{1 - \frac{R_{ss}}{R}}{1 - \frac{R_{ss}}{R_o}}\right) \tag{6.19}$$

The resulting Equations 6.18 and 6.19 describe the resistance response of a FePc thin film sensor over time as it is exposed to nitrogen dioxide gas of a certain concentration, with the assumption that a proportional relationship exists between film conductivity and surface coverage. (Note that in these equations $\beta = k_a C_o + k_d$.)

B. Power relationship between conductivity and surface coverage

Assuming that film conductivity follows a power relationship relative to the surface coverage, a power constant S can be introduced to obtain conductivity:

$$I \propto \theta^S \tag{6.20}$$

$$I = k_i \theta^S = k_i \left[\alpha - e^{(-\beta t - c)}\right]^S \tag{6.21}$$

Since sensor output is resistance and resistance has an inverse relationship to conductivity ($R = 1/I$), this equation can be rewritten as:

$$R = \frac{1}{k_i \left[\alpha - e^{(-\beta t - c)}\right]^S} \tag{6.22}$$

The initial boundary condition where $R = R_o$ when $t = 0$ can be applied to determine the constant c:

$$R_o = \frac{1}{k_i \left[\alpha - e^{-c}\right]^S} \quad , \quad c = -\ln\left[\alpha - \left(\frac{1}{k_i R_o}\right)^{\frac{1}{S}}\right] \tag{6.23}$$

Similarly, the steady state boundary condition where $R \to R_{ss}$ as $t \to \infty$ can be applied to resolve the constant α:

$$\alpha = \left(\frac{1}{k_i R_{ss}}\right)^{\frac{1}{S}} \tag{6.24}$$

Substitution of the boundary condition results back into Equation 6.22 yields the final form of this sensor response model:

$$R = \frac{1}{\left[\left(\frac{1}{R_{ss}}\right)^{\frac{1}{S}} - \left[\left(\frac{1}{R_{ss}}\right)^{\frac{1}{S}} - \left(\frac{1}{R_o}\right)^{\frac{1}{S}}\right] e^{(-\beta t)}\right]^S} \tag{6.25}$$

A reorganized form of Equation 6.25 can be more useful for analysis:

$$-\beta t = \ln\left(\frac{1 - \left(\frac{R_{ss}}{R}\right)^{\frac{1}{S}}}{1 - \left(\frac{R_{ss}}{R_o}\right)^{\frac{1}{S}}}\right) \tag{6.26}$$

The resulting Equations 6.25 and 6.26 describe the resistance response of a FePc thin film sensor over time as it is exposed to nitrogen dioxide gas of a certain concentration, with the assumption that a power relationship exists between film conductivity and surface coverage. (As before, note that in these equations $\beta = k_a C_o + k_d$.)

6.2.2 Theoretical predictions and dependencies

The response models presented in the previous section can be used to predict the theoretical resistance response for FePc thin film sensors. For the assumption that a proportional relationship exists between conductivity and surface coverage, Figure 6.3 details the concentration dependency of the response curve based on Equation 6.18. Values for the various constants have been arbitrarily assigned as follows: $R_o = 1$ x 10^8 Ω, $R_{ss} = 3$ x 10^3 Ω, $k_a = 15$, $k_d = 5$ x 10^{-6}. Note that the proportionality constant k_i no longer exists because the steady state resistance R_{ss} has been assigned a value. From the figure, as concentration increases from 0.5 to 100 ppm, the theoretical response curves become sharper and less gradual. It is worth noting that in the first two minutes, the resistance response curves for the various concentrations are virtually indistinguishable from each other, as resistance drops rapidly from 1 x 10^8 to 1 x 10^6 Ω. It is only until after five minutes of exposure that the magnitude and rate of resistance change becomes distinguishable for the various concentrations.

For the assumption that a power relationship exists between conductivity and surface coverage, Figure 6.4 shows the concentration dependency of the response curve for a fixed $S = 5$, and Figure 6.5 describes how the response curve evolves with the power law constant S for a fixed concentration of 25 ppm. Both figures are based on Equation 6.25. Values for the various constants have been arbitrarily assigned as before: $R_o = 1$ x 10^8 Ω, $R_{ss} = 3$ x 10^3 Ω, $k_a = 15$, $k_d = 5$ x 10^{-6}. From Figure 6.5, like in the proportional case, the theoretical response curves become sharper and less gradual as concentration is increased from 0.5 to 100 ppm. However in this case, the rate of change in resistance is immediately differentiable between the various concentrations at the moment of exposure. This is due to the power law relationship between film conductivity and surface coverage. To investigate the dependency of sensor response on the power law constant S, Figure 6.5 shows response curves for a range of S under a fixed concentration of 25 ppm. Observing Equation 6.25, the dependency on S is such that as S increases, the response curve becomes more gradual. However, as S

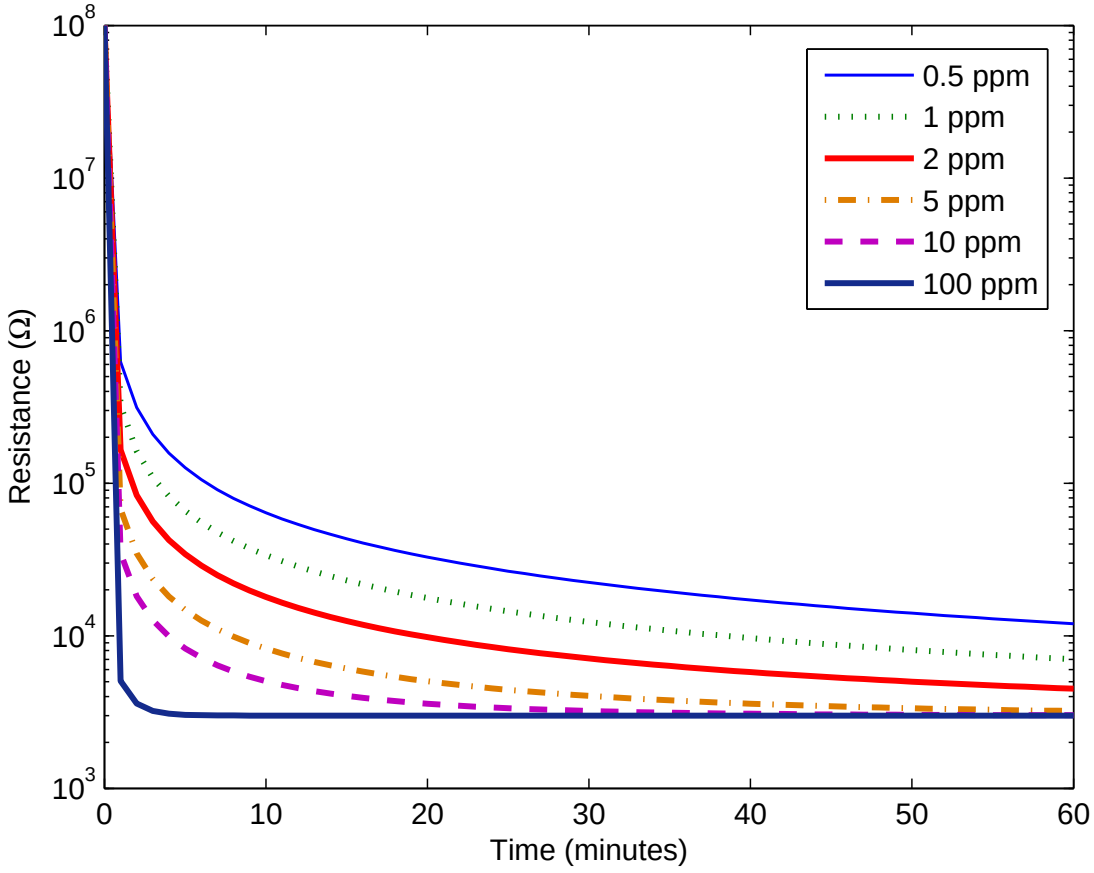

Figure 6.3: For the proportional conductivity versus surface coverage model, as concentration increases from 0.5 to 100 ppm, the theoretical response curves become sharper and less gradual as expected due to the higher concentrations of analyte gas. For the first two minutes, the resistance response curves for the various concentrations are nearly identical from each other, as resistance drops rapidly from 1 x 10^8 to 1 x 10^6 Ω. It is only until after five minutes of exposure that the magnitude and rate of resistance change becomes distinguishable across the various concentrations.

increases above 10, the response curves rapidly converge. Further increasing S above 100 does not significantly affect the response curve.

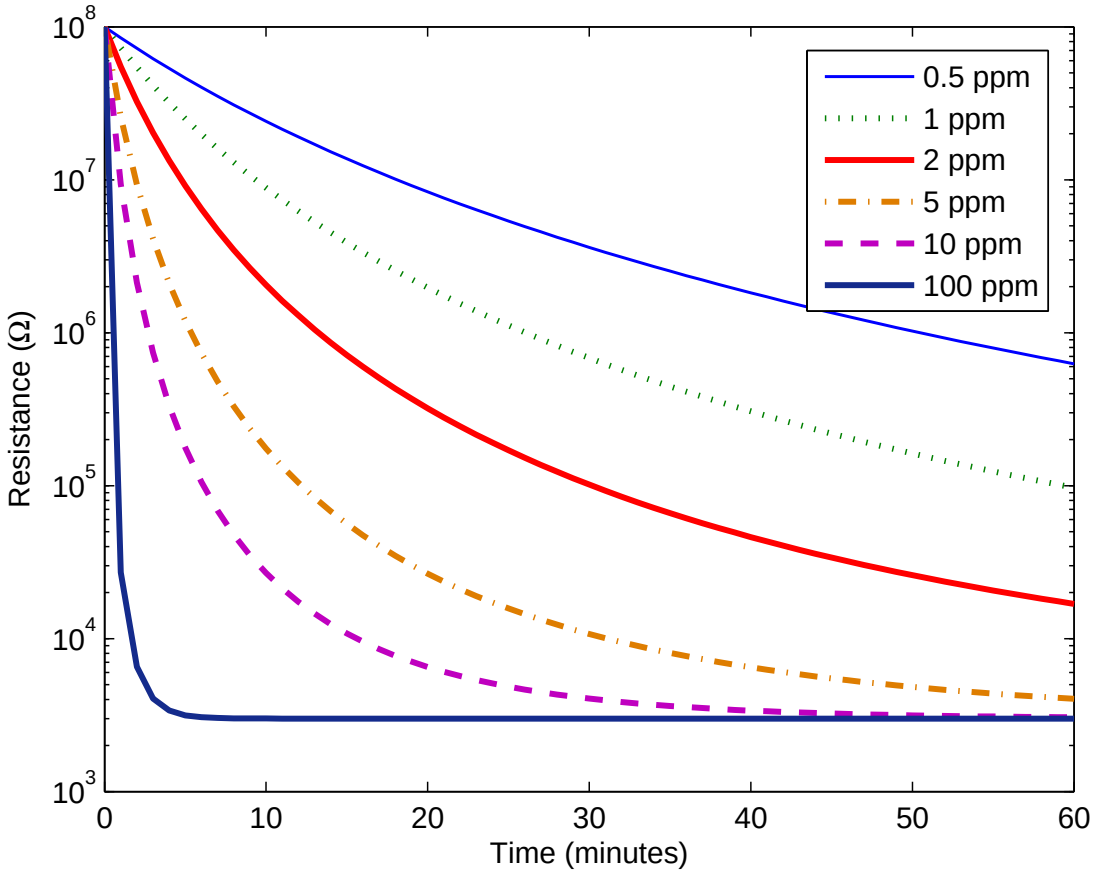

Figure 6.4: For the power law conductivity versus surface coverage model, as concentration increases from 0.5 to 100 ppm, the theoretical response curves become sharper and less gradual as expected. However in this case, the rate of change in resistance is immediately differentiable between the various concentrations at the moment of exposure.

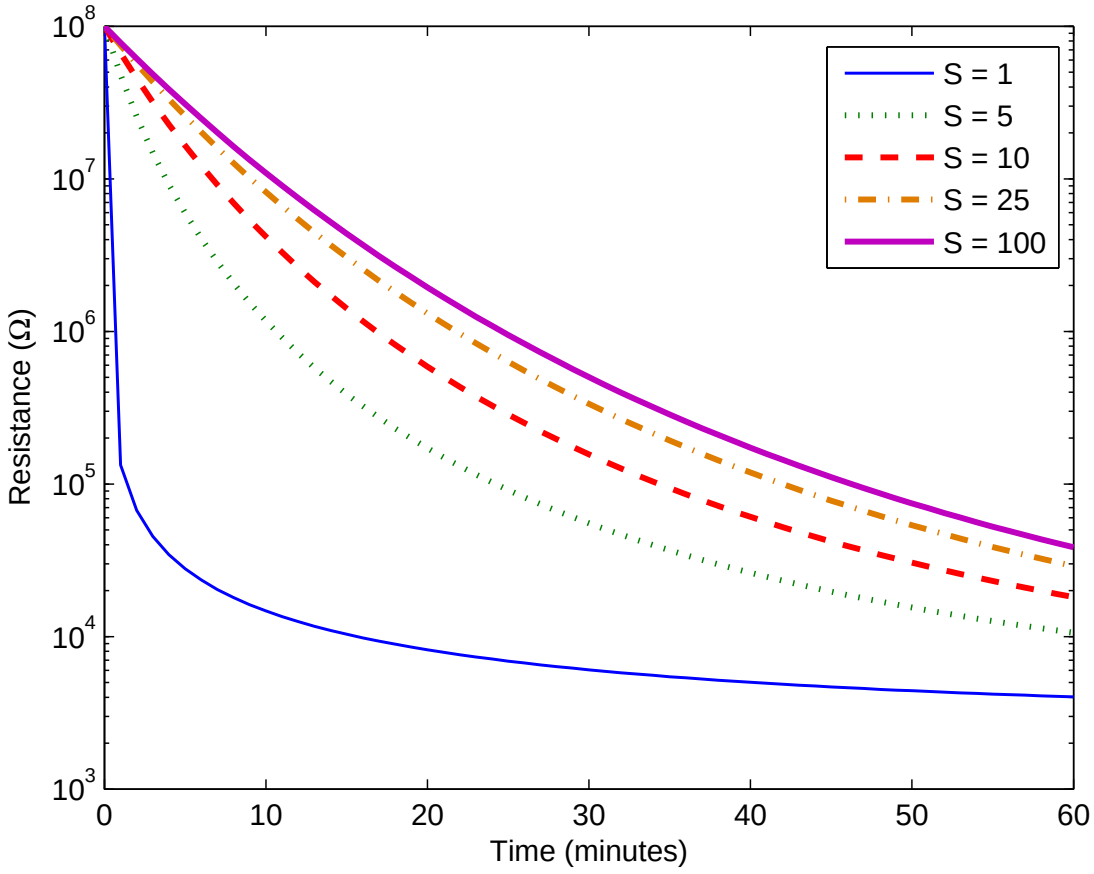

Figure 6.5: For the power law conductivity versus surface coverage model, as the power law constant S is increased, the response curve becomes more gradual, and shows a longer time to saturate. As S increases above 10, the response curves rapidly converge. Further increasing S above 100 does not significantly affect the response curve.

6.2.3 Sensor calibration method

A further application of the sensor response model presented in this research is the determination of a calibration equation. Assuming power law conductivity, an equation can be derived to express a generalized resistance change as a function of analyte gas concentration. For simplicity, variable γ is introduced to represent the dimensionless generalized resistance.

$$\gamma(R) = \ln\left(\frac{1-\left(\frac{R_{ss}}{R}\right)^{\frac{1}{S}}}{1-\left(\frac{R_{ss}}{R_o}\right)^{\frac{1}{S}}}\right) \tag{6.27}$$

Equation 6.26 can thus be rewritten as:

$$\gamma = -(k_a C_o + k_d)t \tag{6.28}$$

Taking the generalized resistance change and dividing it by exposure duration results in the calibration equation:

$$\gamma(R_2) - \gamma(R_1) = \Delta\gamma = -(k_a C_o + k_d)\Delta t \tag{6.29}$$

$$\frac{\Delta\gamma}{\Delta t} = -k_a C_o + k_d \tag{6.30}$$

Equation 6.30 is the calibration equation stating that the generalized resistance change over time is a linear function of analyte gas concentration, with a slope equivalent to the adsorption rate constant and the intercept equal to the desorption rate constant. Since the sensor initial resistance and saturation resistance values can be experimentally determined and vary little within the same batch of vacuum sublimed FePc films, and that the values for adsorption rate, desorption rate, and power law constant remain consistent for a particular FePc thin film, this calibration model becomes useful for evaluating passive sensor response.

6.3 Application of sensor response model

The response models presented in this research can be applied towards an experimental resistance response of a FePc thin film sensor, to evaluate its applicability to actual experimental data, and also to obtain values for the unknown constants. In order to achieve these objectives, curve fits were applied to recorded sensor response data obtained from a nitrogen dioxide saturation experiment. Figure 6.6 shows the plot of two 450 nm FePc sensors exposed to 100 ppm nitrogen dioxide until saturation is reached. In the figure, the dotted line is a curve fit based on the assumption that the conductivity varies proportionally with surface coverage (Equation 6.18), while the solid line is a curve fit based on the assumption that the conductivity follows a power relationship with surface coverage (Equation 6.25).

For both curve fits, sensor initial and saturation resistance values were obtained from experimental maximum and minimum resistance readings of 2 x 10^7 Ω and 3.5 x 10^3 Ω respectively. Since the curve fit variable β is a function of the analyte gas concentration as well as the adsorption and desorption rate constants ($\beta = k_a C_o + k_d$), the same value for β was enforced for both curve fits. Least squares fitting yielded the values $\beta = 4.59$ and power law constant $S = 4.8$. From the figure, the model with the power relationship assumption between conductivity and surface coverage more closely describes the experimental resistance response. The model that assumes proportional conductivity change predicts a trend that reaches saturation faster than actual data suggests. The result is that the gas adsorption-desorption induced conductivity change in a rough, polycrystalline α FePc thin film follows the more complex power law mechanism.

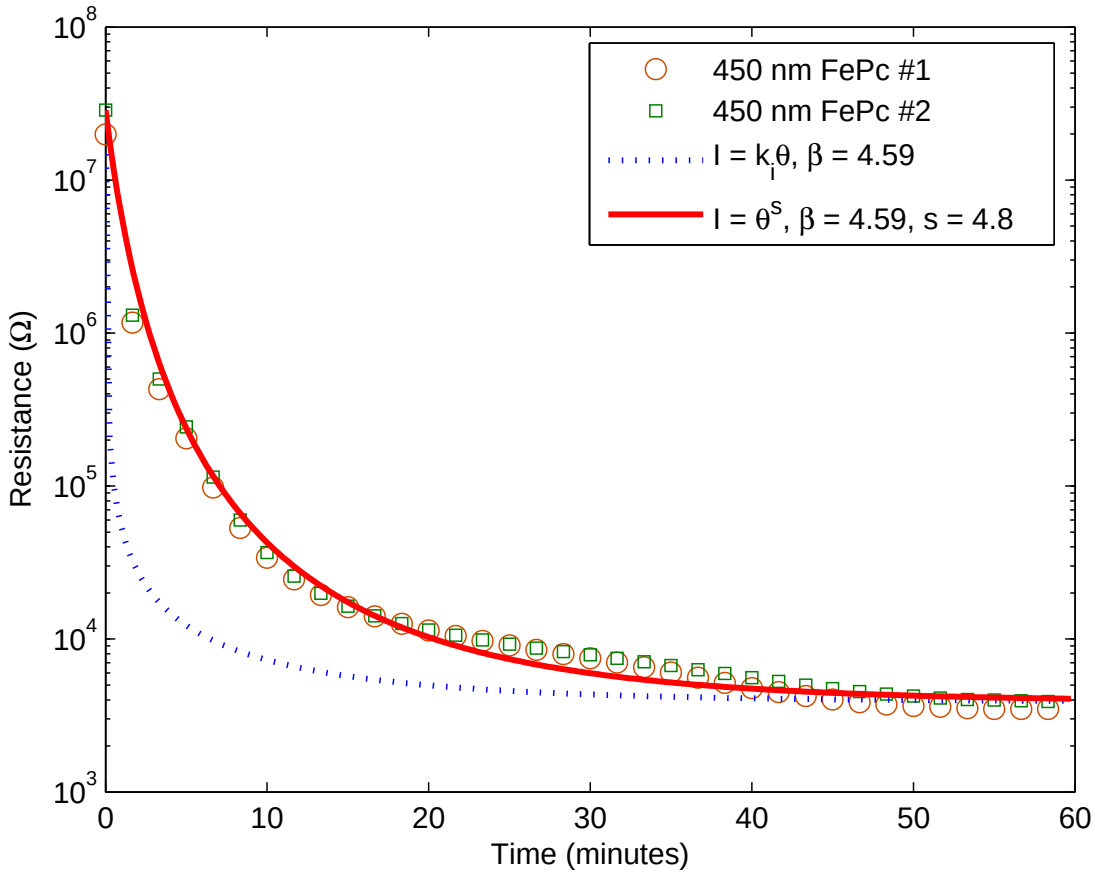

Figure 6.6: Two 450 nm FePc sensors are exposed to 100 ppm nitrogen dioxide until saturation is reached. Their resistance response are indicated by the discrete data points. The dotted line is a curve fit based on Equation 6.18 while the solid line is a curve fit based on Equation 6.25.

6.4 Sensor calibration and performance

The evaluation of sensor performance parameters for passive sensing with FePc thin films is made possible by the application of the passive sensing model and the sensor calibration method presented in this work. Parameters such as sensitivity and limit of detection can be determined by gathering experimental data for use with the calibration method. For that purpose, an experiment was performed to obtain sensor response data to various concentrations of nitrogen dioxide.

In this experiment, two 150 nm, two 250 nm, and two 450 nm FePc thin film sensors based on silicon dioxide substrates were subjected to nitrogen dioxide gas concentrations in an increasing and decreasing order, from 0.1 ppm up to 2 ppm and back to 0.1 ppm at 20 °C. This concentration ramp profile was designed to test sensor response to actual sensing conditions at around the nitrogen dioxide gas exposure limit of 1 ppm. For each concentration, sensors were exposed to two and a half minutes of nitrogen dioxide gas followed by another two and a half minutes of ultra high purity nitrogen gas. Figure 6.7 shows the nitrogen dioxide exposure timeline for this experiment. Figure 6.8 shows the resistance response of all six sensors. The Kin-Tek gas generator provides different concentrations of nitrogen dioxide gas by varying the dilution flow rate, thus the overall flow rate varies from concentration to concentration. For reference, the volumetric flow rates for each nitrogen dioxide concentration step are listed in Table 6.2. The flow rates for each nitrogen purge step are held at a constant 0.25 L/min.

From the resistance response data shown in Figure 6.8, a calibration plot based on Equation 6.30 can be produced. Since the sensor response characteristics are similar between the initial increasing concentration stage and latter decreasing concentration stage, to demonstrate the usability of the passive sensing model at more saturated conditions, only data from the latter stage is used for the calibration plot. To convert resistance measurements to generalized resistance change, a power law relationship was assumed with the constant $S = 4.8$ adopted from the curve fit of a saturated sensor response in Figure 6.6. Figure 6.9 shows the resulting calibration plot. As described by the calibration equation, a linear

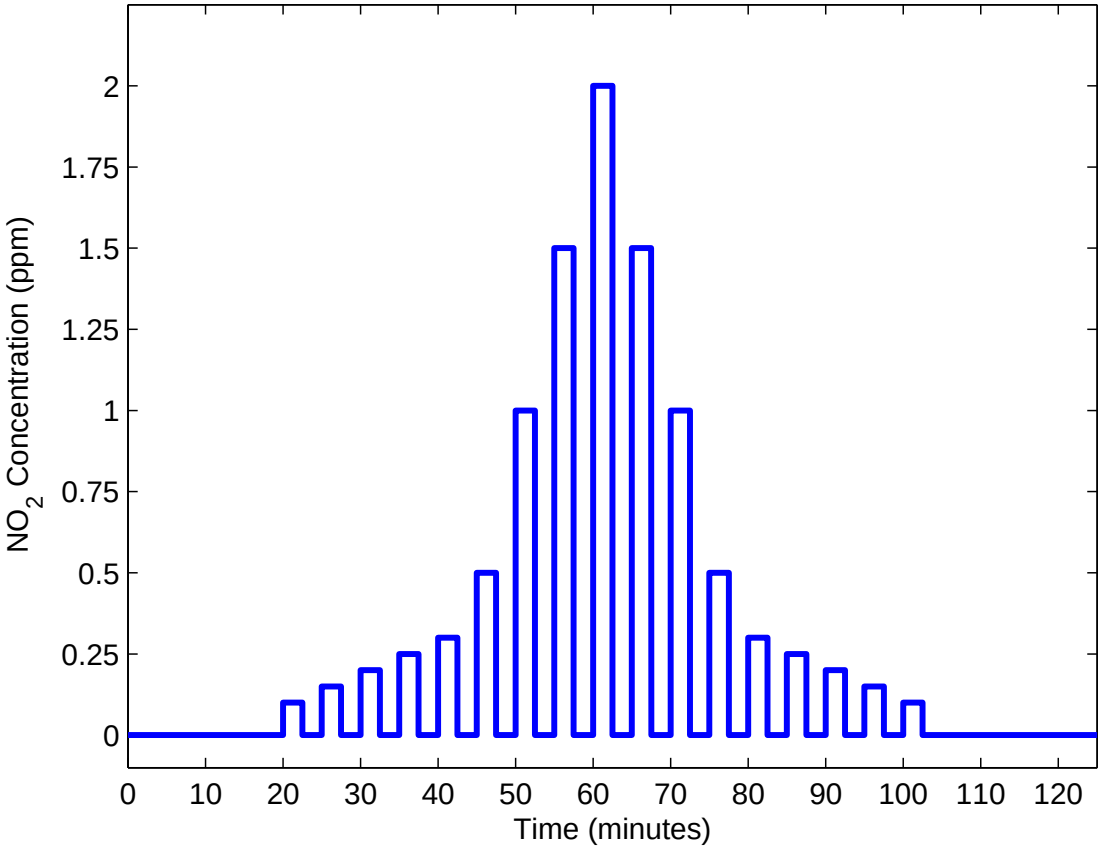

Figure 6.7: The nitrogen dioxide concentration ramp test profile consists of a series of increasing concentration steps followed by a series of decreasing concentration steps. Each concentration step includes two and a half minutes of nitrogen dioxide exposure followed by a nitrogen purge of equal duration. This concentration ramp profile was designed to test sensor response to actual sensing conditions at around the nitrogen dioxide gas exposure limit of 1 ppm.

Table 6.2: Nitrogen dioxide flow rate vs. concentration

Concentration (ppmv)	Volumetric flow rate (L/min)
0.1	4.81
0.15	3.20
0.20	2.40
0.25	1.92
0.3	1.60
0.5	0.96
1	0.48
1.5	0.32
2	0.24

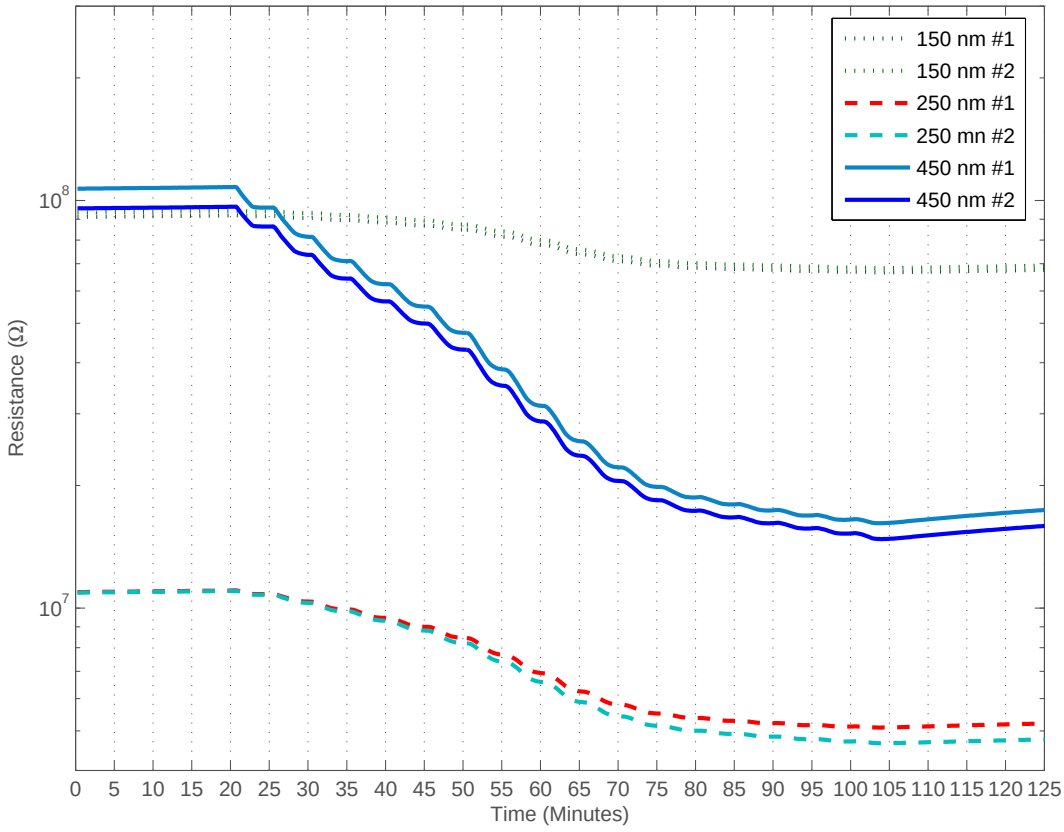

Figure 6.8: Sensor response to the nitrogen dioxide concentration ramp test shows the resistance change of all six sensors versus time. Initially, the rate of resistance decrease for each exposure correlates strongly with the concentration of ambient nitrogen dioxide gas, yet as the sensor gradually approaches saturation, this correlation loses effect. The passive sensing model presented in this research was developed to address this issue by taking into account the saturation state of FePc thin films.

trend is observed between generalized resistance change and concentration. The solid lines in the figure represent curve fits for the first sensor of each thickness. The curve fits yield adsorption rate constants of 2.789, 11.37, and 16.15 as well as desorption rate constants of 4.533 x 10^{-7}, 3.344 x 10^{-6}, and 1.003 x 10^{-5} for film thicknesses of 150, 250, and 450 nm respectively. From this calibration plot, since sensor sensitivity is by definition the slope of the linear region, the adsorption rate constant is effectively the sensitivity of the sensor. In general MPc thin film sensor applications, thinner films typically provide better gas sensitivity due to its responsiveness and high surface to bulk ratio. Yet for the passive sensing case, thinner films may saturate too quickly to low doses of analyte concentrations as observed in Figure 6.8. As for film desorption rates, analysis yields adsorption to desorption rate ratios of 1.63 x 10^{-7}, 2.94 x 10^{-7}, and 6.21 x 10^{-7} for the 150, 250, and 450 nm films respectively. Thus for passive sensing, not only do the thicker 450 nm FePc films possess higher adsorption rates for better sensitivity, its greater ablility to retain adsorbed analyte and prevent it from undergoing desorption makes it more ideal for passive sensing.

The passive sensing capabilities of FePc thin film sensors may not make sense if the sensor was unable to detect meaningful levels of nitrogen dioxide. As outlined in the objectives of this research, a passive FePc thin film sensor should detect nitrogen dioxide levels at or near 1 ppm as this level has been set forth as the maximum permissible exposure limit over a typical work day. To evaluate lower limit of detection, the calibration plot was redrawn on log-log scaled axes in Figure 6.10. This scaling allows inspection of the lower concentration data points. By definition, the lower limit of detection of a sensor is the lowest concentration at which the response departs linearity, where a further decrease in concentration fails to impart a proportional decrease in signal. From Figure 6.10, it is determined that 0.3 ppm nitrogen dioxide is the concentration below which this occurs, thus 0.3 ppm is established as the minimum reliable detection limit for passive FePc sensors of 150, 250, and 450 nm in film thickness.

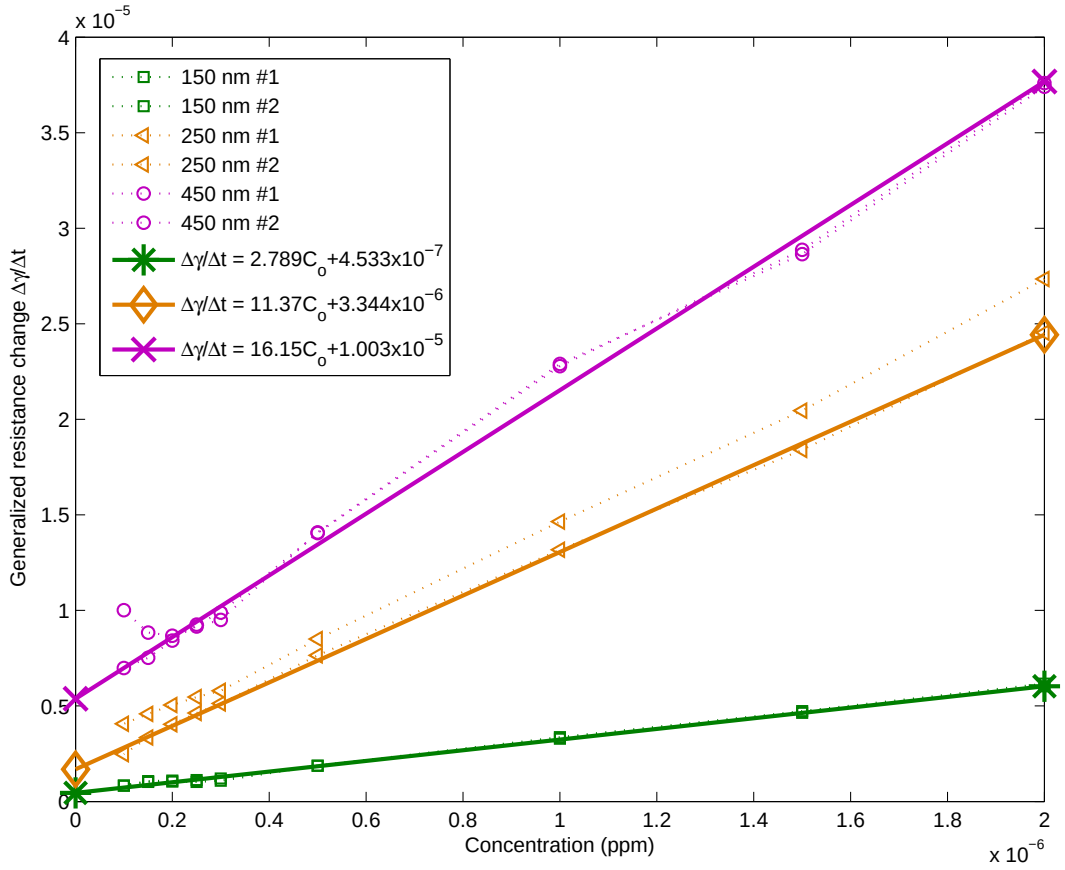

Figure 6.9: A calibration plot for 150, 250, and 450 nm FePc thin film sensors shows the expected linear relationship between the change in generalized resistance and nitrogen dioxide gas concentration. The discrete data points represent generalized resistance changes due to exposure to specific gas concentrations. The solid lines represent curve fits on the first sensor for each thickness using Equation 6.30. The curve fits yield adsorption rate constants of 2.789, 11.37, and 16.15 as well as desorption rate constants of 4.533 x 10^{-7}, 3.344 x 10^{-6}, and 1.003 x 10^{-5} for film thicknesses of 150, 250, and 450 nm respectively. These results quantitatively illustrate the trend that thicker films possess greater adsorption rate constants which result in improved sensitivity in a passive sensing scenario.

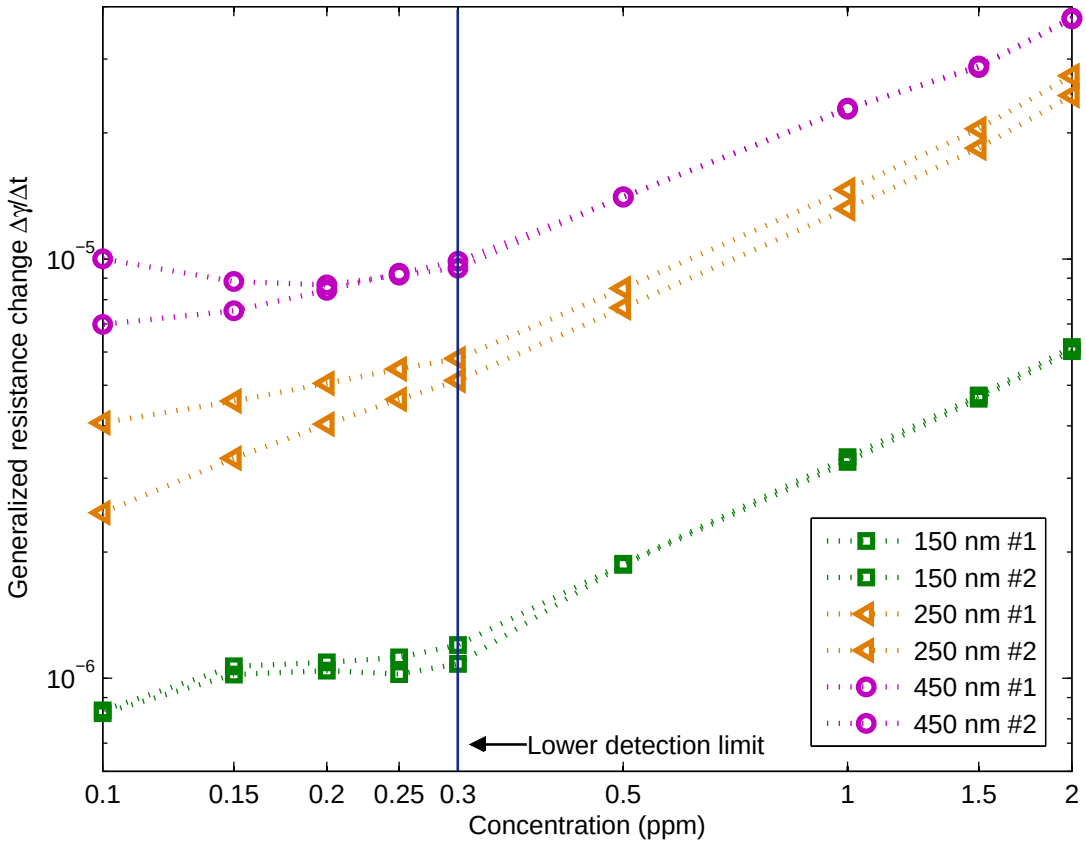

Figure 6.10: The lower limit of detection of 150, 250, and 450 nm FePc thin film sensors can be determined from a log-log scaled calibration plot. By definition, the lower limit of detection of a sensor is the lowest concentration at which the response departs linearity. It can be observed that the change in generalized resistance loses its linear relationship with concentration in at roughly 0.3 ppm for all three film thicknesses. Thus it is determined that 0.3 ppm forms the minimum reliable detection limit for passive sensors 150, 250, and 450 nm in thickness.

In conclusion, the passive sensing model presented in this work can successfully model sensor response, provided that the initial and saturation resistance levels of FePc thin films can be experimentally determined. The power relationship between surface coverage and conductivity change in FePc thin films seems to hold true, primarily due to the complexity of the rough surface morphology which affects the kinetics of gas adsorption and desorption and ultimately the film conductivity in a higher order manner. The key model parameters determined from the curve fitting of saturated and calibrated sensors are documented in Table 6.3. In summary, passive, integrating type sensors may lack an intuitive response characteristic that is easily linked to concentration, but using the calibration model presented here, it is possible to integrate data acquisition with the calibration algorithm and obtain reasonable and reliable estimates on nitrogen dioxide concentrations as low as 0.3 ppm.

Table 6.3: Sensor parameters determined from calibration model

	FePc sensor film thickness		
Parameter	150 nm	250 nm	450 nm
Sensitivity (k_a)	2.789	11.37	16.15
Intercept (k_d)	4.533 x 10^{-7}	3.344 x 10^{-6}	1.003 x 10^{-5}
Power law (S)	4.8		
Lower limit of detection (ppm)	0.3		

References

[1] I. Mclintock, "The elovich equation in chemisorption kinetics," *Letters to Nature*, vol. 216, pp. 1204–1205, 1967.

[2] D. D. Eley, "Studies of organic semiconductors for 40 years - the mobile pi-electron - 40 years on," *Molecular Crystals and Liquid Crystals Incorporating Nonlinear Optics*, vol. 171, pp. 1–21, 1989.

[3] T. Jones and B. Bott, "Gas-induced electrical conductivity changes in metal phthalocyanines," *Sensors and Actuators*, vol. 9, pp. 27–37, 1986.

[4] B. Bott and T. Jones, "A highly sensitive nitrogen dioxide sensor based on electrical conductivity changes in phthalocyanine films," *Sensors and Actuators*, vol. 5, pp. 43–53, 1984.

[5] R. L. V. Ewyk, A. V. Chadwick, and J. D. Wright, "Electron donor-acceptor interactions and surface semiconductivity in molecular crystals as a function of ambient gas," *J. C. S. Faraday Transactions I*, vol. 76, pp. 2194–2205, 1980.

[6] M. F. Craciun, S. Rogge, and A. F. Morpurgo, "Correlation between molecular orbitals and doping dependence of the electrical conductivity in electron-doped metal-phthalocyanine compounds," *Journal of the American Chemical Society*, vol. 127, pp. 12210–12211, 2005.

[7] C. J. Liu, J. C. Hsieh, and Y. H. Ju, "Response characteristics of lead phthalocyanine gas sensor - effect of operating temperature and postdeposition annealing," *Journal of Vacuum Science and Technology A*, vol. 14(3), pp. 753–756, 1996.

[8] K.-C. Ho and Y.-H. Tsou, "Chemiresistor-type no gas sensor based on nickel phthalocyanine thin films," *Sensors and Actuators B*, vol. 77, pp. 253–259, 2001.

[9] M. J. D. Low, "Kinetics of chemisorption of gases on solids," *Chemical Reviews*, vol. 60-3, pp. 267–312, 1960.

Chapter 7

Conclusions

In this research, a passive, chemical resistance based thin film FePc sensor was designed, fabricated, characterized, and tested. The object of this research was to investigate simple and long term monitoring of hazardous levels of nitrogen dioxide gas using passive FePc thin films. In summary, the major conclusions are:

1. FePc thin film sensors were manufactured via physical vapor deposition of FePc powder onto gold inter-digitated electrodes patterned on silicon dioxide and quartz substrates. Fabrication was performed using standard microelectronics fabrication techniques on whole wafers.

2. The general response of sensors showed two to four orders of magnitude change in resistance on exposure to 100 ppm nitrogen dioxide at 71, 20, and -46 °C, with sensor saturation occurring within 25 minutes of exposure. In these tests, nitrogen dioxide sensing for MPc based materials at sub-zero temperatures was successfully reported for the first time. It was found that the low temperatures in fact increased the overall sensor resistance change. Nitrogen dioxide gas adsorption by the FePc thin films was relatively unaffected by temperature.

3. Temperature dependence experiments were conducted over the temperature range of 71 to -46 °C for 450 nm sensors, under ultra-high purity nitrogen (0.1 L/min), and subsequently under nitrogen dioxide gas (100 ppm, 0.1 L/min), to investigate intrinsic and extrinsic conductivity levels respectively. The results showed that the FePc thin film conductivity dependence is described by the Arrhenius equation. The measured

activation energies of 0.76 and 0.30 eV for intrinsic and extrinsic conductivity compared well with reported values for other MPc thin films.

4. Concentration dependence experiments were performed at room temperature over the range of 0.5 to 2 ppm nitrogen dioxide. Sensor response showed that the change in relative resistance over time can be used to differentiate different concentrations in this range. However, this method can only apply for sensors with FePc thin films at relatively low saturation levels.

5. Specificity tests were conducted for the common atmospheric interferants ammonia, water vapor, and oxygen. Ammonia at the concentration of 100 ppm was able to cause de-doping of oxidizing species on the sensor. Thus ammonia can be used as a reversing or cleaning agent for FePc thin film sensors. Exposure to 95% relative humidity air and 99.8% were found not to affect the FePc thin film sensors.

6. Operational longevity tests were conducted using a temperature cycle of -50 to 80 °C under flowing nitrogen gas, with sensor resistance continuously monitored and recorded. Repetitive thermal cycling results indicate that FePc thin films possessed excellent stability under these conditions. The only notable change in resistance was due to the desorption of atmospheric oxygen, which occurred since the sensors were stored under air. All sensors were able to achieve stable equilibrium under the nitrogen environment within 3-7 cycles, upon which resistance levels became a strict function of temperature. Storage longevity tests indicate that sensor storage under a dry, dark or UV shielded, enclosed container can preserve sensor baseline resistance levels indefinitely.

7. To investigate the effects of sensor fabrication parameters, the film thickness, substrate type, and post-deposition heat treatment effects were analyzed. Under SEM, as film thickness increased from 50 to 450 nm, larger grains and greater surface roughness was observed. On n-type oxidized silicon, p-type oxidized silicon, and quartz substrate

types, FePc thin films showed similar morphology as well as similar sensor response. Post-deposition heat treatment results indicated that FePc thin films saturated faster when heat treated in the range of 20 to 190 °C. In general, as-deposited 450 nm α-FePc thin films without any heat treatment provided ideal passive sensor response characteristics. These sensors possessed the highest sensitivity to nitrogen dioxide concentrations (0.3-2 ppm), exhibited the largest order of magnitude change (2 x 10^7 to 3.5 x 10^3 Ω), showed good stability under thermal cycling and storage, and were not significantly affected by high humidity or high oxygen concentrations.

8. Theoretical models for surface and bulk conductivity were presented as methods to obtain film conductivity values from measured resistance, based on the sensor electrode geometry. Comparison with published MPc conductivity values suggest that the bulk conductivity assumption yields comparable intrinsic values of 2.2 x 10^{-5} and 2.49 x 10^{-8} $\Omega^{-1}m^{-1}$ at 80 and -50 °C respectively. These results indicate that for the rough microcrystalline morphologies of α-FePc thin films, the bulk conductivity model more adequately describes the actual conductive mechanism.

9. A theoretical model for passive sensor response was derived with reference to established equations on gas adsorption-desorption kinetics. Experimental sensor saturation data revealed that film conductivity follows a power law of surface coverage. The passive sensing model also predicts a linear, proportional relationship between normalized resistance change and analyte gas concentration, forming the basis for a calibration plot. Experimental sensor response to a concentration gradient showed that the model was able to provide excellent predictions for 150, 250, and 450 nm FePc sensors in response to various concentrations of nitrogen dioxide. The calibration plot indicated that the 450 nm FePc films possessed the best sensitivity for passive sensing, and that reliable detection of nitrogen dioxide gas concentrations around 1 ppm was achievable, with a lower limit of detection of 0.3 ppm.

In conclusion, a passive FePc thin film sensor for the detection of nitrogen dioxide gas was fabricated and demonstrated. The research presented in this dissertation is unique for two main reasons. The first is that a passive sensing approach for an environmental sensor based on FePc is fundamentally different from what has been done with other MPc sensors. Passive sensing was made possible due to the high adsorption characteristics of the engineered FePc thin film and the formulation of a passive response calibration model. The second is that nitrogen dioxide sensing with MPc thin films has not been previously reported at sub-zero temperatures. Other research into MPc thin film sensors for the detection of nitrogen dioxide have at lowest been demonstrated at room temperatures. The FePc thin film sensor in this research was able to operate at temperatures as low as -46 °C. It is worth noting that at these conditions, the FePc thin film was more sensitive towards the detection of nitrogen dioxide gas. For the above reasons, the approach of using a cost-effective, passively monitored FePc thin film nitrogen dioxide sensor is different from previous work involving active sensor systems and shows promise for use as an actual field sensor. Table 7.1 provides a summary of all the parameters regarding the passive FePc thin film sensor presented in this research.

Table 7.1: Summary of sensor parameters

Parameter	Value
Film thickness	450 nm
Intrinsic resistance*	>2.0 x 10^7 Ω
Intrinsic conductivity*	<1.1 x 10^{-5} $\Omega^{-1}m^{-1}$
Extrinsic resistance**	<3.5 x 10^3 Ω
Extrinsic conductivity**	>6.5 x 10^{-2} $\Omega^{-1}m^{-1}$
Adsorption rate constant/Sensitivity (k_a)	16.15
Desorption rate constant (k_d)	1.003 x 10^{-5}
Power law constant (S)	4.8
Lower limit of detection	0.3 ppm
Response time	<1 min
Temperature range	-46 to 71 °C
Intrinsic activation energy	0.76 eV
Extrinsic activation energy	0.30 eV

* Under N_2 at 20°C

** Under NO_2 saturation at 20°C